Faculdade de Engenharia da Universidade do Porto

Experimental Development and Validation of a Fully Variable Valve Actuation System for a Superheated Steam Expansion Machine

Catarina Rodrigues Rosa Costa Brites

Master Thesis



Master in Mechanical Engineering
Fluids & Energy

Supervisor at FEUP: Prof. Dr. Abel Rouboa

Supervisor at KIT: Dr.-Ing. Malki Maliha

September 11, 2026

Experimental Development and Validation of a Fully Variable Valve Actuation System for a Superheated Steam Expansion Machine

Catarina Rodrigues Rosa Costa Brites

Master in Mechanical Engineering
Fluids & Energy

September 11, 2026

Abstract

The performance of steam expansion machines operating at variable expansion ratios depends critically on the accurate control of the intake valve system, which regulates the mass flow rate and timing of steam admission.

This thesis experimentally investigates a fully variable spool valve control concept, based on a linear actuator. A dedicated test bench was developed for this purpose, introducing modifications to the previous design to improve manufacturability, assembly and sealing, which represents a further contribution of this thesis, supporting the experimental characterization of future actuation systems.

Using this test bench, the operating limits of the actuator were characterized, taking into account the effects of friction and moving mass across different stroke amplitudes and operating frequencies, with particular attention to the precision and repeatability of the valve opening timings.

The operating range was found to be limited primarily by the actuator's I^2t thermal protection algorithm. Under these conditions, the maximum sustainable speed was 475 rpm for the least demanding configuration, decreasing to 375 rpm for the highest tested amplitude and mass. Stroke amplitude was found to be the most influential parameter on actuator loading, more so than moving mass. Position tracking errors of more than 10% of the commanded stroke amplitude were observed under the most demanding operating conditions, and the cycle-to-cycle variability of the valve opening duration, quantified by the coefficient of variation (COV), remained generally below 11%, increasing as the actuator approached its operating limits.

While the proposed actuation concept was experimentally validated, the actuator's performance remained substantially below the target speed and stroke amplitude defined for the final expansion machine (1500 rpm and 40 mm), indicating that it does not meet the requirements of the intended application.

These findings contribute to guiding the selection and design of actuation systems for future prototypes of the expansion machine.

Keywords: Waste Heat Recovery, Clausius Rankine Cycle, Variable Valve Actuation, Spool Valve, Linear Actuator, Thermal Overload.

Resumo

O desempenho de máquinas de expansão a vapor que operam com razão de expansão variável depende de forma crítica do controlo preciso do sistema de válvulas de admissão, responsável por regular o caudal mássico e a temporização da admissão de vapor.

Esta tese investiga experimentalmente um conceito de atuação totalmente variável para uma válvula-pistão (*spool valve*), baseado num atuador linear. Para este efeito, foi desenvolvido um banco de ensaio dedicado, que introduz modificações ao design anterior de modo a melhorar a manufatura, a montagem e a vedação — uma contribuição adicional desta tese, que fica disponível para apoiar a caracterização experimental de futuros sistemas de atuação.

Com recurso a este banco de ensaio, caracterizaram-se os limites operacionais do atuador, considerando os efeitos da fricção e da massa em movimento, para diferentes amplitudes de curso e frequências de operação, com particular atenção à precisão e à repetibilidade dos tempos de abertura da válvula.

Verificou-se que a gama de operação é limitada sobretudo pelo algoritmo de proteção térmica I^2t do atuador. Nestas condições, a velocidade máxima sustentável foi de 475 rpm na condição menos exigente, descendo para 375 rpm na condição de maior amplitude e massa testadas. A amplitude de curso revelou-se mais determinante para a carga do atuador do que a massa em movimento. Nas condições operacionais mais exigentes, registaram-se erros de seguimento de posição superiores a 10% da amplitude de curso comandada, enquanto a variabilidade ciclo-a-ciclo da duração de abertura da válvula — quantificada pelo coeficiente de variação (COV) — se manteve, de um modo geral, abaixo de 11%, aumentando à medida que o atuador se aproximava dos seus limites operacionais.

Embora o conceito de atuação proposto tenha sido validado experimentalmente, o desempenho do atuador ficou substancialmente aquém dos valores-alvo de velocidade e amplitude de curso definidos para a máquina de expansão final (1500 rpm e 40 mm), o que indica que o atuador não cumpre os requisitos da aplicação pretendida.

Estes resultados contribuem para orientar a seleção e o desenho de sistemas de atuação para futuros protótipos da máquina de expansão.

Palavras-Chave: Recuperação de Calor Residual, Ciclo de Clausius-Rankine, Válvula-Pistão (*Spool Valve*), Atuação Variável de Válvulas, Atuador Linear, Sobrecarga Térmica.

Acknowledgements

First of all, I would like to thank my supervisor, Malki Maliha, for his support and guidance throughout this work. I am also very grateful to Prof. Abel Rouboa for his advice and for sharing his knowledge and experience in scientific research.

At the workshops of the Institut für Kolbenmaschinen (IFKM), I could always count on the help and support of Ruben Klumpp, Axel Tolksdorf-Vollmer, and Philipp von Wintzingerode, whose dedication and expertise were invaluable during the manufacturing process and the development of the experimental setup.

I would also like to thank my colleagues from the HeDaMa project for their support and for making me feel welcome and integrated into the team. A special thank you goes to Jonas and Alexandre for their help and friendship throughout this journey.

I am also very grateful to the people who made my time in Karlsruhe so wonderful. A special thank you goes to my friends Caty, Elias, Maxime, and Federica, for their friendship and support.

I would also like to thank my dear friends Leonor Nicolau, Eva Pires, Leonor Louro, and Ana Rodrigues, my companions in life, whom I can always rely on.

Finally, my greatest thanks goes to my family. To my grandmothers that I know would be very happy for me, and especially to my parents and my brother, for their unconditional support, encouragement, and love throughout every step of my journey. I am deeply grateful for always having them by my side.

Contribution to the Sustainable Development Goals (SDGs)

The Sustainable Development Goals (SDGs) are a set of 17 global objectives adopted by the United Nations in 2015 as part of the 2030 Agenda for Sustainable Development, aimed at guiding collective action towards a more sustainable, equitable and resilient future. Engineering research, given its direct role in shaping the technologies that underpin energy, industry and transport systems, is particularly well positioned to contribute to these goals.

This thesis relates most directly to SDG 7 (Affordable and Clean Energy), SDG 9 (Industry, Innovation and Infrastructure) and SDG 13 (Climate Action), through its contribution to Waste Heat Recovery (WHR) technology for marine applications. International shipping remains a significant, largely fossil-fuel-dependent source of GHG emissions, and the 2023 IMO Strategy on the Reduction of GHG Emissions from Ships sets indicative checkpoints of 20–30% emission reduction by 2030 and 70–80% by 2040 relative to 2008, with net-zero targeted by or around 2050 International Maritime Organization (2023). Rankine-cycle-based WHR systems installed onboard cargo vessels, such as the expansion machine this thesis's actuation system is designed for, support this transition by converting otherwise wasted exhaust and cooling heat into usable electrical power, directly reducing fuel consumption and associated emissions.

The valve actuation system investigated here is not the WHR system itself, but an enabling component: without accurate and repeatable metering of steam admission across the variable heat availability typical of a ship's operating profile, the expansion machine cannot deliver its intended efficiency gains. The experimental results of this thesis are therefore relevant beyond their immediate scope — the actuator's achieved positioning accuracy, repeatability (COV), and operating envelope relative to the target application (1500 rpm, 40 mm stroke) can be read as indicators of how close this actuation concept is to enabling a deployable, full-scale marine WHR system, and thus to translating into measurable fuel and emissions savings at the SDG 7/13 level.

Contents

1 Introduction **1**
- 1.1 Motivation . . . 1
- 1.2 Objectives . . . 2
- 1.3 Structure of the Thesis . . . 2

2 State of the Art **5**
- 2.1 Thermodynamical Fundamentals . . . 5
- 2.2 Presentation of the Super-Heated Steam Engine . . . 6
  - 2.2.1 Working Principle . . . 6
  - 2.2.2 Spool Valve . . . 8
- 2.3 Variable Valve Control . . . 9
- 2.4 Actuation Systems . . . 11
  - 2.4.1 NLi120X Actuator . . . 12
  - 2.4.2 Linear Motor Working Principle . . . 13
  - 2.4.3 Cascade Control . . . 14
  - 2.4.4 Thermal Management and Protection Mechanisms . . . 15
  - 2.4.5 Kinematics of the movement . . . 17
- 2.5 Cycle-by-Cycle Variation Analysis . . . 19

3 Methodology **21**
- 3.1 Design Development . . . 21
- 3.2 Experimental Setup . . . 22
  - 3.2.1 Structure of Test Bench . . . 22
- 3.3 Design of Experiments . . . 23
  - 3.3.1 Thermal Management . . . 24
  - 3.3.2 Control Tuning . . . 25
- 3.4 Instrumentation . . . 27
  - 3.4.1 Position Reference and Calibration . . . 27
- 3.5 Uncertainty Analysis . . . 28

4 Results and Discussion **29**
- 4.1 Operation Limits . . . 29
- 4.2 Velocity and Position Synchronization . . . 35
- 4.3 Friction Analysis . . . 42
- 4.4 Thermal Analysis . . . 43

5 Conclusions **47**
5.1 Future Works . . . 49
5.1.1 Actuator Selection and Requirements for the Final Machine . . . 50
5.1.2 Thermal Management and Validation . . . 50
5.1.3 Control, Communication and Synchronization . . . 50
5.1.4 Long-Duration and Repeatability Validation . . . 51
5.1.5 Mechanical Configuration Optimization . . . 51

References **53**

A Attachments - State of the Art **59**
A.1 Thermodynamical Fundamentals . . . 59
A.2 NLi120X Datasheet . . . 59

B Attachments - Methodology **63**
B.1 Technical Drawings . . . 63
B.2 Experimental Setup . . . 84
B.3 Control Parameters . . . 84
B.4 NiLab Meeting . . . 85

C Attachments - Results and Discussion **87**
C.1 Operation Limits . . . 87

List of Figures

2.1 Super-Heated Steam Expansion Machine [Modeled with PTC Creo Parametric7] . . . 7
2.2 Valve Timing for Spool Valve Control System of the Superheated Steam Engine. . . . 7

3.1 Test Bench Setup. . . . 22
3.2 Detailed View of Test Bench Components. . . . 22
3.3 Control Scheme. . . . 26

4.1 Motor load of the actuator for different speeds and mass configurations. . . . 30
4.2 Mechanical power and motor force for different strokes and amplitudes. (Configuration E). . . . 33
4.3 Motor force as a function of position feedback for configuration E. . . . 34
4.4 Motor force as a function of actuator position for the unloaded actuator (no valve or additional mass attached), at a 30 mm stroke and 375 rpm. . . . 34
4.5 Current Target, Feedback and SVM amplitude for configuration E, at 375 rpm. . . . 35
4.6 Comparison between the theoretical sinusoidal reference and the measured intake valve velocity (top) and position (bottom) for configuration E with a 20 mm stroke. . . . 36
4.7 Comparison between the theoretical sinusoidal reference and the measured intake valve velocity (top) and position (bottom) for configuration E with a 30 mm stroke. . . . 37
4.8 Difference between feedback position and sinusoidal function for different speeds. . . . 38
4.9 Mean Effective Position Error as a function of Operating Conditions. . . . 42
4.10 Evolution of the motor/drive temperature and I^2T current over time during the diagnostic test. . . . 44

A.1 Ideal TS-Diagram of water for an ideal Clausius-Rankine Cycle at 600 °C and 30 bar Grigull et al. (1984). . . . 59

B.1 Programming box combined with NLi120X motor (cable connections) . . . 84

List of Tables

3.1 Experimental test configuration and respective moving masses. 23
3.2 Cascade Control System Equations (Laplace Domain). 26

4.1 Position errors at IOT (1&3) and ICT (2&4), and their differences between the 1st and 4th cycles. 39
4.2 Statistical analysis of the measured inlet opening duration (1–2) and (3–4). 40

B.1 Feedback control parameters. 84
B.2 Feed forward control parameters. 84
B.3 Description of Meeting with NiLAB. 85

C.1 Operating limits identified for each configuration and stroke amplitude based on the last recorded point before I^2T thermal overload. 87

List of Acronyms

BDC	Bottom Dead Center
CBC	Cycle-by-Cycle
CCL	Current Control Loop
COV	Coefficient of Variation
CRC	Clausius Rankine Cycle
EtherCAT	Ethernet for Control Automation Technology
FOC	Field-Oriented Control
FVC	Fully Variable Control
ICE	Internal Combustion Engine
ICT	Inlet Closing Time
IOD	Intake Opening Duration
IOT	Inlet Opening Timing
GHG	Greenhouse Gas
ORC	Organic Rankine Cycle
PCL	Position Control Loop
PLC	Programmable Logic Controller
PMLSM	Permanent Magnet Linear Synchronous Motor
SDGs	Sustainable Development Goals
TDC	Top Dead Center
VCL	Velocity Control Loop
VVA	Variable Valve Actuation
VVL	Variable Valve Lift
VVT	Variable Valve Timing
WHR	Waste Heat Recovery

List of variables

A	Amplitude
e_{bemf}	Back Electromotive Force
f	Frequency
I_{Cont}	Continuous Rated Current
I_f	Feedback Current
I_{RMS}	Root Mean Square Current
m_{mov}	Moving Mass
t	Time
u_{ff}	Feed-Forward Control Input
$\dot{x}$	Actuator's Velocity
$\ddot{x}$	Actuator's Acceleration
μ_X	Mean of Parameter X
x_f	Feedback Position
σ_X	Standard Deviation of Parameter X

Chapter 1

Introduction

1.1 Motivation

Waste Heat Recovery represents a promising opportunity to reduce greenhouse gas (GHG) emissions from industrial and marine applications, among others. Taking Europe as an example, the potential of waste heat recovery in industry has been estimated to range between 300 and 375 TWh/year. When put into perspective with a total heat requirement in Europe estimated at 1820 TWh/year, this demonstrates the relative importance that waste heat recovery in industry could bring to the energy sector and its contribution to achieving more sustainable energy systems Jovet et al. (2022).

For power generation from waste heat, a variety of technologies have been developed and established to accommodate different heat-source temperatures and power ranges Raab et al. (2024). Among these technologies, systems based on the Rankine Cycle have demonstrated high efficiency and are widely employed in waste heat recovery applications. Within such systems, the expansion machine plays a particularly critical role, as it is the component responsible for converting the thermal energy of the working fluid into useful mechanical power and, ultimately, electrical energy Latz et al. (2013).

The performance of the expansion machine is strongly influenced by the conditions at its intake, where the working fluid enters the expansion process. This is typically regulated by control valves that adjust the mass flow rate and timing of steam admission, directly affecting the thermodynamic conditions of the expansion process and, consequently, the overall efficiency and power output of the system.

Camless valve actuation is well established in internal combustion engines, where variable timing and lift are used to optimize combustion Srivastava et al. (2018), Paden et al. (2015). Its application to steam admission in waste heat recovery systems, however, remains largely unexplored, with existing expansion machines typically relying on fixed or discretely adjustable valves rather than fully variable actuation. This is especially relevant given the intrinsic variability of recovered waste heat, which fluctuates with the source

process, load, and operating regime, requiring an intake system capable of adapting continuously Wieland et al. (2023). Yet the dynamic performance, positioning accuracy, and repeatability of linear actuator-driven valves under such variable conditions remain uncharacterized in the literature — a gap that constitutes the starting point for the present work.

This thesis therefore aims at experimentally investigating the intake cylinder of an expansion machine capable of generating electricity at a variable expansion ratio, with a focus on the possibilities and limitations of valve actuation control.

1.2 Objectives

The primary objective of this thesis is to experimentally validate a fully variable spool valve actuation concept, assessing its feasibility for application in the intake system of a super-heated steam expansion machine. To achieve this, an experimental test bench is developed based on previous works, introducing the necessary modifications to improve manufacturability, assembly and sealing while preserving the original operating principle.

The experimental work focuses on evaluating whether the selected NLi120X linear actuator is capable of meeting the dynamic and accuracy requirements imposed by the proposed valve actuation system. Particular attention is given to determining the range of operating frequencies, stroke amplitudes and moving masses that can be achieved while maintaining accurate and repeatable valve positioning with minimum tracking error. Furthermore, the influence of these operating parameters on the actuator performance is analyzed in order to identify the practical operating limits of the system.

In addition, the study aims to evaluate the repeatability and reliability of the actuation system during continuous operation through the statistical analysis of successive operating cycles. This assessment makes it possible to determine whether the actuator is capable of maintaining stable performance over extended operating periods without significant degradation in positioning accuracy or dynamic response. Ultimately, the results obtained provide an experimental validation of the proposed actuation concept, establish its operating envelope and identify the conditions under which the system can be reliably implemented in future prototypes of the steam expansion machine.

1.3 Structure of the Thesis

The work is organized into five chapters, covering the current state of the art, theoretical background, system development, experimental methodology, results, and conclusions.

Chapter 2 presents the state of the art relevant to the topic, ranging from variable valve control to linear motor operation. It establishes the theoretical basis for the experimental investigation and provides the context for the superheated expansion machine conceptualized in previous works.

Chapter 3 describes the experimental setup and procedure carried out in this work, including the materials used and the variables investigated. Furthermore, the data collected is presented and analyzed in Chapter 4. The motor's behaviour and operating conditions are discussed in detail in this chapter.

Finally, Chapter 5 assesses the overall outcomes of the experimental investigation. An outlook for future research is also provided, taking into account the limitations identified during the investigation and the future development of the expansion machine.

Chapter 2

State of the Art

2.1 Thermodynamical Fundamentals

Waste heat recovery enables otherwise wasted thermal energy to be converted into useful power, contributing to improved energy efficiency and reduced environmental impact Maurya et al. (2025). Rankine-cycle-based WHR systems have been widely investigated and have demonstrated significant potential for improving energy efficiency and reducing pollutant emissions Maurya et al. (2025). For example, Liu et al. Liu et al. (2020) proposed a combined Steam Rankine Cycle (SRC) and Organic Rankine Cycle (ORC) for marine applications, achieving a 4.42% increase in engine thermal efficiency and a reduction in fuel consumption of 9322 tons per year at full engine load. Compared with other WHR technologies, such as thermoelectric generators and absorption air-conditioning systems, Rankine-cycle-based systems have also shown high potential for recovering waste heat from internal combustion engines Quoilin et al. (2013). The selection of the most suitable thermodynamic cycle for the present application, driven primarily by the operating temperature range of the available heat source, has been studied in detail in previous works, particularly in Siedler (2024) and Eirich (2024).

The Clausius-Rankine Cycle (CRC) uses steam as the working fluid and consists of four main processes: pumping, heating, expansion, and condensation. The working fluid is pressurized and heated using an external waste heat source, expanded in an expansion machine to produce mechanical work, and subsequently condensed before being pumped back to the boiler, completing the cycle. The corresponding ideal cycle is illustrated in the T–s diagram shown in Appendix A.1.

The ORC follows the same basic principle but uses an organic working fluid, such as n-pentane or toluene, instead of water. Different working fluids can be selected according to the temperature of the available heat source, with isentropic fluids being particularly suitable for low-temperature heat recovery Shu et al. (2013). However, ORC systems are often exposed to significant fluctuations in the temperature and mass flow rate of the waste heat source, imposing demanding requirements on dynamic modeling and control

Wieland et al. (2023).

2.2 Presentation of the Super-Heated Steam Engine

2.2.1 Working Principle

Within the CRC, the expansion machine is a key component, as it transforms the thermal energy carried by the working fluid into mechanical work, which can subsequently be converted into electrical power Latz et al. (2013).

Similarly to any steam expansion machine, two sections must be distinguished: the hot and cold section. In the studied engine, the hot section includes the steam lines, the control system, and two spool valves per intake cylinder, also known as piston valves, responsible for controlling the intake of the steam in the working piston. The cold section includes the cross head and crank mechanism.

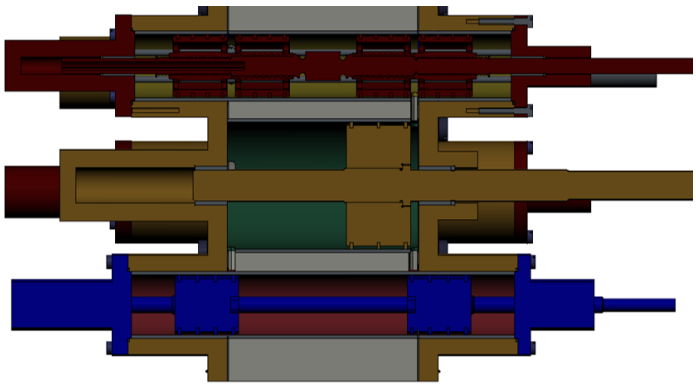
The structure includes, in the inlet side, four cylinders, with two spool valves each. The working stage is composed by two main cylinders, each with one double acting piston. At last, the outlet side has two cylinders, with two pistons each.

Its design incorporates several key features aimed at improving the overall efficiency of the system. When common intake and exhaust channels are employed, the hotter incoming steam transfers heat to the housing, which is subsequently absorbed by the cooler outgoing steam and carried outwards, resulting in a net reduction in efficiency. To mitigate this effect, the intake and outlet channels in the studied machine are physically separated and positioned on opposite sides of the machine.

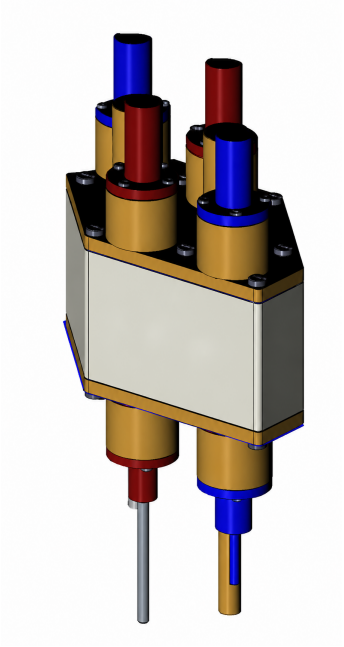
The position of the working piston is described by the crank angle, with the Top Dead Center (TDC) and Bottom Dead Center (BDC) defining the reference positions. These positions are used to define the timing of the intake and exhaust events. Steam admission begins when the superheated steam, previously stored in the intake control cylinder, enters the working cylinder through the intake port. This event is defined as the inlet opening timing (IOT) and is specified as a crank-angle position referenced to the working piston.

Although the intake valves are actuated independently of the crank mechanism, their opening and closing events are synchronized with the motion of the working piston and occur once per engine cycle, corresponding to half the frequency of the working piston reciprocation. The intake port remains open for the intake opening duration (IOD), after which, at the inlet closing timing (ICT), it is sealed by the spool valves, isolating the control cylinder from the working cylinder. The trapped steam then expands approximately isentropically, driving the working piston and producing mechanical work.

Consequently, the valve events, IOT and ICT, are defined as crank-angle positions referenced to the motion of the working piston, while the IOD corresponds to the crank-angle interval during which the intake port remains open. The IOD has been shown to be one of the main parameters governing the engine output torque Heyder (2025).



(a) Cross Section View.



(b) Complete system. In red the hot section of the machine, in blue the cold one.

Figure 2.1: Super-Heated Steam Expansion Machine [Modeled with PTC Creo Parametric7]

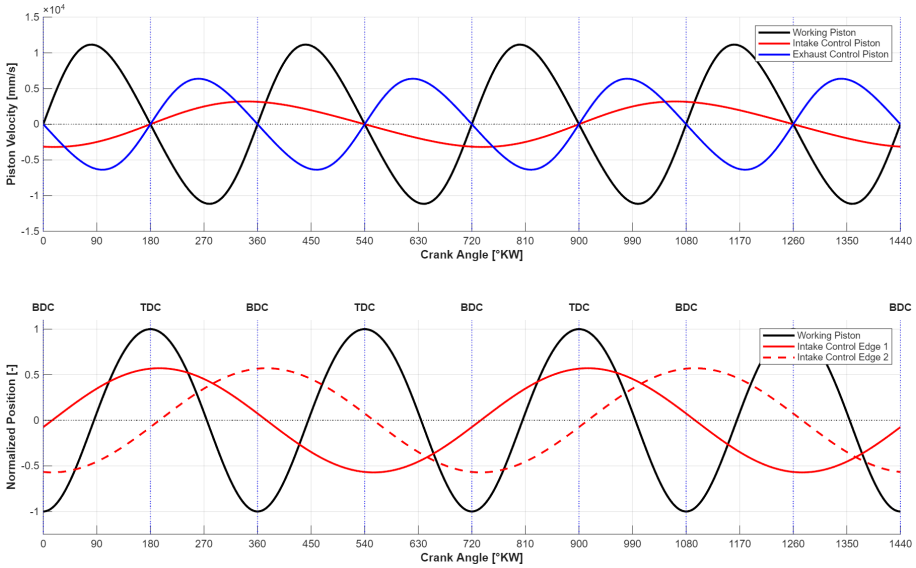


Figure 2.2: Valve Timing for Spool Valve Control System of the Superheated Steam Engine.

Figure 2.2 illustrates the opening and closing timings of the intake valves. The valve motion is defined by the equations presented in Siedler (2024) and Heyder (2025), with the motion of the intake control spool valve being determined independently of the crank

mechanism.

The frequency of the intake control piston determines the frequency of the intake valve events and is therefore related to the frequency of the working piston reciprocation, with the latter being twice the former. This synchronization ensures that the intake events occur once per working cycle and that the desired mechanical work can be produced. The exhaust control piston, on the other hand, operates at the same frequency as the working piston. After expansion, the steam exits the working cylinder through the exhaust port, with the exhaust process being similarly defined by the exhaust opening and closing timings and the corresponding exhaust opening duration.

2.2.2 Spool Valve

The design of inlet and outlet valves in combination with appropriate control, is a central element of the super-heated steam engine. The size of the valves affects the mass flow rate in the system and thus the efficiency and power of the machine.

A distinctive feature of the proposed design is the incorporation of spool valves, a cylindrical variant of the valve. The wall of the cylindrical valve sleeve is interrupted by slit-shaped steam channels. The valve consists of two piston bodies mounted on a common valve rod. Unlike flat slide valves, where steam pressure acts only on one side of the surface, the piston spool valve is affected by steam pressure on both external surfaces Siedler (2024). The presence of two control edges per valve enables precise control of the fluid flow.

In conventional valve systems, the intake process occurs when the valve velocity is zero, as the valve changes its direction of motion. However, in this design, the intake takes place when the piston reaches its maximum velocity. By opening and closing the valves at this operating point, the throttling effect is expected to be significantly reduced, thereby minimizing flow losses and improving efficiency, particularly during short admission periods Cornetti (2025).

The transverse force introduced by this configuration can be absorbed by linear bearings, while sealing is achieved using piston sealing rings rather than relying on direct contact between the spool and the cylinder. This approach allows a small running clearance to be maintained between the moving components while limiting leakage through the clearance. The sealing of the spool valve is provided by piston rings, whose role in reciprocating machinery extends well beyond preventing gas leakage Yamagata (2005). In addition to sealing the working chamber against the escape of pressurized gas, piston rings regulate and distribute the lubricant film along the cylinder wall and stabilize the lateral and tilting motion of the piston Sherrington (2010), MS Motorservice International GmbH (2015).

This sealing function, however, comes at a mechanical cost. Piston rings are historically one of the main contributors to friction losses in reciprocating machines: the friction generated between the piston/ring assembly and the cylinder liner typically accounts for

approximately 15–20% of the total mechanical friction losses. The design of the ring–liner interface therefore represents a compromise between effective sealing and acceptable friction, rather than an optimization of either aspect in isolation Mahle GmbH (2012), Nagar and Miers (2011).

The lubrication regime experienced by the ring–liner contact, and consequently its associated friction and wear, varies considerably along the piston stroke. In conventional reciprocating machines, the piston reaches zero instantaneous velocity at the top and bottom dead centres (TDC and BDC). At these reversal points, the piston is momentarily not moving, so no lubricant film can form between the ring and the liner. This results in direct contact between the two surfaces, increasing friction and wear Mahle GmbH (2012). Conversely, around mid-stroke, where the sliding velocity is maximum, a thick and continuous lubricant film is established, and friction becomes governed primarily by the viscous shear of the lubricant rather than by direct surface contact Nagar and Miers (2011).

In the present design, however, this behaviour cannot be directly transposed, since the spool valve does not reverse direction at the positions relevant to the intake process. As previously discussed, the valve opening and closing events occur close to the point of maximum piston velocity rather than at a velocity reversal. Consequently, the ring–liner contact at the intake and exhaust timings is expected to benefit from more favorable lubrication conditions than would be the case in a conventional dead-centre-actuated valve.

Operating without piston rings would eliminate the associated contact friction, but it would allow pressurized gas to leak past the piston into the adjacent chamber during operation. This uncontrolled leakage leads to an immediate loss of thermodynamic efficiency and a reduction in the useful power output of the machine.

2.3 Variable Valve Control

The methods to control the lift and timing of the intake and exhaust valves of an ICE are collectively known as variable valve timing (VVT), variable valve lift (VVL) or variable valve actuation (VVA) systems. Modifications to the camshaft to have variable valve lift and timing control have been carried out by many automotive manufacturers, and such technologies are being used in many vehicles of everyday use Haskara et al. (2004).

Camless valve actuation originates from the pioneering electrohydraulic system of Schechter and Levin (1996), which established full independence between valve motion and crankshaft phasing as the defining principle of camless actuation, later refined into a range of electrohydraulic and electromagnetic architectures.

A variable valve actuation system allows to flexibly control the timing and lift of the engine valves according to the speed and load on the engine. VVA systems today not only target at reducing pumping losses but also at improving the overall efficiency of the engine

by functioning as a better engine management system as compared to fixed valve lift and timing systems Srivastava et al. (2018).

Jiang et al. (2020) developed a fully variable actuation system that demonstrated significant utility in providing real-time, continuous adjustment of valve timing, duration and lift. By meeting critical design requirements, the fully flexible mechanism was able to optimize engine performance across all operating points more effectively than traditional fixed camshafts.

Speed control causes the operating point of maximum steam-engine efficiency to shift toward different mass flow rates: a lower speed enables more effective use of lower mass flow rates, while an increased speed leads to better efficiency at higher mass flow rates. Valve control, in turn, allows the operating point of the steam engine to be adjusted within its characteristic map, making it possible to adapt the mass flow rate and optimize efficiency accordingly. For this reason, the time interval between the fully closed and fully open positions should be kept as short as possible, since the control edge acts as a flow resistance (throttle) during this transition Heyder (2025).

The camless valvetrain is considered to be a promising solution to improve the engine performance. Most of the camless valvetrains, based on reluctance force, suffer the problem of high impacts at valve seating, which restricts its mass production. The difficulty for the engine valves actuators in the case of full camless engine is to cover the large range of forces and dynamics, required for operating correctly all intake and all exhaust valves Dimitrova et al. (2019).

Although variable valve actuation has been extensively investigated for internal combustion engines, the same concept can also be exploited in expansion machines operating on Rankine-type cycles. Unlike IC engines, where valve actuation is mainly employed to improve combustion efficiency and reduce pumping losses, in steam engines valve timing directly determines the admitted steam mass, the expansion ratio, and consequently the engine efficiency over a wide operating range.

This sensitivity has been confirmed experimentally across different expansion machine architectures. Badami and Mura (2009) designed and tested a small-scale reciprocating steam engine for a wood-waste Rankine cycle Combined Heat and Power unit, comparing part-load control strategies and showing that adjusting the admission cut-off, rather than expander speed alone, is essential to preserve efficiency away from the design point. For volumetric spool expansion devices, Antonelli et al. (2014) combined numerical (AMESim) and experimental analysis to quantify how valve advance and admission/recompression degree affect part-load performance of a small spool expander intended for solar-, geothermal-, biomass- and waste-heat-driven power plants. More recently, Wronski et al. (2019) implemented a spool variable-timing admission valve on a reciprocating piston expander for a small-scale organic Rankine cycle, enabling the expansion ratio to be adjusted in real time and achieving an isentropic efficiency of approximately 70%. Taken together with the sensitivity of expander performance to inlet valve timing already re-

ported by Latz et al. (2013) for a steam Rankine cycle waste-heat recovery system, these studies consistently identify valve timing as one of the dominant parameters governing the efficiency and flexibility of Rankine-cycle expansion machines, regardless of the specific expander architecture (reciprocating, rotary, or spool-type).

However, in each of these studies valve timing is varied through a manually adjustable or motor-driven mechanical linkage, and is evaluated primarily at the level of thermodynamic and part-load performance rather than through a fully variable, closed-loop actuation system whose own dynamic response, positioning accuracy, and repeatability are characterized. In the previous work by Eirich (2024), operating strategies for a solar-driven steam engine were investigated, showing that engine speed should be used as the primary control variable while valve timing provides fine adjustment of the operating point. This identifies variable valve timing as a key enabling technology for efficient and flexible steam engine operation under varying steam supply conditions, while also highlighting that the actuation system itself — rather than only the resulting valve event — must be experimentally validated before it can be reliably implemented in practice.

Fully Variable Control (FVC) enables the independent adjustment of valve opening timing and opening duration, allowing the steam engine to be adapted to varying operating conditions. Unlike fixed valve mechanisms, FVC provides sufficient flexibility to regulate both the admitted steam mass flow and the expansion process, making it particularly suitable for applications with highly variable thermal input.

A sensitivity analysis conducted by Heyder (2025) demonstrated that the engine speed and the inlet valve actuation parameters are the dominant variables governing the operating point of the steam engine. Increasing the engine speed reduces the valve opening duration available per cycle, resulting in less steam admitted per stroke. However, the higher number of cycles per second increases the overall live-steam mass flow through the engine. As the inlet valve opening duration increases, more steam is admitted into the cylinder, resulting in a higher mean indicated pressure and, consequently, greater engine torque. Nevertheless, this benefit reaches a saturation point beyond which further increases in opening duration produce little additional torque while reducing efficiency due to the shortened expansion phase. Furthermore, the inlet valve opening timing strongly influences the engine performance. Opening the inlet valve significantly before top dead center leads to a rapid reduction in torque, highlighting the importance of accurate valve timing for efficient operation.

2.4 Actuation Systems

The timing and duration of steam admission have a significant impact on the performance and efficiency of steam engines. Variations in valve timing parameters can considerably affect key operating characteristics, highlighting the importance of accurate and responsive intake control systems.

To achieve the required level of control, modern steam engine architectures increasingly rely on electronically actuated valve systems capable of adjusting valve position according to the engine operating conditions. Such systems enable greater flexibility compared to conventional mechanical valve trains and allow the implementation of advanced control strategies aimed at improving efficiency, responsiveness, and overall engine performance Cornetti (2025).

Electro hydraulic and electromagnetic systems enable very flexible control of valve timing phase and duration, as well as near-optimal valve event timing at all operating speeds and loads. However, challenges remain in the design and control of electro hydraulic and electromagnetic valve systems with regard to response times, power consumption, and control Paden et al. (2015).

Different actuation technologies were carefully evaluated in previous design studies conducted by Cornetti (2025), including hydraulic and pneumatic actuators, electric spindle drives, and electric linear motors. Based on this assessment, the NLi120X tubular linear actuator was selected as the most suitable solution for the present valve actuation system, due to its dynamic performance, compact design, and integration capabilities.

2.4.1 NLi120X Actuator

The increasing demand for compact, efficient, and highly integrated automation systems has driven the development of smart electric actuators. This actuator combines mechanical transmission, power electronics, sensing and communication ability within a single unit.

The NLi120X is a tubular permanent-magnet linear motor that converts electrical energy directly into linear motion. It supports digital inputs and outputs for motion controlling, homing operations, status monitoring and fault reporting, characteristics that make it suitable for automation environments.

All the information regarding mechanical performance, electrical, thermal, mechanical and encoder specifications, can be consulted in the actuator's datasheet (Appendix A.2) and the motor's technical database NiLAB GmbH (2023). This document also contains a Force vs Velocity Graph.

The actuator is operated in closed-loop control using the integrated linear encoder, which continuously measures the slider position and provides feedback to the servo controller.

All operational parameters, including control word settings, status monitoring, and the scaling/offset of analog inputs, are managed via the NiLAB Starter Commissioning Tool.

2.4.2 Linear Motor Working Principle

Permanent Magnet Linear Synchronous Motors (PMLSMs) are the linear counterpart of Permanent Magnet Synchronous Motors and are capable of producing linear motion directly. In contrast to conventional electromechanical drives, linear motors do not require mechanical transmission elements such as gearboxes, ball screws, or other reduction mechanisms Wendel et al. (2017).

The direct-drive configuration eliminates transmission-related effects such as backlash and pitch errors, which is particularly advantageous in applications requiring high positioning accuracy and dynamic response Yuan et al. (2021). In the present application, this characteristic is particularly relevant since the actuator is required to impose a prescribed linear motion directly on the valve mechanism. Furthermore, the fully variable nature of the valve actuation system allows the displacement trajectory to be defined according to the desired valve timing, rather than being constrained by a fixed mechanical cam profile.

The electromagnetic force generated by a PMLSM is directly related to the motor current. Consequently, the thrust required to achieve a prescribed motion, particularly under high acceleration or increased mechanical load, results in a corresponding increase in the required motor current. This relationship is particularly relevant to the present study, as the current demand ultimately influences both the dynamic performance and the thermal behaviour of the actuator Wang et al. (2018), Buyukdegirmenci and Krein (2013).

The electrical actuation of high-performance permanent magnet synchronous motors is commonly based on Field-Oriented Control (FOC). In FOC, the three-phase motor currents are transformed into a rotating d-q reference frame, where the current components can be controlled independently. In this representation, the q-axis current is primarily associated with electromagnetic force production, while the d-axis current is related to the flux-producing component. The current controller therefore determines the voltage references required to achieve the commanded motor current.

The electrical behaviour of the motor can, in simplified form, be described by the voltage balance

$$v = Ri + L\frac{di}{dt} + e_{\mathrm{bemf}}, \tag{2.1}$$

where R represents the winding resistance, L the winding inductance, and e_{bemf} the back electromotive force. The winding resistance determines the resistive voltage drop and associated electrical losses, while the inductance limits rapid variations in current. The back-EMF is generated by the motion of the motor and opposes the applied voltage. These electrical effects determine the voltage required to establish the desired current during operation.

The voltage references generated by the FOC are subsequently applied to the inverter using Space Vector Modulation (SVM). SVM represents the three-phase voltage system as

a single rotating space vector and synthesizes the desired voltage vector by appropriately combining the available inverter voltage vectors within each pulse width modulation period. The reference vector is generated using the adjacent active voltage vectors together with the zero vectors, with their respective application times determining the resulting voltage magnitude and direction. This allows the inverter to generate the required voltage within the limits imposed by the available DC-bus voltage Bose (2002).

The resulting control structure establishes the connection between the prescribed mechanical motion and the electromagnetic actuation of the NLi120X. The current required by the motor is therefore ultimately determined by the force associated with the commanded motion, while the FOC and SVM provide the electrical control required to achieve this current. The integration of these elements into the position, velocity, and current control loops is discussed in the following section.

2.4.3 Cascade Control

Cascade control architectures are widely adopted in valve actuation systems because they allow the fast inner dynamics of the actuator to be decoupled from the slower motion dynamics of the valve, improving stability and tracking performance. In particular, accurate position tracking is required in applications in which the mover has to follow a predefined trajectory Mercorelli and Werner (2017)..

Different control strategies have therefore been investigated for PMLSM-based positioning systems. Wendel et al. (2017) investigated model predictive position control for a permanent magnet synchronous linear motor and compared its performance with conventional control approaches, demonstrating the relevance of the position-control layer for achieving high dynamic performance and accurate trajectory tracking.

More recently, adaptive model predictive current control was investigated for PMLSM drives and showed that variations in parameters such as permanent-magnet flux, inductance and resistance can affect current regulation and, consequently, the overall drive performance Wang et al. (2018), Kennel et al. (2023).

These studies illustrate the different control levels involved in high-performance PMLSM drives. While the inner electrical control is responsible for regulating the motor currents and, consequently, the electromagnetic force, the outer motion-control loops are responsible for ensuring that the actuator follows the desired position and velocity trajectories. A cascade control structure is therefore commonly adopted, with current, velocity and position loops arranged according to their respective dynamic requirements.

For trajectory-tracking applications, feed-forward compensation can further improve the response by providing part of the required control effort based on the desired trajectory, while the feedback controller compensates for disturbances, parameter variations and unmodelled dynamics. Yuan et al. (2021) proposed a high-precision motion-control scheme for a PMLSM combining model-based feed-forward control with feedback control. The experimental results demonstrated improved tracking performance for the PMLSM

servo system. These approaches demonstrate that the mechanical tracking performance of a linear motor cannot be considered independently from the electrical drive and its current-control dynamics.

For linear motor systems, feed-forward compensation is particularly important due to the high accelerations involved during motion. The feed-forward gains are designed improve the dynamic response by compensating the inertial and friction forces acting on the moving mass, thereby reducing the burden on the feedback controller and improving tracking accuracy, especially at high operating frequencies. The PID controller remains responsible for compensating modeling errors and unmeasured disturbances Guzmán and Hägglund (2024).

Considering the mechanical dynamics of a linear motor, the required actuation force can be expressed according to Newton's second law as

$$F_{act} = m_{mov}\ddot{x} + F_{fric} \tag{2.2}$$

where m is the moving mass, F_{act} is the actuator force, and F_{fric} represents the friction forces acting on the system. Assuming that the actuator follows the reference trajectory, the ideal feed-forward control input becomes

$$u_{ff} = m\ddot{x}_{cmd} + F_{fric}(x_{cmd}, \dot{x}_{cmd}) \tag{2.3}$$

where x, $\dot{x}$, and $\ddot{x}$ correspond to the reference position, velocity and acceleration, respectively Bolderman et al. (2021). This expression shows that the feed-forward action predicts the force required to overcome both inertia and friction before tracking errors develop.

In practical motion control applications, this principle is commonly implemented through velocity and acceleration feed-forward gains. Consequently, the PID controller is primarily responsible for correcting residual tracking errors and rejecting unmodeled disturbances.

2.4.4 Thermal Management and Protection Mechanisms

The thermal behaviour of electric motors represents an important limitation for their continuous and dynamic operation. Motors are expected to deliver their rated power while maintaining the temperature rise within specified limits, in order to prevent degradation of the insulation system, permanent magnet demagnetization, and damage to the stator windings. Consequently, thermal management and protection mechanisms are required to ensure safe operation under both continuous and transient operating conditions, and are therefore particularly relevant for compact, high-dynamic actuators such as the NLi120X.Demetriades et al. (2010).

2.4.4.1 Power Losses and Heat Generation

In electric motors, part of the supplied electrical and mechanical power is converted into heat. The main sources of losses in permanent magnet synchronous motors include winding losses, iron losses, and mechanical losses. Among these, the resistive losses in the stator windings are of particular relevance to the thermal behaviour of the motor, as they increase with the square of the current.

The resistive losses in the stator windings, resulting from the Joule effect, can be expressed as:

$$P_{\text{loss}} = \sum_i R_i I_i^2, \tag{2.4}$$

where R_i is the resistance of the corresponding winding and I_i is the RMS current flowing through it. Since the winding resistance varies with temperature, the electrical losses and the resulting temperature rise are coupled. Consequently, an increase in current results in a disproportionately higher heat generation within the windings Demetriades et al. (2010).

2.4.4.2 Heat Transfer and Thermal Behaviour

The heat generated within the motor is subsequently transferred from the windings to the surrounding components and environment through conduction and convection. The resulting temperature rise therefore depends not only on the generated losses, but also on the thermal characteristics of the motor and its cooling conditions.

The thermal response of an electric machine is transient, meaning that the winding temperature does not respond instantaneously to changes in the generated losses. Several approaches have been proposed to describe this behaviour and estimate the allowable operating time under overload conditions, including thermal time-rating methods and dynamic thermal models Buyukdegirmenci and Krein (2013). Real-time thermal models based on motor geometry and state-space representations have also been investigated to estimate the thermal state of electric machines during operation Demetriades et al. (2010).

2.4.4.3 Thermal Protection and I^2t Criterion

The electrical current applied to a motor is generally subject to predefined current limits, which determine the maximum allowable instantaneous electrical load. However, an instantaneous current limit alone does not fully describe the thermal constraints of the motor, since the temperature rise depends on both the magnitude of the current and the duration for which it is applied.

An increase in current leads to an increase in the Joule losses in the windings according to Equation 2.4. These losses are converted into heat, resulting in an increase in winding temperature. Therefore, higher currents impose a greater thermal load and can only

be sustained for a shorter period, whereas lower currents can be maintained for longer durations.

One established approach for representing the thermal load associated with the winding current is the I^2t criterion. Since the Joule losses are proportional to the square of the current, the accumulated thermal load can be represented by the time integral of the squared current,

$$I^2t = \int_0^t i^2(\tau)\,\mathrm{d}\tau. \tag{2.5}$$

where τ denotes the integration variable, representing the time instant over which the current is evaluated. The I^2t criterion therefore provides a simplified representation of the thermal loading associated with the motor windings. A higher current results in a faster accumulation of thermal load and can consequently only be sustained for a shorter duration, while a lower current produces slower thermal accumulation and can be maintained for a longer period. More detailed approaches may additionally account for the transient thermal response of the motor through thermal time constants or dynamic thermal models Buyukdegirmenci and Krein (2013).

In practical motor drives, the I^2t criterion can be implemented as a real-time thermal protection algorithm. The motor current is continuously monitored and used to estimate the accumulated thermal load, which is then compared with a predefined I^2t limit determined by the thermal characteristics of the motor and the configured operating limits. This approach is widely used in electric motor drives to account for the time-dependent nature of thermal loading and to permit temporary overload operation while maintaining the thermal load within defined limits Demetriades et al. (2010).

The specific implementation of the thermal protection mechanism in the NLi120X drive, including the configured current limits, the calculation of the available I^2t load, and the current monitoring procedure, is described in the methodology.

2.4.5 Kinematics of the movement

Engine speed is one of the main operating parameters of the steam engine, directly affecting the valve timing requirements and the overall operating conditions. Therefore, the actuator kinematics must be defined to evaluate the feasible operating range of the linear motor under representative steam engine operating conditions.

The linear motor follows a sinusoidal motion profile, which reduces acceleration peaks compared to trapezoidal and other motion profiles, thereby contributing to lower mechanical stress and increased system lifetime Cornetti (2025). Since both velocity and acceleration references are analytically known for a sinusoidal trajectory, they are directly used by the cascade control system.

The position of the actuator is therefore described by

$$x(t) = A\sin(2\pi ft) \tag{2.6}$$

where A is the motion amplitude and f is the operating frequency.

Differentiating the position equation yields the velocity:

$$\dot{x}(t) = A(2\pi f)\cos(2\pi ft) \tag{2.7}$$

and the acceleration:

$$\ddot{x}(t) = -A(2\pi f)^2\sin(2\pi ft) \tag{2.8}$$

From Equations 2.7 and 2.8, it follows that the maximum actuator velocity is proportional to both the stroke amplitude and the operating frequency, whereas the maximum acceleration increases with the square of the frequency. Consequently, high-frequency operation imposes considerably larger inertial loads on the actuator, making the evaluation of its force capability essential.

According to the feed-forward model introduced previously, the actuator force required to follow the prescribed trajectory is given by Equation 2.2. Although both inertia and friction contribute to the required actuation force, the inertial component becomes dominant as the operating frequency increases because it is proportional to f^2, whereas friction-related effects generally increase more slowly. Therefore, for the purpose of evaluating whether the actuator operates within its force capability, a first-order approximation considering only the inertial term is adopted.

The inertial contribution to the actuation force can be obtained from Newton's second law,

$$F_{inertial} = m_{\text{mov}}a \tag{2.9}$$

and substituting Equation 2.8 yields the instantaneous inertial force required to follow the sinusoidal trajectory:

$$F_{inertial}(t) = m_{\text{mov}}A(2\pi f)^2\sin(2\pi ft) \tag{2.10}$$

whose maximum magnitude is

$$F_{inertial,\text{max}} = m_{\text{mov}}A(2\pi f)^2 \tag{2.11}$$

This expression provides a first-order estimate of the peak force demand imposed on the actuator, obtained under the idealized assumption of continuous sinusoidal motion and should remain below the maximum force specified by the manufacturer (170 N according to NiLAB GmbH (2023)). It also highlights that doubling the operating frequency approximately quadruples the required peak actuation force.

2.5 Cycle-by-Cycle Variation Analysis

While the kinematic and force analysis presented above provides a first-order estimate of the actuator's capability to follow a single reference trajectory, actual operation involves continuous, repeated cycling, during which the actuator's behaviour may not remain strictly identical from one cycle to the next.

The concept developed in previous works is expected to operate over a high number of cycles while maintaining a constant IOD under the same operating conditions, thereby maximizing the efficiency of the machine.

A cycle-by-cycle (CBC) evaluation is a commonly used technique to assess how a certain parameter varies over consecutive cycles. This concept is widely used in ICE analysis, but can also be applied to expansion machines, where a large number of cycles is analyzed Chen et al. (2017), Engelmann et al. (2026).

One of the ways to quantify this variation is through the Coefficient of Variation (COV). The integral of the COV curve is commonly used as a criterion for quantifying cyclic dispersion. Furthermore, the COV of a parameter i is defined by Chen et al. (2017) as:

$$COV_i = \frac{\sigma_X}{\mu_X} \times 100 \tag{2.12}$$

Where σ_X and μ_X are sample standard deviation and mean of parameter X.

Although variable valve actuation and electric linear actuation have been extensively studied and applied in the context of internal combustion engines, their application to the intake control of expansion machines remains comparatively unexplored, particularly with respect to fully variable spool valve concepts. Similarly, while cascade control architectures and thermal protection mechanisms for permanent magnet linear motors are well established in the literature, their experimental characterization under the specific operating requirements of this application — namely the achievable combination of stroke amplitude, operating frequency, and moving mass — has not yet been addressed. This thesis therefore contributes to closing this gap by experimentally evaluating the NLi120X linear actuator as a candidate solution for this application, assessing its operating limits and the repeatability of the resulting valve timing through a cycle-by-cycle analysis of the intake opening duration.

Chapter 3

Methodology

The present experimental study focuses on the control system associated with the intake of the superheated steam expansion machine, particularly its valve actuation and control strategy. Accordingly, the test bench was adapted to meet the specific objectives of this study, while preserving the machine's overall operating principle.

3.1 Design Development

The test bench design is primarily based on the concept proposed by Cornetti (2025). However, several modifications were introduced to improve manufacturability and simplify assembly, particularly regarding the spool valve dimensions, fixation system, and sealing arrangement. The diameters of both the housing cylinder and the spool valves were increased to facilitate the manufacturing process, while preserving the operating principle and the aspects of the system relevant to the present characterization.

Given the trade-off between sealing effectiveness and friction losses discussed in Chapter 2, the selection of the piston ring material was an important design consideration for the present test bench. TEFLON (poly-tetrafluoroethylene, PTFE) piston rings were selected due to their low friction coefficient and good wear resistance under the operating conditions of the test bench. PTFE exhibits a dry sliding friction coefficient against metallic surfaces typically in the range of 0.05–0.10 (DuPont), substantially lower than most engineering polymers and comparable metals in unlubricated contact. To further reduce friction and wear at the ring–liner interface, a lubricant (silicon based spray - *Silikon-Spray, Atlas Spray, Germany*) was applied to the cylinder liner prior to testing.

Since the spool valve has a double-intake configuration, both piston rings alternately act as the primary sealing ring, depending on the direction of motion. Consequently, both grooves were designed with identical rectangular cross-sections to ensure consistent sealing behaviour regardless of which ring is active. Each groove has a depth of 3.0 mm and a width of 2.05 mm, providing sufficient support for the ring while allowing the required side clearance for proper sealing and free axial movement.

3.2 Experimental Setup

3.2.1 Structure of Test Bench

The test bench consists of two main components: the intake cylinder, including all the associated components and the NLi120X actuator, along with its connection to the +24 VDC power supply and Programming Box. The main cable connections are detailed in Appendix B.2.

Figure 3.1 illustrates the test bench setup and its components.

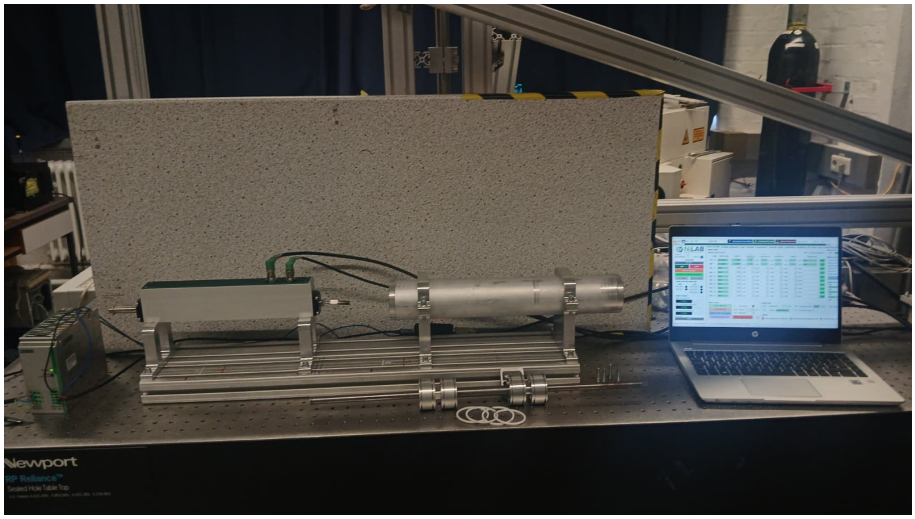
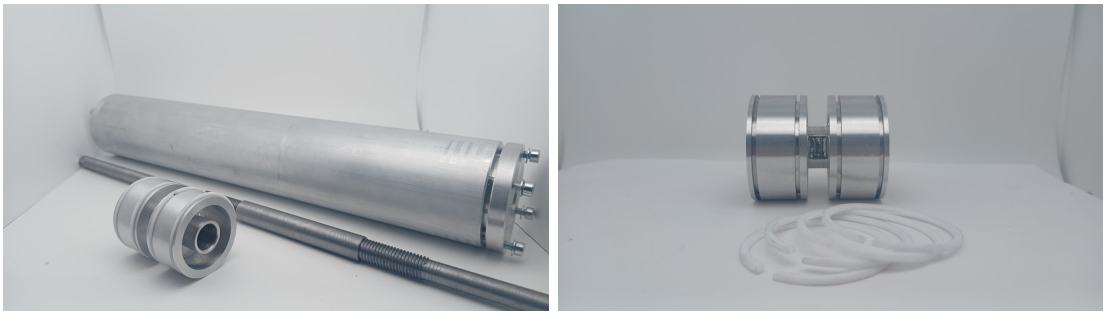


Figure 3.1: Test Bench Setup.

The shaft provided the connection to actuator, as well as the correct positioning and fixation of the spool valves. Its smooth movement is ensured by the incorporation of linear bearings, *PAB12-PP-AS*[1], installed within the housing caps, at both ends of the cylinder.

The fixation of the spool valves to the shaft is insured by a thread connection between the items, as can be seen in Figure 3.2.



(a) Housing, Shaft and Spool Valve. (b) Spool Valve and Piston Rings.

Figure 3.2: Detailed View of Test Bench Components.

[1] [https://medias.schaeffler.de/de/produkt/linear-motion/wellenfuehrungen/linear-gleitlager/standard-reihe/pab12-pp-as/p/1151417?utm]

The technical drawings of these components, as well as those of the remaining parts, can be found in Appendix B.1, and were done based on the standards Deutsches Institut für Normung (1989) and International Organization for Standardization (2011).

3.3 Design of Experiments

One of the main objectives of this experience is to investigate the physical and operational limits of the NLi120X actuator when applied to variable valve actuation systems. Beyond assessing its suitability for valve control, the study aims to evaluate the actuator's capability to operate under different loading conditions and valve configurations, including both single-valve and dual-valve arrangements. Particular attention is given to determining the maximum achievable actuation frequencies, stroke amplitudes, and operating conditions under which reliable and repeatable performance can be maintained. Table 3.1 presents the different configurations used in the experiment and respective masses.

For this reason, a broad operating range representative of different engine and steam admission conditions is studied. The setup includes a baseline configuration (referred to as *A*), which is not only studied independently but is also common to all experiments. This configuration includes a shaft and a connection bolt, which establishes the contact between the former and the electrical actuator.

Table 3.1: Experimental test configuration and respective moving masses.

Configuration	**Number of Valves**	**Number of Piston Rings**	**Mass [g]**
A	0	0	440
B	1	0	560
C	1	4	566.8
D	2	0	680
E	2	8	693.6

The mass of each piston ring is 1.7 g. The total moving mass for each configuration is obtained by adding the actuator slider (497 g). In addition to the range of operating frequencies and stroke amplitudes investigated, the effect of the piston rings on actuator performance is also studied, by comparing configurations with and without piston rings for both the single-valve and dual-valve arrangements (configurations B/C and D/E, respectively). This allows the additional friction introduced by the piston rings to be isolated from the effect of the added valve mass alone. The frequency is defined in rpm, with one revolution corresponding to one complete cycle. The actuator starts at Position 1, moves to Position 2, and then returns to Position 1. This sequence corresponds to one revolution.

In his predictions, Heyder (2025), targeted an amplitude of 20 mm (40 mm stroke) for the intake cylinder. However, to ensure safe operation of machine, lower amplitudes were initially taken into account, targeting 10, 12.5 and 15 mm.

Furthermore, for each configuration and each amplitude, a set of speeds was tested, going from 300 to 500 rpm with intervals between 100 and 25 rpm, with adjustments made according to motor conditions and limitations.

The variables continuously retrieved from the software included Set and Feedback Position, Speed Feedback, SVM amplitude, Target and Feedback Current.

During the operation of the motor, it was possible to obtain information about the Motor Load, Drive and Coil Temperature and instant RMS current evaluated over 1 s intervals. However the software does not allow this data to be extracted or uploaded directly. For this reason, rounded values were collected manually for every data sample.

The Motor Load, represents the percentage of the application process power to a motor's continuous power limits and was calculated according to Equation 3.1.

$$\text{Duty Motor Power} = (\frac{I_{RMS}}{I_{Cont}})^2 \times 100 \tag{3.1}$$

Where I_{RMS} is the root mean square current, the effective thermal average current actually consumed by the motor over a specific duty cycle or time period and I_{Cont} is the current required to heat the motor phases to their maximum operating temperature when the ambient temperature is 25 ºC, the motor is not moving, and there is no cooling NiLAB GmbH (2023).

Another parameter considered was the force executed by the motor. The total force is calculated based on the motor constant, $K_f = 10.895$ N/A$_{RMS}$ and given by Equation 3.2.

$$F = K_f \cdot I_{feedback} \tag{3.2}$$

Furthermore, the power being supplied was calculated, by multiplying Equation 3.2 by the actuator's velocity at each instant:

$$P_{mec} = F(t) \cdot v(t) \tag{3.3}$$

3.3.1 Thermal Management

The nominal and maximum current defined in the NiLAB Starter software define the physical limit and from this value, the I2T value is calculated, according to Equation 3.4. Consequently, every time the load conditions present a I2T current superior to this value, the overload error should be manifested.

$$I^2t_{value} = (I_{max}^2 - I_{nom}^2)t_{max} \times 1000 \tag{3.4}$$

I_{max} is the maximum current defined in motor parameters ($I_{max} = 15$ A), I_{nom} is the nominal current ($(I_{nom})_{ref} = 2.4$ A) and t_{max} is the maximal current time ($t_{max} = 1$ s).

The nominal current can be increased to a certain extent, with the manufacturer recommending a maximum increase of 10% compared with the manufacturer's reference values ($(I_{nom})_{ref}$). However, the allowable increase is ultimately limited by the resulting coil temperature, as higher nominal currents lead to increased thermal loading of the actuator. Therefore, any adjustment to the nominal current must ensure that the coil temperature remains within the permissible operating range. According to the software interface, temperatures below 60 °C are considered to be within the safe operating range, while temperatures between 60 and 80 °C correspond to the warning range. Although higher temperature can theoretically be reached, the manufacturer recommended a limit of 80ºC for both windings and drive temperatures NiLAB GmbH (2023).

To obtain the best possible result, the nominal current was then defined as 2.6 A, resulting in $I2t_{available} = 218240$ A^2s.

As mentioned, the interface returns I2t current at 1 s intervals, expressed in A_{RMS}. This value is calculated according to Equation 3.5 (assuming a RMS based method).

$$I_{RMS,1s}(t) = \sqrt{\frac{1}{1s}\int_{t-1s}^{t} I^2_{feedback}(\tau)d\tau} \tag{3.5}$$

Finally, the accumulation, that will dictate if (or when) the fault occurs is given by Equation 3.6. When this value reaches the $I^2t_{available}$, a current overload fault happens and the motor stops.

$$I2t_{acc}(t) = \int [I^2_{RMS,1s}(\tau) - I^2_{nom}]d\tau \tag{3.6}$$

It is worth noting that the terminology adopted by the software interface does not map directly onto the I^2t accumulation defined above. Specifically, the current value displayed at 1 s intervals is given in A_{RMS}, and is accordingly interpreted here as the RMS current computed over a 1 s window, as expressed in Equation 3.5. This value is then used to compute the I^2t accumulation given by Equation 3.6.

Three distinct quantities therefore appear throughout the analysis: the RMS current, the accumulated I^2t, and the available I^2t limit. The RMS current, expressed in A, corresponds to the effective current over a given time window. The accumulated I^2t, expressed in A^2s, results from integrating the squared current over time. The available I^2t sets the threshold used by the protection algorithm: once the accumulated value reaches this limit, the overcurrent protection trips and the motor is stopped.

3.3.2 Control Tuning

The experimental analysis is based on the measurement of actuator position, velocity, and current, which are evaluated against their corresponding reference trajectories. To minimize tracking errors and ensure consistent actuator performance, a control architecture was implemented, and adapted to different testing conditions.

The implemented control strategy consists of cascaded PID feedback loops responsible for regulating position, velocity, and current. Furthermore, feed-forward compensation based on velocity and acceleration references was incorporated to enhance the dynamic response of the system. Figure 3.3 illustrates the overall structure of the control loop.

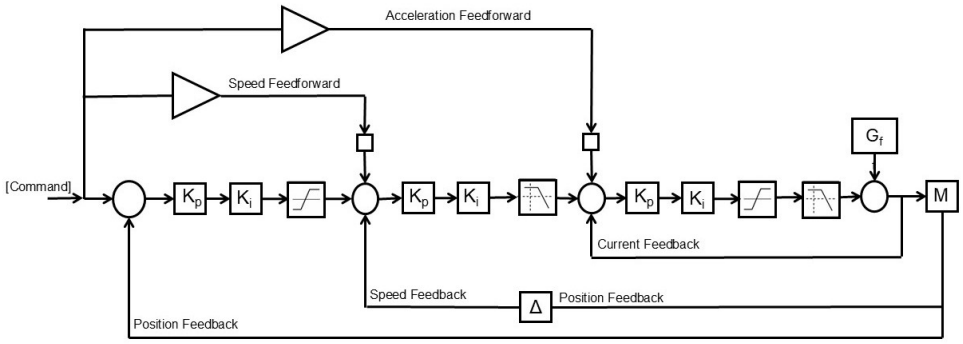


Figure 3.3: Control Scheme.

Reference for the Position, Velocity and Current are defined by $x_{cmd}(s)$, $v_{ref} = v_{lim} + v_{ff}$ and $i_{ref} = i_{filt} + a_{ff}$, and the rest of the equations that define the overall control loop for the actuation system are described in Table 3.2.

Table 3.2: Cascade Control System Equations (Laplace Domain).

Variable	**Error** (E)	(PI)	**Low-Pass Filter**
PCL	$E_x = x_{cmd} - x_f$	$V_{pi} = E_x \left(K_{p1} + \frac{K_i}{s}\right)$	$V_{ref_{lim}} = \text{Sat}(V_{pi}, \pm\text{Max})$
VCL	$E_v = v_{ref} - v_f$	$I_{pi} = E_v \left(K_p + \frac{K_i}{s}\right)$	$I_{filt} = I_{pi} \left(\frac{2\pi f_c}{s+2\pi f_c}\right)$
CCL	$E_i = i_{ref} - i_f$	$U_{pi} = E_i \left(K_p + \frac{K_i}{s}\right)$	$U_{motor} = \text{Sat}(U_{pi}, \pm I_{max}) \cdot \left(\frac{2\pi f_c}{s+2\pi f_c}\right) + \text{Grav}$

In the control system, velocity and current saturation blocks were also incorporated, in order to enforce the physical limits of the actuator. The velocity limiter prevents the position controller from requesting unattainable speeds, while the current limiter restricts the motor command to the maximum allowable current, which is directly related to the maximum actuation force.

Low-pass filters are included to attenuate high-frequency noise and smooth the control signals, improving the stability and robustness of the cascaded control architecture. A Gravity Feed-Forward [mA] option is also available in the control loop, but it was not used in this case since the actuator operates horizontally. Control parameters were adjusted to match the operating conditions, based on feedback provided by the manufacturer, although no significant changes relative to the reference values (presented in Appendix B.3) were

required. Overall, parameter variations remained below 10%, with only the Velocity Feed-forward gain, Position K_p, and Current K_i and K_p being modified.

3.4 Instrumentation

The design development was entirely made with PTC Creo Parametric 7.0.4.0. In the experiment, a +24VDC generator was used, the model being from Phoenix Contact. The actuator was the NLi120X-M12 version, coupled with the NL120-G695 slider, which has a mass of 0.497 kg and a total length of 695 mm. When combined with the NLi120X actuator, the slider provides a maximum stroke of 374 mm.

and it was controlled with the NiLAB Starter in the version 2.4.4.3. The software was used in *Expert Mode*, whose access was provided by the company itself. A firmware was also provided, that included bug corrections, in the version 623E_FW.S19.

The Programming Box DA012060 acts as the communication and power interface for the NLi120X motor. It provides the motor with a 24 VDC supply, enables USB communication with the control software, and exposes the digital input/output signals for configuration and testing.

3.4.1 Position Reference and Calibration

The position feedback provided by the NLi120X's integrated linear encoder relies on a factory pre-calibrated sinusoidal measuring principle (SIN/COS 1Vpp), in which one full sine period corresponds to one magnetic pole pitch of 60 mm, as specified in the actuator datasheet (Appendix A.2). No additional recalibration of the encoder was performed beyond this factory-provided reference.

Prior to every sample collected, a homing routine was executed to establish an absolute position reference. The raw encoder reading was subsequently translated so that the starting point of each test corresponded to a position of 0, ensuring a consistent zero reference across all tested configurations and operating conditions.

The commanded actuator positions were defined through two discrete tasks transmitted via Modbus: Task 1, corresponding to a fixed reference displacement of 5 mm, common to all tested conditions; and Task 2, corresponding to the variable target displacement under investigation (25, 30, or 35 mm, depending on the tested stroke amplitude), both defined relative to the homed zero reference.

All data collections were made with a sampling time of 2 ms and a record length of 1 s. The temporal resolution of the position commands is additionally limited to 1 ms by the programming unit.

In the Test Bench, a scale used to measure the mass of the components, from the manufacturer August Sauter KG (Ebingen/Württemberg, Germany), a mechanical dial platform scale, with a maximum capacity of 20 kg, a scale division of 10 g and the reading

uncertainty (half of the scale division) of ±5 g. For the lighter components, an analytical balance (Entris 224-1S, Sartorius Lab Instruments GmbH Co. KG, Göttingen, Germany), with a maximum capacity of 220 g and a readability of 0.1 mg, was used for the measurements.

The parts used in the test bench set up were manufactured at the workshops of Institut für Kolbenmaschinen at KIT (IFKM). The tolerances and fitting norms used are detailed in the respective technical drawings (Appendix B.1).

3.5 Uncertainty Analysis

The mass measurements used to define the moving-mass configurations (Table 3.1) carry an absolute uncertainty of ±5 g, corresponding to a relative uncertainty ranging from approximately 0.7% (configuration E, 693.6 g) to 1.1% (configuration A, 440 g).

The motor force reported throughout Chapter 4 is calculated from the feedback current according to Equation 3.2 , using the manufacturer-specified force constant $K_f = 10.895$ $\mathrm{N/A}_{rms}$ (Appendix A.2). The datasheet does not specify a tolerance for K_f nor the resolution of the current feedback reported by the drive; consequently, the force values presented in this work should be understood as nominal estimates based on the manufacturer's stated force constant, rather than values with a fully quantified measurement uncertainty.

Similarly, while the encoder's measuring principle (one sine period per 60 mm pole pitch) is specified in the datasheet, the effective spatial resolution of the position feedback depends on the interpolation performed internally by the drive electronics, which is not disclosed in the available documentation. The step-like position profile observed in Chapter 4 provides empirical evidence of this finite resolution, but its numerical value could not be independently determined or verified within the scope of this work.

The temporal resolution of the position commands, limited to 1 ms by the programming unit, represents an additional source of uncertainty affecting the timing of the reported valve events (IOT, ICT, and IOD), separate from the spatial resolution of the position feedback itself.

Overall, the quantifiable uncertainty in this study is limited to the mass measurements (±5 g); the remaining sources discussed above (force constant tolerance, encoder interpolation resolution, and current sensing resolution) could not be quantified from the available manufacturer documentation, and are acknowledged here as limitations of the uncertainty characterization.

Chapter 4

Results and Discussion

4.1 Operation Limits

The experimental analysis focused on characterizing the operating limits and position-tracking accuracy of the NLi120X linear motor. In particular, the influence of velocity, force demand, and thermal limitations on the actuator's performance was investigated.

Throughout the testing phase, it was verified that the main limitation was imposed by the current overload protection algorithm *Overload I2T*, which is described in detail in Section 2.4.4. The results show that the higher the amplitude and/or velocity, the sooner the algorithm is triggered. This limitation was confirmed by the manufacturer, who clarified that it originates from the thermal characteristics of the motor rather than from the available electrical power, so a higher-current supply would not extend the operating range (Appendix B.3). The *I2T value* and the motor load are good indicators of the current operating state of the motor. The protection mechanism is activated when the I2T value remains above its limit for more than 1 s. The motor load, given by Equation 3.1, was monitored throughout the test campaign, with approximate values collected for each sample and presented in Figure 4.1.

The results indicate that motor load generally increases with increasing operating speed. Higher motion amplitudes also result in increased motor load, causing the current overload limit to be reached at lower speeds.

It is important to distinguish that the behaviour with one or two valves differs from that of the no-valve configuration. In the former two cases, it is clear that the amplitude of motion has a more significant impact on motor load than the change in mass, as configurations C and E both present lower loads when compared with their counterparts at lower amplitudes. In configuration A, the impact of amplitude is still visible, but is not as pronounced as in the former cases.

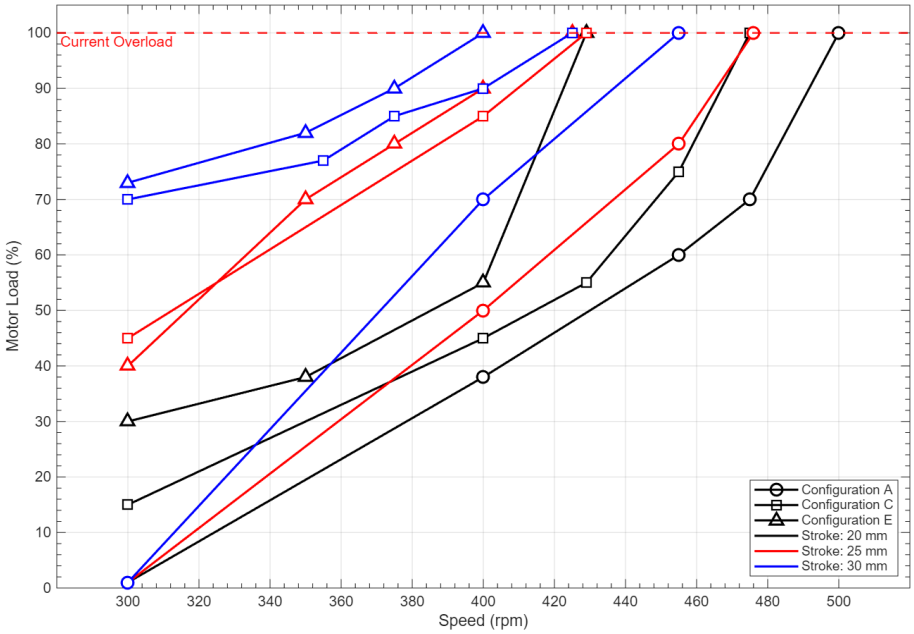


Figure 4.1: Motor load of the actuator for different speeds and mass configurations.

The effect of mass is nevertheless very noticeable. For example, at 300 rpm and for a stroke of 20 mm, the introduction of the two spool valves caused an approximately 35% increase in motor load compared to the configuration without valves, highlighting the significant impact of the added mass. This effect is, as expected, enhanced as the amplitude increases, with increases of approximately 40% and 70% for strokes of 25 mm and 30 mm, respectively. This progressive increase is also noticeable with increasing speed. This behaviour can be explained by the higher current demand, which is directly related to the force required to accelerate the higher moving mass, according to Equation 2.9.

The increasing motor load with speed, common to all configurations and amplitudes, is a reflection of the higher acceleration. The acceleration is calculated using Equation 2.8 and is proportional to the amplitude and the square of the frequency.

Considering the results for the largest amplitude, for both the one and two valve configurations, the motor load already starts at a concerning value, exceeding 70% at 300 rpm. This indicates operation with a reduced margin to the motor's thermal limit, with the overload limit being reached shortly thereafter. This is a very relevant analysis, as it represents the absolute limit of this study.

It could furthermore be expected that an increase in stroke would not be feasible within the investigated speed range, even though previous works targeted a stroke of 40 mm. The operating speed would have to be significantly reduced to prevent the I2T fault.

A possible alternative could therefore be to modify the design in order to reduce the stroke, even if accompanied by a slight increase in mass. This could be advantageous, as the results suggest that the reduction in stroke may compensate for the additional mass,

given the strong influence of amplitude on motor load and consequently, on the speed at which the overload occurs.

Overall, the permissible operating speed decreases as the moving mass and stroke amplitude increase. The last point recorded before the activation of the protection mechanism is defined in this analysis as the operating limit for each amplitude, speed, or valve configuration. These values are detailed in Appendix C.1.

It is also important to note that the closer the motor load corresponding to the frequency limit is to 100%, the smaller the margin to the thermal overload limit. Therefore, in some cases, the maximum achievable speed could potentially be slightly higher. However, within the investigated speed range, a minimum increment of approximately 25 rpm was considered between consecutive test points, considering the overall operating requirements of the expansion machine.

In addition, to assess the electrical effort required by the actuator, the force and power generated by the linear motor were calculated from the feedback current and velocity, according to Equations 3.2 and 3.3. The profiles presented in Figure 4.2 reflect an alternating peak behaviour, with these peaks occurring around the reversal points, where the acceleration reaches its highest values. Considering the maximum values obtained, a clear increase can be observed with both motion amplitude and speed, as expected.

The predicted peak inertial force (Equation 2.11) can be deducted and compared for configuration E at the 30 mm stroke: 17.4 N vs. approximately 31 N at 300 rpm, and 27.2 N vs. approximately 54 N at 375 rpm, a factor of 1.8 and 2 higher than predicted in both cases. However, the increase in force with speed is relatively consistent with the inertial model: between 300 and 375 rpm (f ratio of 1.25), the model predicts a 1.56 increase, and a increase of 1.74 times (30 N to 54 N) was registered, with the persistent offset attributed to velocity-dependent friction effects not captured by the purely inertial model. Since the inertial component alone already explains the observed scaling of force with speed, the persistent offset between predicted and measured values, present at both speeds and of comparable relative magnitude, is attributed primarily to friction at the test bench interface, rather than to speed-dependent effects such as the dwell-time interruption of the trajectory.

The mechanical power profiles provide a complementary assessment of the actuator's mechanical demand, as power depends on both the motor force and instantaneous velocity. As shown in Figure 4.2, the peak mechanical power increases significantly with both operating speed and stroke. For the 30 mm stroke, the peak power increases from approximately 15–16 W at 300 rpm to 33–34 W at 375 rpm, corresponding to an increase of approximately 2.2 times.

This increase is consistent with the expected dynamic behaviour of the reciprocating system. Since the inertial force scales with f^2 and the velocity with f, the inertial contribution to mechanical power is expected to scale approximately with f^3. Thus, increasing the speed by a factor of 1.25 predicts a power increase of 1.95 times, which is close to the

measured value. The results therefore confirm the strong influence of operating speed on the mechanical power demand.

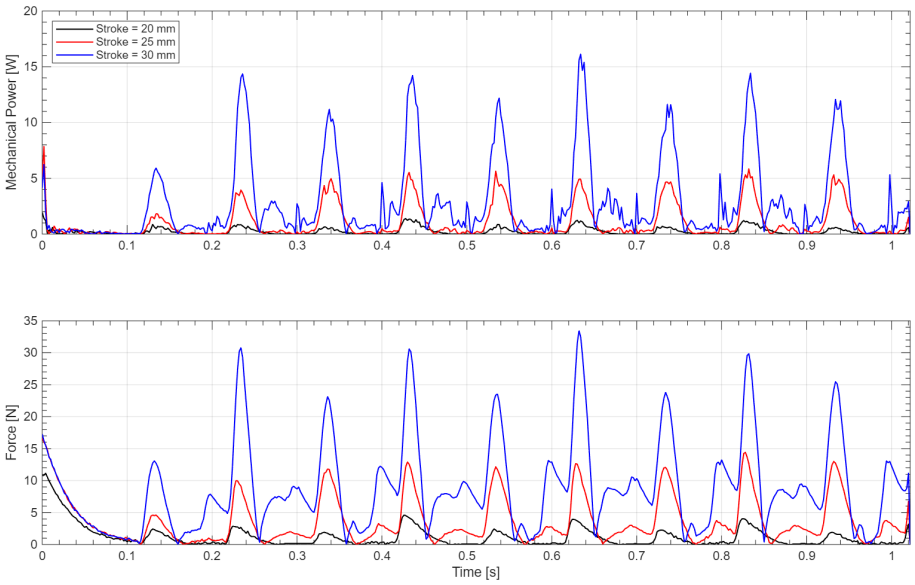
The results also reveal an asymmetric behaviour between the two directions of motion, most evident for the 25 and 30 mm strokes, where the force peaks, directly proportional to the measured current, alternate between higher and lower values. As shown in Figures 4.2a and 4.2b, for the 30 mm stroke the higher peaks reach approximately 30 N and 54 N at 300 and 375 rpm, respectively, while the corresponding lower peaks are approximately 23 N and 30 N. This suggests the motor faces greater resistance in one direction, demanding higher current to follow the target trajectory.

At 375 rpm, the force profile within each cycle also becomes visibly more complex: instead of a single, well-defined peak, a secondary, smaller peak emerges shortly before the main one, particularly for the 30 mm stroke. This double-peak pattern is much less pronounced at 300 rpm, where the force rises and falls more smoothly. Its emergence at higher speed suggests an increasing contribution of dynamic effects superimposed on the main frictional resistance, although confirming its exact origin would require further analysis correlating the force signal with the actuator's position and velocity profiles.

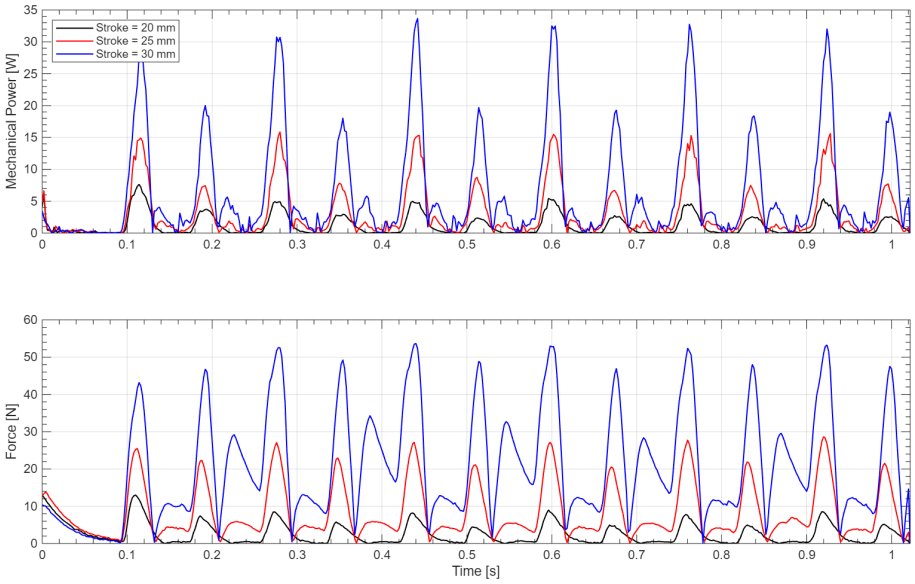
This is confirmed in Figure 4.3, where the motor force is plotted against actuator position, forming a hysteresis loop for each stroke. The differing peaks in the positive and negative directions likely originate from a combination of inertial and frictional effects, the latter possibly linked to mechanical asymmetries in the test bench, such as misalignment.

To determine whether this asymmetry originates from the actuator itself or from the valve configuration, a test was performed without any mass attached, under similar conditions of stroke and speed (30 mm, 375 rpm), shown in Figure 4.4. Even without payload, a measurable force asymmetry persists between the two motion directions, with the positive force lobe reaching a higher peak over a narrower position range than the negative lobe. This indicates that the asymmetry is not solely a consequence of the valve configuration, but is already present, to a lesser extent, in the actuator and guiding system itself, and is subsequently amplified once the valve and additional mass are introduced.

This amplification is consistent across the tested operating speeds and stroke amplitudes. At 300 rpm, the force loops remain relatively compact for all three stroke amplitudes, and the asymmetry between the two motion directions, while present, is comparatively modest. At 375 rpm, the loops expand considerably in both amplitude and area, and the asymmetry becomes markedly more pronounced. A similar dependence is observed with respect to stroke amplitude at a fixed speed: the 20 mm stroke consistently produces the most compact and closest-to-symmetric loops, while the 30 mm stroke produces the largest loop area and the most pronounced asymmetry. This trend indicates that the directional asymmetry is amplified by the same factors that increase the overall actuator loading, namely higher operating speed and larger stroke amplitude, rather than being an independent or condition-invariant effect.

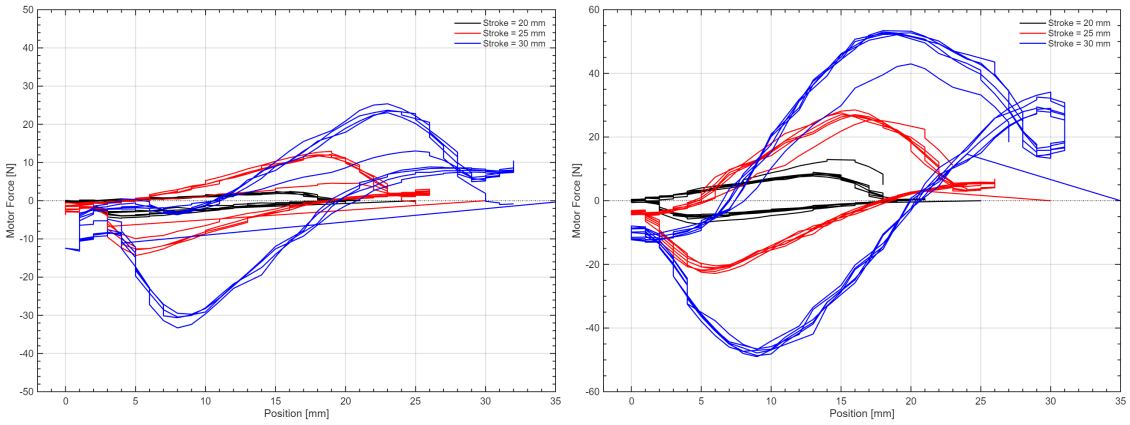


(a) 300 rpm.



(b) 375 rpm.

Figure 4.2: Mechanical power and motor force for different strokes and amplitudes. (Configuration E).



(a) 300 rpm. (b) 375 rpm.

Figure 4.3: Motor force as a function of position feedback for configuration E.

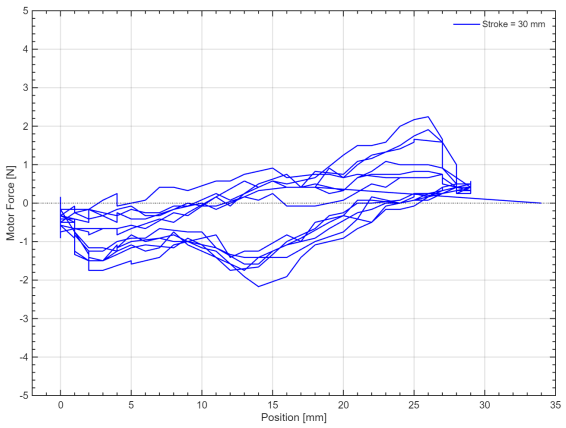
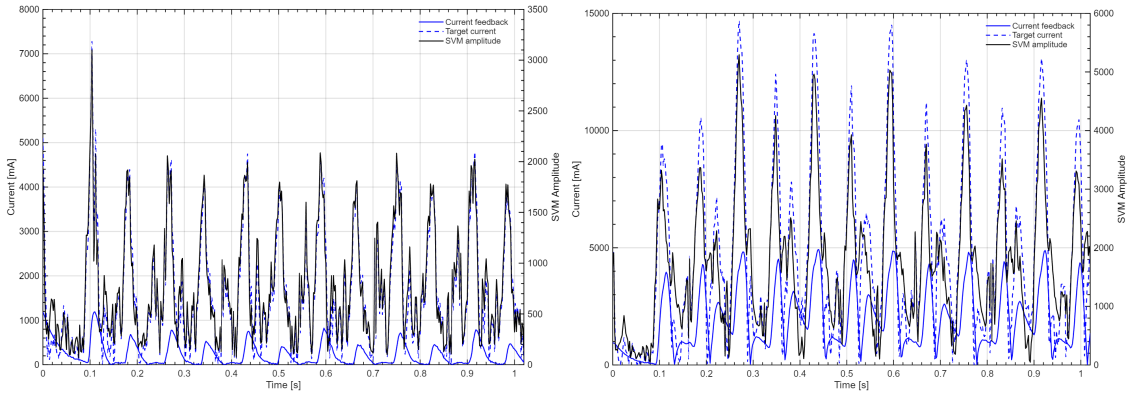


Figure 4.4: Motor force as a function of actuator position for the unloaded actuator (no valve or additional mass attached), at a 30 mm stroke and 375 rpm.

The increase in motor force observed at higher speeds and strokes is accompanied by an increase in the electrical demand of the actuator. As the required motor force increases, the controller increases the target current supplied to the motor. The higher current demand is reflected in the SVM amplitude, as the inverter must apply a greater voltage command to achieve the required motor current, which is visible in Figure 4.5. This relationship is particularly evident for the 30 mm stroke at 375 rpm, where the largest peaks in target current and SVM amplitude are observed.



(a) Stroke:20mm (b) Sroke:30mm

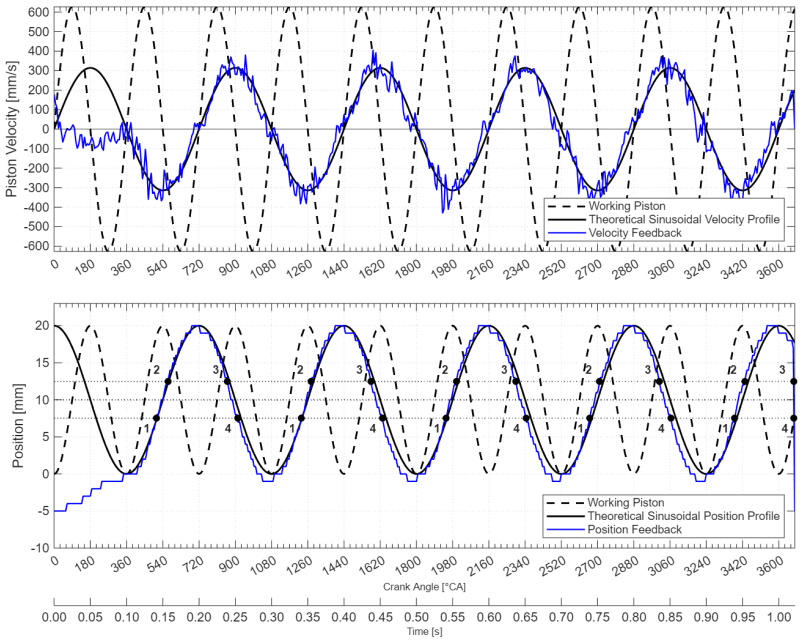
Figure 4.5: Current Target, Feedback and SVM amplitude for configuration E, at 375 rpm.

The velocity and force physical limits, detailed in the technical information of the actuator were not reached within a large margin. The actuator can only reach high speeds when set to extremely low amplitudes, which is not representative of this application.

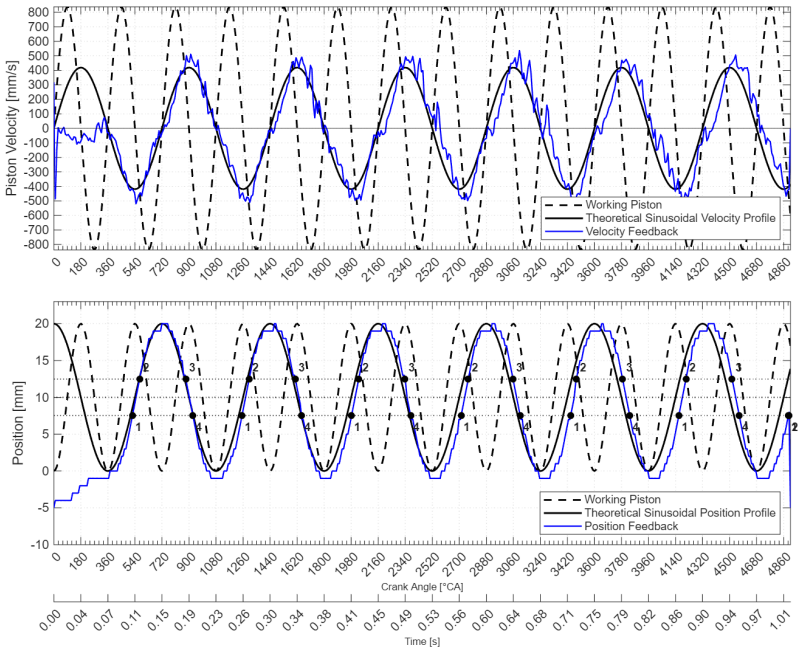
4.2 Velocity and Position Synchronization

The position and velocity profiles were evaluated by comparing the experimental response with an ideal sinusoidal function, providing a theoretical reference for assessing the synchronization and trajectory tracking performance of the actuator. In a preliminary analysis, the velocity profile exhibits a relatively irregular and oscillatory behaviour across all operating conditions, with more pronounced fluctuations around the maximum and minimum velocity points. Despite these irregularities, the overall profile remains approximately sinusoidal, as expected. As the operating frequency increases (Figures 4.6b, 4.7b), a progressive phase delay between the experimental and ideal sinusoidal profiles becomes evident. The delay accumulates over successive cycles, leading to an increasingly larger deviation from the ideal profile over time.

A key limitation of the actuator is the mandatory pre-definition of a *waiting time* of, at least, 6 ms. This corresponds to 3 ms of dwell time at each target position. The imposed dwell time introduces an interruption in the continuous motion, requiring the actuator to remain at zero velocity at each target position. Consequently, oscillations around 0 m/s become increasingly pronounced at higher operating frequencies, as the actuator must transition more rapidly between the motion phases while maintaining the prescribed dwell time. Looking at the corresponding instant in the position profile, this phenomenon is observed at the maximums, where the actuator reaches the targeted positions.

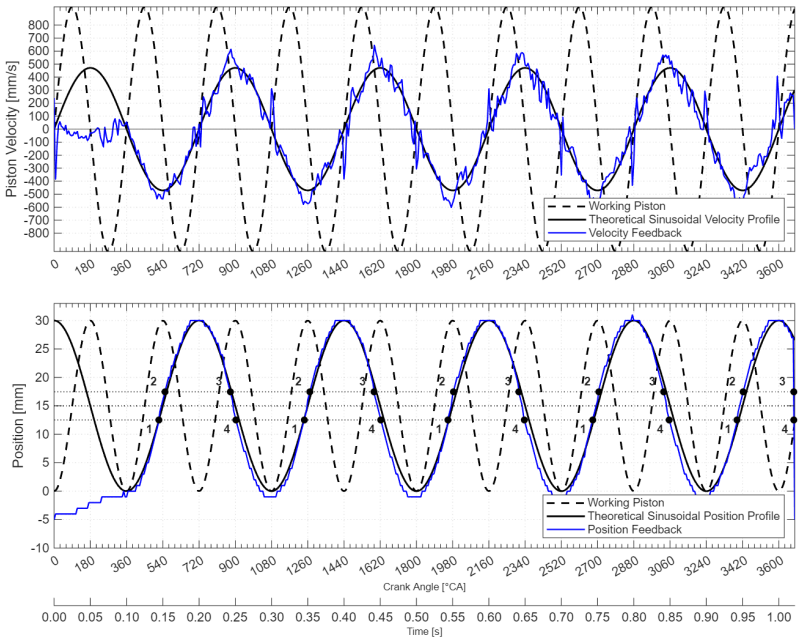


(a) 300 rpm

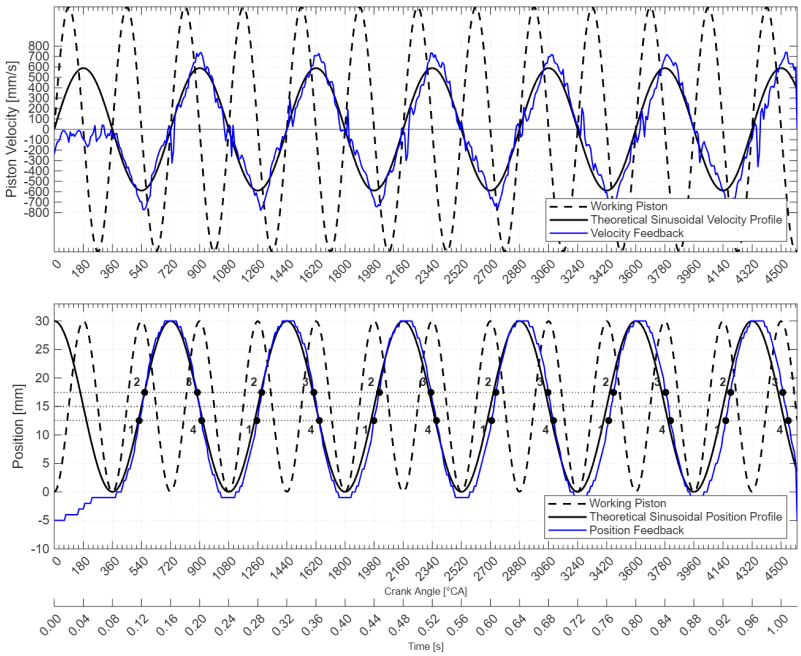


(b) 400 rpm

Figure 4.6: Comparison between the theoretical sinusoidal reference and the measured intake valve velocity (top) and position (bottom) for configuration E with a 20 mm stroke.



(a) 300 rpm



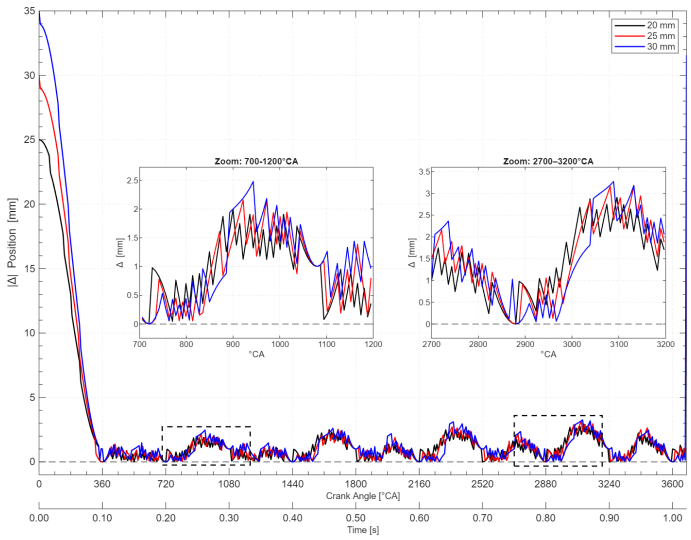
(b) 375 rpm

Figure 4.7: Comparison between the theoretical sinusoidal reference and the measured intake valve velocity (top) and position (bottom) for configuration E with a 30 mm stroke.

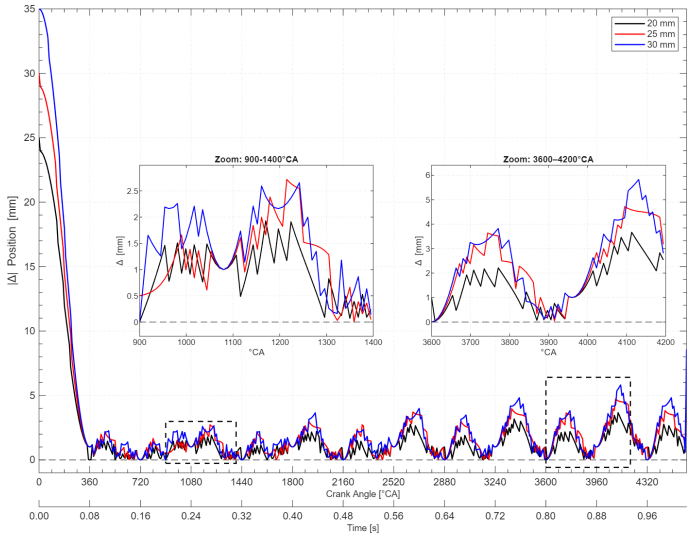
In this representation, points 1 and 3 correspond to the inlet opening timing (IOT), and points 2 and 4 to inlet closing timing (ICT). The neutral point (10 mm or 15 mm depending on the case) corresponds to a fully open valve configuration.

This position is reached approximately at the moment when maximum velocity is obtained, taking place once every full cycle of the working cylinder.

Figure 4.8 illustrates the evolution of error over time, for different frequencies and amplitudes. A clear trend can be identified, as the error exhibits an oscillatory profile, with alternating higher and lower amplitudes and an overall progressive increase over time. The peak error regions occur in the interval between ICT (Position 4) and the following target position. This result further confirms the non-symmetrical behaviour identified previously, with the descending trajectory showing larger discrepancies from the expected sinusoidal profile. When comparing the timing of the force peaks in Figure 4.2 with the peaks identified in Figures 4.8, the higher force peaks tend to coincide with the larger error peaks, with the same behaviour also observed for the lower peaks.



(a) 300 rpm



(b) 375 rpm

Figure 4.8: Difference between feedback position and sinusoidal function for different speeds.

The position error at critical points was also analyzed, with particular focus on the error at IOT and ICT and its evolution over time, as presented in Table 4.1.

Table 4.1: Position errors at IOT (1&3) and ICT (2&4), and their differences between the 1st and 4th cycles.

Stroke [mm]	Speed [rpm]	Cycle	1	2	3	4
20	300	1°	0.5	0.5	1.5	1.5
		4°	1.5	1.5	2.5	2.5
		Δ	1.0	1.0	1.0	1.0
	400	1°	1.3	0.2	0.1	0.3
		4°	3.3	2.3	2.8	1.7
		Δ	2.0	2.1	2.7	1.4
30	300	1°	0.2	1.2	0.8	2.2
		4°	0.8	2.2	2.2	3.2
		Δ	0.6	1.0	1.4	1.0
	375	1°	0.8	0.2	0.6	1.6
		4°	3.6	3.2	2.8	1.4
		Δ	2.8	3.0	2.2	-0.2

The results indicate a general increase in the position error over time, observed by comparing the errors at the selected positions between the 1^{st} and 4^{th} cycles of operation.

For the first case analysed (stroke = 20 mm and speed = 300 rpm), the measured error increases by approximately 1 mm at all four positions. At the same stroke but 400 rpm, the increase in absolute error is more pronounced, reaching approximately 2 mm at positions 1 and 2 and more than 2.7 mm at position 3 — suggesting that the higher operating speed drives a greater deviation from the theoretical sinusoidal trajectory over consecutive cycles. The 30 mm stroke at 300 rpm behaves differently: the error at the ICT positions tends to increase, while it decreases at the IOT positions, so the error does not evolve uniformly throughout the cycle.

Comparing the two operating conditions closest to the respective motor limits, the errors at positions 1, 2 and 3 are slightly lower for the smaller stroke amplitude. At position 4, however, the trend reverses, with a lower error for the 30 mm stroke. Increasing the stroke therefore does not translate into a consistent increase or decrease in position error across the trajectory.

The highest errors occur for the largest stroke and speed combination (30 mm and 375 rpm), exceeding 3 mm — more than 10% of the commanded 30 mm stroke, a significant deviation for an application that requires accurate reproduction of the prescribed trajectory.

Overall, the evolution of the position error is not easily predicted from the tested operating conditions: it follows no consistent trend with either stroke or speed, and it also depends on the position within the cycle. Position 4 illustrates this well, with the error decreasing at higher speed for both stroke amplitudes. Figures 4.6b and 4.7b suggest that this behaviour is linked to the oscillatory response of the actuator, and analyzing the

position error continuously over time, as in Figure 4.8, makes the origin of these variations clearer.

One of the main causes of the discrepancies with the sinusoidal function was, as previously mentioned, the mandatory dwell time. This limitation originates from the communication method used in the test setup, namely Modbus. The communication is task-based, which imposes a minimum time interval between successive position commands and therefore prevents the actuator from continuously following the desired sinusoidal trajectory. A possible solution to overcome this limitation would be to implement a communication protocol such as EtherCAT or CANopen, which supports shorter communication cycle times and allows successive position setpoints to be interpolated within the drive. This would reduce the discretization effects associated with the current Modbus implementation, resulting in a smoother and more accurate sinusoidal motion profile.

It is also important to note that the position curve exhibits a step-like profile, which results from the resolution limitations of the motor. Finally, the initial actuation period is not analysed in detail, as it corresponds to the movement towards the first target position, which is reached after approximately 0.1 s.

Beyond the position error, the repeatability of the actuator motion can be assessed through the variation in the intake opening duration(IOD). Table 4.2 presents the statistical analysis of the IOD, obtained from the measured valve opening and closing timings over four consecutive cycles. For each operating condition, the mean IOD, standard deviation, and coefficient of variation (COV) were calculated for the two valve intervals, 1–2 and 3–4.

Table 4.2: Statistical analysis of the measured inlet opening duration (1–2) and (3–4).

Stroke [mm]	Speed [rpm]	Indicator	1–2	3–4
20	300	μ [ms]	10	9.1250
		σ [ms]	0	1.0308
		COV [%]	0	11.3
	400	μ [ms]	14.500	15
		σ [ms]	1.0	1.1547
		COV [%]	6.9	7.7
30	300	μ [ms]	8.1250	8.2500
		σ [ms]	0.4787	0.8660
		COV [%]	5.9	10.5
	375	μ [ms]	6.8750	7.0000
		σ [ms]	0.7500	0.7071
		COV [%]	10.9	10.1

The number of cycles captured per sample is constrained by the data acquisition software, which does not allow new samples to be triggered once the actuator motion has started. Four cycles per sample were used consistently across all tested conditions to preserve the validity of the comparison between them. As a result, the statistics reported in

this section should be interpreted as preliminary estimates: confidence intervals on σ and COV cannot be reliably calculated at this sample size, and a larger dataset (N 30) would allow a more robust statistical characterization.

The mean IOD values obtained for the two intervals are generally close under the same operating condition. The differences between intervals 1–2 and 3–4 remain below 1 ms for all tested conditions, indicating consistent opening durations between the two valve openings. For instance, at 20 mm and 300 rpm, mean IOD values of 10.00 ms and 9.125 ms were obtained for intervals 1–2 and 3–4, respectively, while at 30 mm and 375 rpm the corresponding values were 6.875 ms and 7.00 ms. This agreement indicates that, despite variations in mean IOD across operating conditions, the two valve opening events exhibit similar durations within a given condition.

The standard deviation and COV provide a measure of cycle-to-cycle repeatability of the opening duration. Standard deviation values range from 0 to approximately 1.15 ms. The lowest variability corresponds to the 1–2 interval at 20 mm and 300 rpm, where a standard deviation of 0 ms was obtained, indicating identical IOD values across the four analysed cycles. The highest standard deviation, 1.155 ms, was obtained for the 3–4 interval at 20 mm and 400 rpm. The corresponding COV values are generally below 11%, with the highest value, 11.30%, occurring for the 3–4 interval at 20 mm and 300 rpm. As COV is normalized by the mean IOD, its magnitude should be interpreted in conjunction with the standard deviation and mean values: a standard deviation of 0.75 ms corresponds to a COV of approximately 10.9% when the mean IOD is 6.875 ms, whereas a standard deviation of 1.00 ms corresponds to a lower COV of 6.9% when the mean IOD is 14.5 ms.

The 3–4 interval generally exhibits higher COV values than the 1–2 interval, a trend observed in three of the four tested conditions. The exception is the 30 mm stroke at 375 rpm, where the COV values are 10.91% and 10.10% for intervals 1–2 and 3–4, respectively. This indicates that the repeatability of the IOD associated with the 3–4 interval is generally slightly lower than that of the 1–2 interval. Nevertheless, the relatively close mean IOD values between the two intervals suggest that this difference stems mainly from cycle-to-cycle variability rather than a systematic difference in average opening duration.

Overall, the results show that the actuator reproduces similar mean opening durations for the two valve events, although a degree of cycle-to-cycle variation persists. Since the IOD directly determines the duration of the steam admission event, this variability should be taken into account when evaluating the consistency of valve operation and its potential effect on the expansion process.

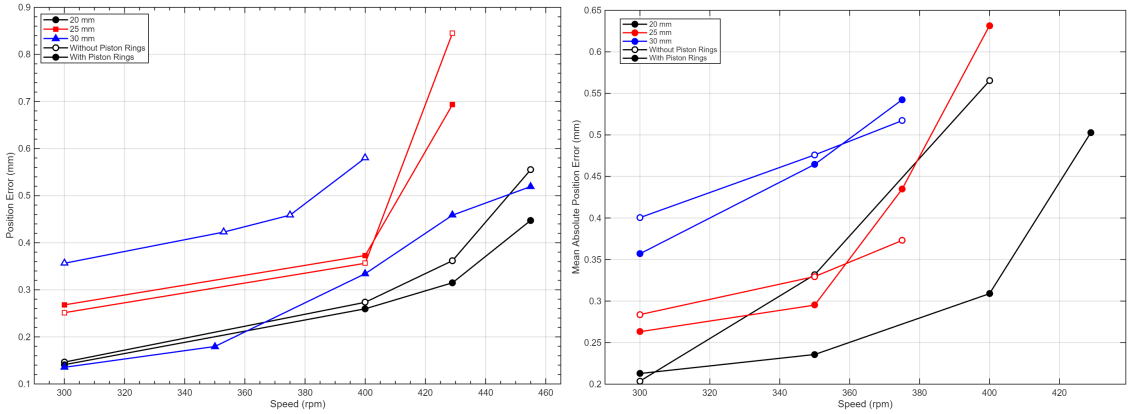
These results can be placed in a system-level context using simulation data from related work within the same research group. Eirich (2024) reports that a sinusoidal valve motion profile — kinematically comparable to the actuator used here — already incurs a baseline penalty of 5% in mass flow and power relative to an idealized instantaneous valve opening. Building on this, Heyder (2025) provides a simulated torque sensitivity to intake-side opening duration at the target application speed (1400–1500 rpm); converting

the measured IOD variability (COV 11%, Table 4.2) into crank-angle terms and applying this sensitivity suggests an additional cycle-to-cycle torque and power variability on the order of 10–15% at the target operating point. This estimate is necessarily approximate, as it transfers a sensitivity derived from simulated target-machine geometry onto timing variability measured on the actuator test bench at lower speeds, but it indicates that the observed positioning variability is not merely a bench-level metrology concern: it corresponds to a plausible, non-negligible variation in delivered power at the level of the complete expansion machine.

4.3 Friction Analysis

Friction represents an important source of mechanical loading in the present test bench, directly affecting the force and current required to follow the commanded trajectory. TEFLON piston rings (four per valve) were incorporated into the design, as described in Chapter 3, allowing their contribution to the overall friction to be isolated and assessed experimentally.

Figure 4.9 presents the mean effective position error, defined as the deviation between the set position commanded to the actuator and the corresponding feedback position, calculated for each tested operating condition. By comparing configurations with and without piston rings under otherwise identical conditions, this analysis isolates the effect of the piston rings on the actuator's position-tracking performance.



(a) Single Valve Arrangement. (b) Double Valve Arrangement.

Figure 4.9: Mean Effective Position Error as a function of Operating Conditions.

The introduction of piston rings was found to affect the mean effective position error, although the magnitude and direction of this effect vary with the operating condition. In the single-valve configuration, differences between the cases with and without piston rings are generally small at lower stroke amplitudes but become more pronounced at larger ones. A similar trend is observed for the two-valve configuration, where the effect of the piston rings is more evident under some of the higher-load conditions.

The increase in position error observed in several configurations can be linked to the additional friction introduced by the piston rings, which opposes the actuator motion and thus increases the effort required to follow the target trajectory. However, the lack of a consistent increase across all conditions suggests that friction alone does not account for this behaviour; rather, it results from the combined effect of friction, inertial loading, and the control system's response.

Overall, the piston rings add to the actuator load and can degrade position tracking under more demanding conditions. Their influence, however, remains condition-dependent and appears secondary to that of the system's overall dynamic load.

4.4 Thermal Analysis

The temperature of both the motor and the windings was monitored throughout the test sessions. Considering the entire test phase, the drive temperature ranged from a minimum of $T_{\min} = 31°\text{C}$ to a maximum of approximately $T_{\max} = 60°\text{C}$, while the coil temperature varied between 25°C and 55°C. Although temperature monitoring during the tests had to be performed manually, the software continuously recorded the temperature over longer time periods. Figure 4.10 exemplifies the temperature and I^2T value evolution over one test session of approximately 30 min. These results indicate that, within the duration and operating conditions of the tests, the motor remained within a safe temperature range. However, a clear accumulation of heat over time can be observed, which is expected given the lack of active cooling.

Comparing the temperature evolution with the I^2T values recorded, the temperature peaks occur with a slight delay relative to the I^2T peaks which shows that temperature does not respond instantaneously to the fluctuations in the I^2T value. This can be attributed to the thermal inertia of the system, as the heat generated during periods of high current demand requires time to be transferred and dissipated. It can also be observed that periods with zero I^2T values, corresponding to interruptions in the system, are not sufficient to reduce the temperature by a significant amount.

These results highlight the relationship between the electrical effort imposed on the actuator and its thermal response.

The temperature range observed throughout the tests indicates that the motor remained within a safe operating range under the tested conditions. This can be attributed, to the I^2T protection implemented in the drive, which limits the duration of operation under high-current conditions (the heat generated in the windings due to Joule Effect is proportional to I2T). Consequently, prolonged operation at elevated current levels is interrupted by an overload fault before the motor temperature can reach potentially concerning values. Therefore, the temperature behaviour observed during the tests is consistent with the protection mechanism implemented in the drive and the operating conditions investigated.

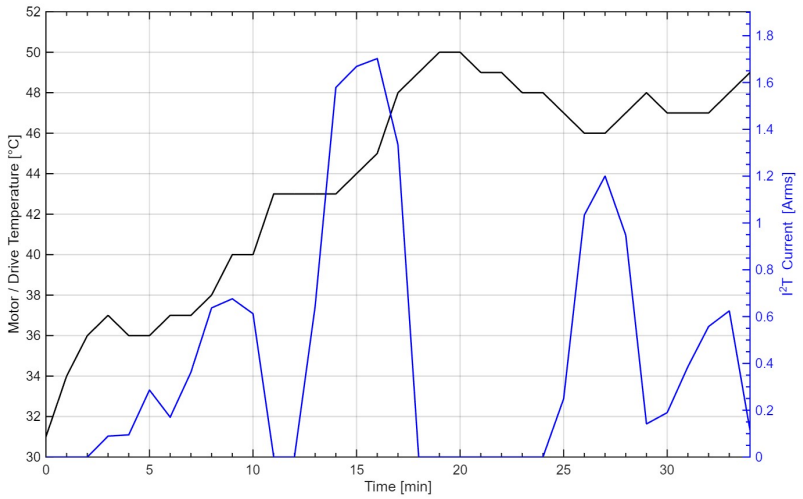


Figure 4.10: Evolution of the motor/drive temperature and I²T current over time during the diagnostic test.

To further investigate the influence of the temperature, additional tests were performed starting from the previously defined operating limits, but with both the coil and drive initially at approximately 25°C and 30°C, respectively. Starting the motor from a lower initial temperature delayed the occurrence of the I²t overload, confirming the influence of the initial thermal state on the available operating time. However, this did not result in a significant improvement in the achievable operating conditions, since the current accumulation eventually reached the protection threshold.

A potential approach to extending the operating capability would be the implementation of an additional cooling system. Cooling the windings would increase the heat dissipation capacity of the actuator, allowing the winding temperature to remain lower for a given current. Since the winding resistance increases with temperature, as described by the temperature-resistance relationship, reducing the winding temperature also reduces the resistance and, consequently, the Joule losses. This could provide additional thermal margin over a long operation period and potentially allow operation at higher current levels, provided that the resulting temperatures remain within the limits specified by the manufacturer. Any modification of the nominal current or I²t protection parameters should therefore be performed only after verifying the resulting thermal conditions and within the limits permitted by the manufacturer.

Two possible cooling solutions could be considered. The first would consist of a forced-convection system, using a fan to increase heat transfer from the actuator to the surrounding air. A more effective, although more complex, alternative would be a liquid-cooling system, such as water cooling, which could provide a higher heat-removal capacity.

It is also important to consider the cumulative nature of the I²t algorithm, as described in Equation 3.6. The current itself does not accumulate; rather, the algorithm accumulates

the excess of the squared current relative to the nominal current over time. Consequently, even if an I^2t fault is not triggered during a given test, continuous operation under the same conditions may progressively increase the I^2t accumulation and eventually lead to an I^2t overload. Therefore, the absence of a fault during a finite test period does not necessarily demonstrate that the corresponding operating condition is suitable for continuous operation. This consideration is particularly relevant when assessing the long-duration performance of the actuator and defining its practical operating limits.

Finally, it should be considered that the test bench conditions do not fully replicate the intended application, in which the actuator will operate in contact with high-temperature steam. The elevated ambient temperature associated with this environment is expected to have an impact on actuator performance, which, given the thermal limitations of the motor, is unlikely to be favourable.

Chapter 5

Conclusions

The experimental investigation demonstrated the technical feasibility of the proposed fully variable spool valve actuation concept for the intake system of the super-heated steam expansion machine. The developed test bench successfully enabled the actuation and control of the spool valves using the NLi120X linear actuator, allowing the influence of operating frequency, stroke amplitude, and moving mass on the actuator performance to be experimentally assessed. The achievable operating envelope was, however, found to be significantly constrained by the thermal limitations of the actuator and by its motion-control architecture, particularly as the required operating frequency, stroke amplitude, and moving mass increased.

The results showed that operating frequency, stroke amplitude, and moving mass are the main parameters governing actuator loading. Higher operating frequencies require greater acceleration of the moving mass and, consequently, higher actuator force, which translates into higher current draw and, in turn, greater thermal loading. Stroke amplitude proved to be one of the most influential parameters affecting the achievable operating speed, since larger strokes demand higher acceleration for a given frequency, while heavier moving-mass configurations were also found to require higher current and to reach lower operating limits. Nonetheless, the effect of stroke amplitude was generally more pronounced than that of moving mass, suggesting that reducing the required stroke may be a more effective strategy for extending the operating range than reducing the moving mass alone.

Based on the experimental results, the highest operating speed reached before the I^2t thermal overload threshold was 475 rpm, obtained for the lower-load configurations and smaller stroke amplitudes. This maximum dropped to 375 rpm for the most demanding configuration tested, with a 30 mm stroke. These results confirm that the actuator's sustainable operating speed depends strongly on the mechanical demand imposed by the selected motion profile, and that the achievable operating range is ultimately limited by its thermal capability.

The position tracking analysis confirmed that, although the actuator was able to reproduce the commanded sinusoidal motion, it exhibited a delay and a loss of synchronization with respect to the ideal reference, particularly at the theoretical valve opening and closing positions. Since the tracking error at these points directly affects the timing of the valve events, this deviation has a direct impact on the intake opening duration (IOD). The cycle-by-cycle analysis further showed that the repeatability of these events is operating-condition dependent: the COV, evaluated over the position error within the interval between the theoretical opening and closing points, was lower under less demanding conditions and increased as the actuator approached its operating limits.

This trend was corroborated by a complementary statistical evaluation of the IOD itself, based directly on the measured valve opening and closing instants rather than on deviation from the ideal sinusoidal reference. The resulting variability followed the same pattern identified in the tracking analysis, increasing under more demanding operating conditions. Taken together, the two analyses indicate that the loss of repeatability in valve timing is an inherent characteristic of the actuator's behaviour near its operating limits, rather than an artefact of the reference trajectory used for comparison, and that even relatively moderate cycle-to-cycle position variations can translate into changes in the opening duration, with a direct effect on the consistency of steam admission. It should be noted that this statistical characterization was based on a limited number of cycles, constrained by the data acquisition software used; a larger sample would allow a more robust characterization of this variability.

The friction analysis provided additional insight into the sources of this variability. The introduction of piston rings was found to increase the mean effective position error, although the magnitude of this effect was condition-dependent and generally less pronounced than that of the actuator's overall dynamic load. This indicates that, while friction at the ring–liner interface contributes to the observed tracking deviations, it acts as a secondary factor relative to the inertial and thermal loading imposed by the operating conditions themselves.

The operating range was found to be limited primarily by the predefined thermal protection algorithm, rather than by the actuator's ability to generate the commanded trajectory. The actuator was not fundamentally constrained by its capacity to follow the required motion profile, but by its ability to sustain the associated current thermally. Notably, the thermal protection limit was reached before a critical motor temperature was necessarily attained, confirming that the protection mechanism responds to accumulated electrical loading rather than to an instantaneous temperature threshold. Additional cooling is therefore identified as the most direct route to extending the sustainable operating range, as it would allow a higher nominal current to be used without compromising the integrity of the windings. It should also be noted that the present test bench does not replicate the elevated ambient temperature associated with the actuator's intended operating environment, in direct contact with superheated steam. Since this elevated temperature is

expected to further constrain the thermal capability of the actuator, the operating limits identified in this work likely represent an optimistic estimate relative to the conditions of the final application.

A further limitation stems from the control system architecture: the resolution of the encoder constrains the precision of the position feedback, and part of the observed deviation from the ideal sinusoidal trajectory cannot be attributed exclusively to the actuator's own performance, since the communication and feedback architecture introduce additional constraints. In particular, the mandatory dwell time imposed by the Modbus communication protocol prevents the actuator from following a continuous trajectory, introducing periodic interruptions in the motion profile that are amplified at higher operating frequencies. An EtherCAT-based implementation would reduce these discretizations and communication-cycle limitations and should therefore be considered in future developments of the control system. Overall, the experimental results demonstrate that the proposed fully variable valve actuation concept is technically feasible, fulfilling the primary objective defined in Section 1.2. However, when assessed against the target operating envelope of the final application, up to 1500 rpm and a 40 mm stroke, the selected NLi120X actuator does not meet the required specifications. The maximum sustainable operating speed identified experimentally, 475 rpm, decreasing to 375 rpm under the most demanding tested configuration, remained substantially below the targeted actuation speed, and the maximum tested stroke of 30 mm remained below the 40 mm stroke targeted for the final application. Therefore, the actuator could not demonstrate the combination of speed and stroke required for the intended operating conditions, and the observed increase in position error with operating speed indicates that, in an eventual application within the complete machine, would introduce significant deviations in admission timing, potentially affecting the consistency of steam admission and, consequently, engine torque and efficiency.

These results indicate that, although the NLi120X is capable of generating and controlling the required type of valve motion, its present thermal capability and control architecture are insufficient to support the targeted operating range. Further development of the actuation system, particularly through improved thermal management and a higher-performance control and communication architecture, would therefore be required before integration into the final expansion machine.

5.1 Future Works

The experimental results obtained in this work identified the main dynamic, thermal and control limitations of the investigated actuator. Future work should therefore focus on determining whether these limitations can be overcome within the requirements of the final expansion machine and, if not, on defining the requirements for an alternative actuation solution. The proposed developments are prioritised according to their relevance to the final system.

5.1.1 Actuator Selection and Requirements for the Final Machine

The first step towards the integration of the valve actuation system into the final expansion machine should be to assess the suitability of the NLi120X for the required operating conditions. The target operating point of the final machine requires a stroke of approximately 40 mm at 1500 rpm. The results obtained in this work indicate that the actuator's operating capability is strongly influenced by stroke, moving mass, velocity and acceleration, while the thermal load imposes an additional limitation on sustained operation.

Consequently, the selection of an actuator for the final machine should not be based solely on its nominal or peak force rating. Instead, the required stroke, peak velocity, peak acceleration, dynamic force, continuous operating capability, thermal capacity, feedback resolution and control bandwidth should be considered simultaneously. The dynamic requirements should first be determined from the required valve motion and moving mass, followed by verification of the actuator's thermal capability for the corresponding duty cycle.

Three development paths can then be considered: further optimization of the NLi120X, modification of the valve mechanism to reduce the required stroke or moving mass, or selection of an alternative actuator capable of satisfying the required dynamic and thermal operating conditions. This assessment should be performed before further extensive validation of the current actuator at high cycle counts.

5.1.2 Thermal Management and Validation

Since the thermal load was identified as a major limitation during the experimental investigation, the potential of an enhanced cooling system should be assessed. Both forced-air and liquid-based cooling solutions could be considered, depending on the thermal requirements and integration constraints of the final machine. The objective should be to quantify the extent to which improved heat dissipation increases the sustainable operating range.

This assessment should be performed under representative operating conditions and should consider not only the instantaneous current demand but also the accumulated thermal load during continuous operation. The results would establish whether thermal management alone can provide a sufficient increase in the operating envelope to justify retaining the NLi120X for the final application.

5.1.3 Control, Communication and Synchronization

The control and communication architecture should be further developed to improve trajectory tracking and synchronization with the targeted sinusoidal motion, as well as synchronization with the working piston. As discussed previously, the Modbus communication method introduces a waiting time between successive tasks (position setpoints),

which contributes to deviations from the desired motion profile. An alternative communication architecture, such as EtherCAT or CANopen, could therefore be investigated to reduce communication-induced delays and improve the temporal resolution of the control loop.

The synchronization of the intake valve with the working piston should subsequently be validated using a representative piston reference. This should account for the temporal resolution of the available hardware and the characteristics of the digital input interface used in the present setup. The influence of the communication architecture and feedback resolution on the achievable valve timing accuracy should be quantified at the target operating frequency.

5.1.4 Long-Duration and Repeatability Validation

Once an actuator configuration capable of meeting the required operating conditions has been identified, long-duration testing should be performed to assess the stability and repeatability of the actuation system. Extending the analysis to a substantially larger number of cycles would provide a stronger statistical basis for evaluating the repeatability of the IOT and IOD, as well as their evolution during prolonged operation.

In addition to tracking performance, long-duration tests should monitor the thermal behaviour of the actuator and possible changes in the measured force, position and velocity profiles. This would provide further information on the suitability of the actuation system for continuous operation.

5.1.5 Mechanical Configuration Optimization

Further optimization of the mechanical configuration could be considered after the actuator requirements have been established. In particular, reducing the moving mass or the required valve stroke could decrease the dynamic force demand and consequently the actuator current and thermal load. The influence of actuator orientation could also be investigated for the final machine configuration, particularly regarding gravity-related effects.

These modifications should be considered as secondary optimization measures, since their relevance depends on the actuator configuration selected for the final system.

References

M. Antonelli, A. Baccioli, M. Francesconi, and L. Martorano. Experimental and Numerical Analysis of the Valve Timing Effects on the Performances of a Small Volumetric Rotary Expansion Device. *Energy Procedia*, 45:1077–1086, 2014. ISSN 18766102. doi: 10.1016/j.egypro.2014.01.113. URL https://linkinghub.elsevier.com/retrieve/pii/S1876610214001143.

M. Badami and M. Mura. Preliminary design and controlling strategies of a small-scale wood waste Rankine Cycle (RC) with a reciprocating steam engine (SE). *Energy*, 34(9): 1315–1324, September 2009. ISSN 03605442. doi: 10.1016/j.energy.2009.04.031. URL https://linkinghub.elsevier.com/retrieve/pii/S0360544209001571.

Max Bolderman, Mircea Lazar, and Hans Butler. Physics–Guided Neural Networks for Inversion–based Feedforward Control applied to Linear Motors. In *2021 IEEE Conference on Control Technology and Applications (CCTA)*, pages 1115–1120, San Diego, CA, USA, August 2021. IEEE. ISBN 978-1-6654-3643-4. doi: 10.1109/CCTA48906.2021.9659174. URL https://ieeexplore.ieee.org/document/9659174/.

Bimal K. Bose. *Modern power electronics and AC drives*. Prentice Hall PTR, Upper Saddle River, NJ, 2002. ISBN 978-0-13-016743-9.

Veysel T. Buyukdegirmenci and Philip T. Krein. Machine characterization for short-term or instantaneous torque capabilities: An approach based on transient thermal response. In *2013 International Electric Machines & Drives Conference*, pages 801–808, Chicago, IL, USA, May 2013. IEEE. ISBN 978-1-4673-4974-1 978-1-4673-4975-8 978-1-4673-4972-7 978-1-4673-4973-4. doi: 10.1109/IEMDC.2013.6556185. URL http://ieeexplore.ieee.org/document/6556185/.

Yu Chen, Yuesen Wang, and Robert Raine. Correlation between cycle-by-cycle variation, burning rate, and knock: A statistical study from PFI and DISI engines. *Fuel*, 206: 210–218, October 2017. ISSN 00162361. doi: 10.1016/j.fuel.2017.06.016. URL https://linkinghub.elsevier.com/retrieve/pii/S001623611730707X.

Clefi Cornetti. *Untersuchung einer vollständig varia blen Steuerung einer Expansionsma schine, (Investigation of a Fully Variable Control System for an Expansion Machine)*. Bachelor, Institut für Kolbenmaschinen, Karlsruher Institut für Technologie (KIT), Karlsruhe, Germany, October 2025.

Georgios D. Demetriades, Hector Zelaya De La Parra, Erik Andersson, and Hakan Olsson. A Real-Time Thermal Model of a Permanent-Magnet Synchronous Motor. *IEEE Transactions on Power Electronics*, 25(2):463–474, February 2010. ISSN 0885-8993, 1941-0107. doi: 10.1109/TPEL.2009.2027905. URL https://ieeexplore.ieee.org/document/5204128/.

Deutsches Institut für Normung. DIN ISO 2768: General tolerances – Part 1: Tolerances for linear and angular dimensions without individual tolerance indications, 1989.

Zlatina Dimitrova, Massinissa Tari, Patrick Lanusse, François Aioun, and Xavier Moreau. Robust control for an electromagnetic actuator for a camless engine,. *Mechatronics*, 57:109–128, February 2019. ISSN 09574158. doi: 10.1016/j.mechatronics.2018.12.004. URL https://linkinghub.elsevier.com/retrieve/pii/S0957415818301909.

DuPont. Teflon® PTFE Fluoropolymer Resin — Properties Handbook. Technical report, E.I. du Pont de Nemours and Company.

Daniel Eirich. Vorbereitende Simulation und Poten tialabschätzung einer Dampfmaschine im Kontext eines solaren Clausius Rankine Prozesses (Preparatory Simulation and Potential Assessment of a Steam Engine in the Context of a Solar Clausius–Rankine Cycle). Master's thesis, Institut für Kolbenmaschinen, Karlsruher Institut für Technologie (KIT), May 2024.

Linus Engelmann, Matthias Ihme, Andreas Kempf, and Benjamin Böhm. A general probabilistic approach for the analysis of cycle-to-cycle variations in internal combustion engines. *Combustion and Flame*, 287:114911, May 2026. ISSN 00102180. doi: 10.1016/j.combustflame.2026.114911. URL https://linkinghub.elsevier.com/retrieve/pii/S0010218026001471.

Ulrich Grigull, Johannes Straub, and Peter Schiebener, editors. *Steam Tables in SI-Units/Wasserdampftafeln*. Springer Berlin Heidelberg, Berlin, Heidelberg, 1984. ISBN 978-3-540-13503-6 978-3-642-96840-2. doi: 10.1007/978-3-642-96840-2. URL http://link.springer.com/10.1007/978-3-642-96840-2.

J. L. Guzmán and T. Hägglund. Tuning rules for feedforward control from measurable disturbances combined with PID control: a review. *International Journal of Control*, 97(1):2–15, January 2024. ISSN 0020-7179, 1366-5820. doi: 10.1080/00207179.2021.1978537. URL https://www.tandfonline.com/doi/full/10.1080/00207179.2021.1978537.

I. Haskara, V. V. Kokotovic, and L. A. Mianzo. Control of an electro-mechanical valve actuator for a camless engine. *International Journal of Robust and Nonlinear Control*, 14(6):561–579, April 2004. ISSN 1049-8923, 1099-1239. doi: 10.1002/rnc.903. URL https://onlinelibrary.wiley.com/doi/10.1002/rnc.903.

Hendrik Heyder. Entwicklung und Applikation einer Steuerungsstrategie für eine Heiß dampfmaschine auf Basis einer simu lativen Sensitivitätsanalyse (Development and Application of a Control Strategy for a Superheated Steam Engine Based on a Simulation-Based Sensitivity Analysis). Master's thesis, Institut für Kolbenmaschinen, Karlsruher Institut für Technologie (KIT), October 2025.

International Maritime Organization. 2023 IMO Strategy on Reduction of GHG Emissions from Ships. Resolution MEPC.377(80), International Maritime Organization, July 2023. URL https://www.imo.org/en/ourwork/environment/pages/2023-imo-strategy-on-reduction-of-ghg-emissions-from-ships.aspx.

International Organization for Standardization. ISO 8015: Geometrical product specifications (GPS) – Fundamentals – Concepts, principles and rules, 2011.

Longxin Jiang, Liang Liu, Xiaowei Peng, and Zhaoping Xu. Design and Analysis of a Fully Variable Valve Actuation System. *Energies*, 13(23):6391, December 2020. ISSN 1996-1073. doi: 10.3390/en13236391. URL https://www.mdpi.com/1996-1073/13/23/6391.

Yoann Jovet, Frédéric Lefèvre, Alexis Laurent, and Marc Clausse. Combined energetic, economic and climate change assessment of heat pumps for industrial waste heat recovery. *Applied Energy*, 313:118854, May 2022. ISSN 03062619. doi: 10.1016/j.apenergy.2022.118854. URL https://linkinghub.elsevier.com/retrieve/pii/S0306261922002902.

Ralph Kennel, Long He, Jinsong Kang, Fengxiang Wang, and Jose Rodriguez. Adaptive Model Predictive Current Control for PMLSM Drive System. *IEEE Transactions on Industrial Electronics*, 70(4):3493–3502, April 2023. ISSN 0278-0046, 1557-9948. doi: 10.1109/TIE.2022.3179550. URL https://ieeexplore.ieee.org/document/9789964/.

Gunnar Latz, Sven Andersson, and Karin Munch. Selecting an Expansion Machine for Vehicle Waste-Heat Recovery Systems Based on the Rankine Cycle. pages 2013–01–0552, Detroit, Michigan, United States, April 2013. doi: 10.4271/2013-01-0552. URL https://saemobilus.sae.org/papers/selecting-expansion-machine-vehicle-waste-heat-recovery-systems-based-rankine-cycle-

Xiangyang Liu, Manh Quang Nguyen, Jianchu Chu, Tian Lan, and Maogang He. A novel waste heat recovery system combing steam Rankine cycle and organic Rankine cycle for marine engine. *Journal of Cleaner Production*, 265:121502, August 2020. ISSN 09596526. doi: 10.1016/j.jclepro.2020.121502. URL https://linkinghub.elsevier.com/retrieve/pii/S0959652620315493.

Mahle GmbH. *Pistons and engine testing*. ATZ/MTZ-Fachbuch. Vieweg+Teubner Verlag, Wiesbaden, 2012. ISBN 978-3-8348-1590-3 978-3-8348-8662-0. doi: 10.1007/978-3-8348-8662-0.

Sooraj Maurya, Shailendra Kumar Shukla, and Saurabh Pathak. A review on waste heat and its utilization through Organic Rankine Cycle systems. *Sādhanā*, 50(3):195, August 2025. ISSN 0973-7677. doi: 10.1007/s12046-025-02891-y. URL https://link.springer.com/10.1007/s12046-025-02891-y.

Paolo Mercorelli and Nils Werner. An Adaptive Resonance Regulator Design for Motion Control of Intake Valves in Camless Engine Systems. *IEEE Transactions on Industrial Electronics*, 64(4):3413–3422, April 2017. ISSN 0278-0046, 1557-9948. doi: 10.1109/TIE.2016.2606091. URL http://ieeexplore.ieee.org/document/7560596/.

MS Motorservice International GmbH. Kolbenringe für Verbrennungsmotoren. Technical information, MS Motorservice International GmbH, 2015. Article No. 50 003 958-01.

Pranay Nagar and Scott Miers. Friction between Piston and Cylinder of an IC Engine: a Review. pages 2011–01–1405, Detroit, Michigan, United States, April 2011. doi: 10.4271/2011-01-1405. URL https://saemobilus.sae.org/papers/friction-piston-cylinder-ic-engine-a-review-2011-01-1405.

NiLAB GmbH. NiLAB Starter User Manual & Technical Documentation. Technical Manual, NiLAB GmbH, 2023. URL https://www.nilab.at/dokuwiki/doku.php?id=start.

Brian A. Paden, Shaun T. Snyder, Brad E. Paden, and Michael R. Ricci. Modeling and Control of an Electromagnetic Variable Valve Actuation System. *IEEE/ASME Transactions on Mechatronics*, 20(6):2654–2665, December 2015. ISSN 1083-4435, 1941-014X. doi: 10.1109/TMECH.2015.2389112. URL http://ieeexplore.ieee.org/document/7038171/.

Sylvain Quoilin, Martijn Van Den Broek, Sébastien Declaye, Pierre Dewallef, and Vincent Lemort. Techno-economic survey of Organic Rankine Cycle (ORC) systems. *Renewable and Sustainable Energy Reviews*, 22:168–186, June 2013. ISSN 13640321. doi: 10.1016/j.rser.2013.01.028. URL https://linkinghub.elsevier.com/retrieve/pii/S1364032113000592.

Florian Raab, Lennart Böse, Harald Klein, and Frank Opferkuch. Steam Storage Rankine Cycle for Unutilized Applications in Distributed High-Temperature Waste Heat Recovery. *Energies*, 17(4):920, February 2024. ISSN 1996-1073. doi: 10.3390/en17040920. URL https://www.mdpi.com/1996-1073/17/4/920.

Michael M. Schechter and Michael B. Levin. Camless Engine. page 960581, Detroit, Michigan, United States, February 1996. doi: 10.4271/960581. URL https://saemobilus.sae.org/papers/camless-engine-960581.

I. Sherrington. Measurement techniques for piston-ring tribology. In *Tribology and Dynamics of Engine and Powertrain*, pages 387–425. Elsevier, 2010. ISBN 978-1-84569-361-9. doi: 10.1533/9781845699932.2.387. URL https://linkinghub.elsevier.com/retrieve/pii/B9781845693619500119.

Gequn Shu, Youcai Liang, Haiqiao Wei, Hua Tian, Jian Zhao, and Lina Liu. A review of waste heat recovery on two-stroke IC engine aboard ships. *Renewable and Sustainable Energy Reviews*, 19:385–401, March 2013. ISSN 13640321. doi: 10.1016/j.rser.2012.11.034. URL https://linkinghub.elsevier.com/retrieve/pii/S1364032112006466.

Sebastian Siedler. *Konzeptentwicklung einer innovati ven, prototypischen Dampfexpansi onsmaschine für den Betrieb eines Clausius-Rankine-Kreisprozesses (Conceptual Development of an Innovative Prototype Steam Expansion Engine for Operation in a Clausius–Rankine Cycle)*. Bachelor, Institut für Kolbenmaschinen, Karlsruher Institut für Technologie (KIT), Karlsruhe, Germany, November 2024.

Dhananjay Kumar Srivastava, Abhimanyu Das, and Nitish Kumar Singh. Variable Valve Actuation Systems. In Dhananjay Kumar Srivastava, Avinash Kumar Agarwal, Amitava Datta, and Rakesh Kumar Maurya, editors, *Advances in Internal Combustion Engine Research*, pages 63–91. Springer Singapore, Singapore, 2018. ISBN 978-981-10-7574-2 978-981-10-7575-9. doi: 10.1007/978-981-10-7575-9_4. URL http://link.springer.com/10.1007/978-981-10-7575-9_4. Series Title: Energy, Environment, and Sustainability.

Mingyi Wang, Rui Yang, Chengming Zhang, Jiwei Cao, and Liyi Li. Inner Loop Design for PMLSM Drives With Thrust Ripple Compensation and High-Performance Current Control. *IEEE Transactions on Industrial Electronics*, 65(12):9905–9915, December 2018. ISSN 0278-0046, 1557-9948. doi: 10.1109/TIE.2018.2814014. URL https://ieeexplore.ieee.org/document/8310569/.

Sebastian Wendel, Armin Dietz, and Ralph Kennel. Model Predictive Position Control for Permanent Magnet Synchronous Linear Motors. In *Innovative Small Drives and Micro-Motor Systems*, 11th GMM/ETG-Symposium. 2017.

Christoph Wieland, Christopher Schifflechner, Fabian Dawo, and Marco Astolfi. The organic Rankine cycle power systems market: Recent developments and future perspectives. *Applied Thermal Engineering*, 224:119980, April 2023. ISSN 13594311. doi: 10.1016/j.applthermaleng.2023.119980. URL https://linkinghub.elsevier.com/retrieve/pii/S1359431123000091.

Jorrit Wronski, Muhammad Imran, Morten Juel Skovrup, and Fredrik Haglind. Experimental and numerical analysis of a reciprocating piston expander with variable valve timing for small-scale organic Rankine cycle power systems. *Applied Energy*, 247: 403–416, August 2019. ISSN 03062619. doi: 10.1016/j.apenergy.2019.04.028. URL https://linkinghub.elsevier.com/retrieve/pii/S0306261919306592.

Hiroshi Yamagata. The Piston Ring. In *The science and technology of materials in automotive engines*, Woodhead Publishing in materials. Woodhead Publishing and Maney Publishing on behalf of The Institute of Materials, Minerals & Mining, Cambridge, 2005. ISBN 978-1-85573-742-6 978-1-84569-085-4 978-0-8493-2585-4.

Hao Yuan, Ximei Zhao, and Dongxue Fu. A novel high-precision motion control for permanent magnet linear synchronous motor servo system. *International Journal of Applied Electromagnetics and Mechanics*, 66(1):181–201, May 2021. ISSN 13835416, 18758800. doi: 10.3233/JAE-201558. URL https://journals.sagepub.com/doi/full/10.3233/JAE-201558.

Appendix A

Attachments - State of the Art

A.1 Thermodynamical Fundamentals

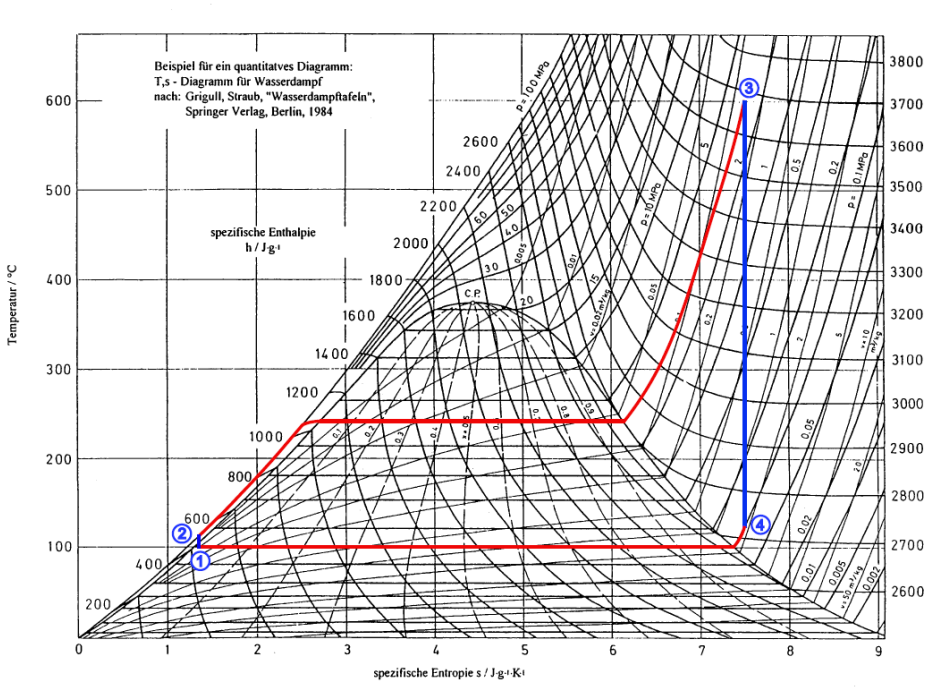


Figure A.1: Ideal TS-Diagram of water for an ideal Clausius-Rankine Cycle at 600 °C and 30 bar Grigull et al. (1984).

A.2 NLi120X Datasheet

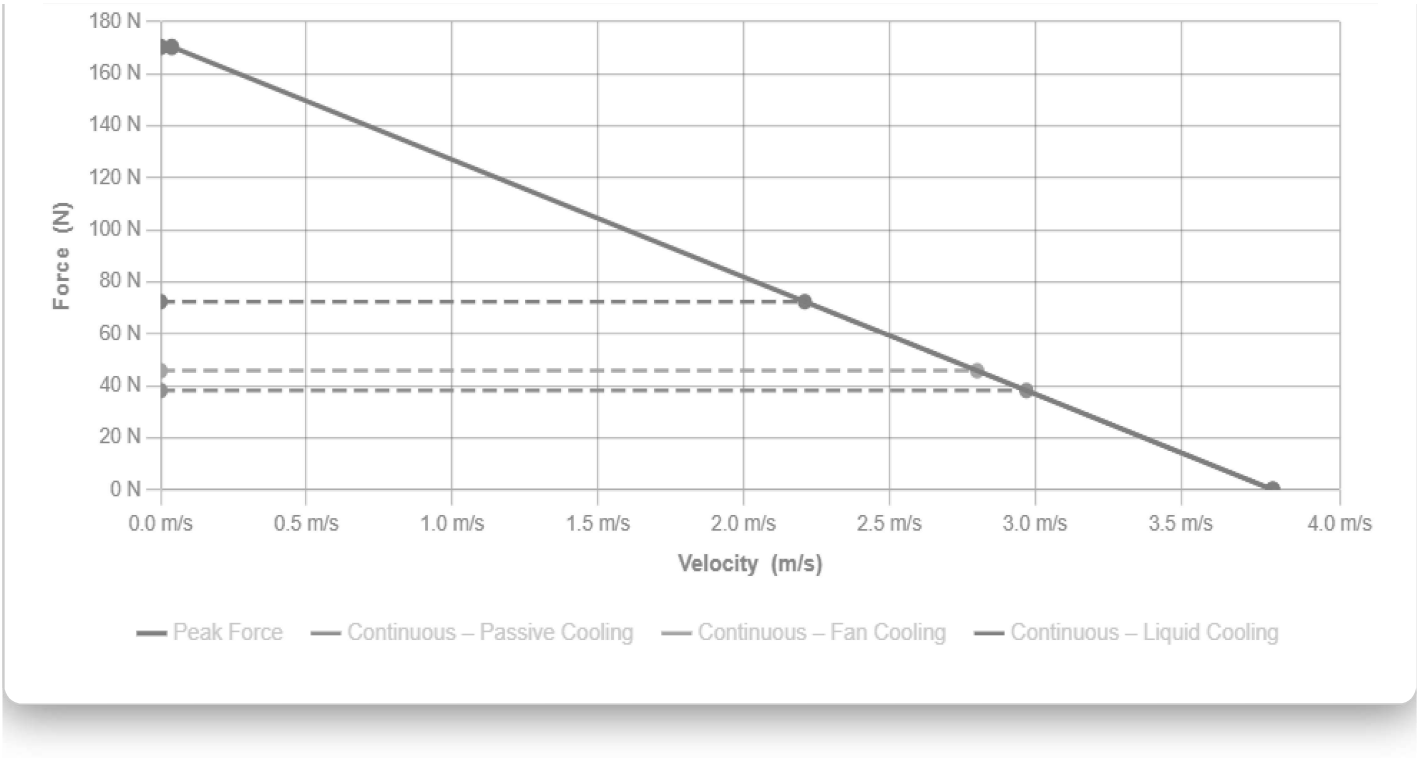
NL120X — Motor Datasheet

DATASHEET PARAMETERS

GENERAL		
Motor Name		**NL120X**
Motor Type		**Green Drive Miniatur Tubular linear motor**
MECHANICAL PERFORMANCE		
Peak Force (S3 – 5% Duty)	N	**170.31**
Continuous Stall Force (passive cooling)	N	**38.1**
Max Velocity (motor current = 0)	m/s	**3.82**
Continuous Stall Force (heatsink plate)	N	**40.01**
Continuous Stall Force (fan cooling)	N	**45.72**
Continuous Stall Force (liquid cooling)	N	**72.39**
ELECTRICAL SPECIFICATION		
Servo Drive Power Supply	Vdc	**24.00**
Required DC-Link Voltage	Vdc	**42.38**
Peak Current (S3 – 5% Duty)	Apk	**14.751**
Continuous Stall Current (passive cooling)	Arms	**3.3**
Continuous Stall Current (heatsink plate)	Arms	**3.465**
Continuous Stall Current (fan cooling)	Arms	**3.96**
Continuous Stall Current (liquid cooling)	Arms	**6.27**
Force Constant	N/Arms	**10.895**
Back EMF Constant (ph-ph)	Vpk/(m/s)	**8.90**
Back EMF Constant (ph-ph)	Vrms/(m/s)	**6.29**
Resistance @ 25°C (ph-ph)	O	**2.98**
Resistance @ 135°C (ph-ph)	O	**4.268**
Inductance (ph-ph)	mH	**1.51**

Electrical Time Constant	ms	0.51
Motor Constant	N/√W	4.56
THERMAL SPECIFICATION IC40		
Max Winding Temperature	°C	135
Max Duration Peak Current	s	1
Max Power Dissipation	W	69.72
Thermal Resistance (case–ambient)	°C/W	1.6
Thermal Resistance (winding–ambient)	°C/W	2.3
Thermal Time Constant	s	1200
MECHANICAL SPECIFICATION		
Stator Length	mm	305
Stator Width	mm	35 x 63
Stator Mass	kg	1.5
Slider Diameter	mm	12
Slider Mass	kg/m	0.78
Magnetic Period (pole pitch N–N)	mm	60
ENCODER SPECIFICATION		
Encoder Type		SIN/COS 1Vpp or Digital AB TTL/BiSS
Encoder Power Supply	Vdc	5 VDC ±10%
Resolution		1 sine period per pole pitch

NL120X — FORCE VS VELOCITY GRAPH @ 24 VDC Bus Level

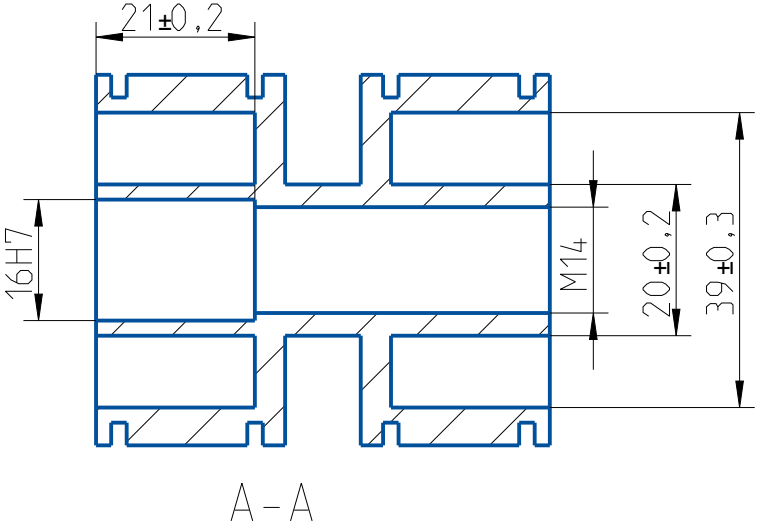

180 N
160 N
140 N
120 N
100 N
80 N
60 N
40 N
20 N
0 N
Force (N)
0.0 m/s
0.5 m/s
1.0 m/s
1.5 m/s
2.0 m/s
2.5 m/s
3.0 m/s
3.5 m/s
4.0 m/s
Velocity (m/s)
Peak Force
Continuous – Passive Cooling
Continuous – Fan Cooling
Continuous – Liquid Cooling

Appendix B

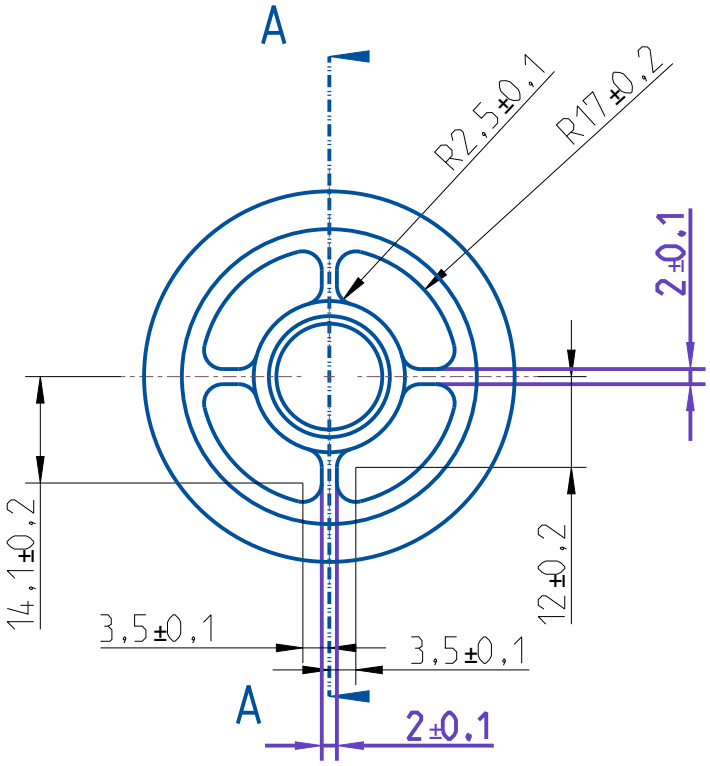
Attachments - Methodology

B.1 Technical Drawings

This section presents the technical drawings of the components manufactured for the test bench. As described in the previous sections, all components were manufactured in the workshops of the Institut für Kolbenmaschinen (IFKM).



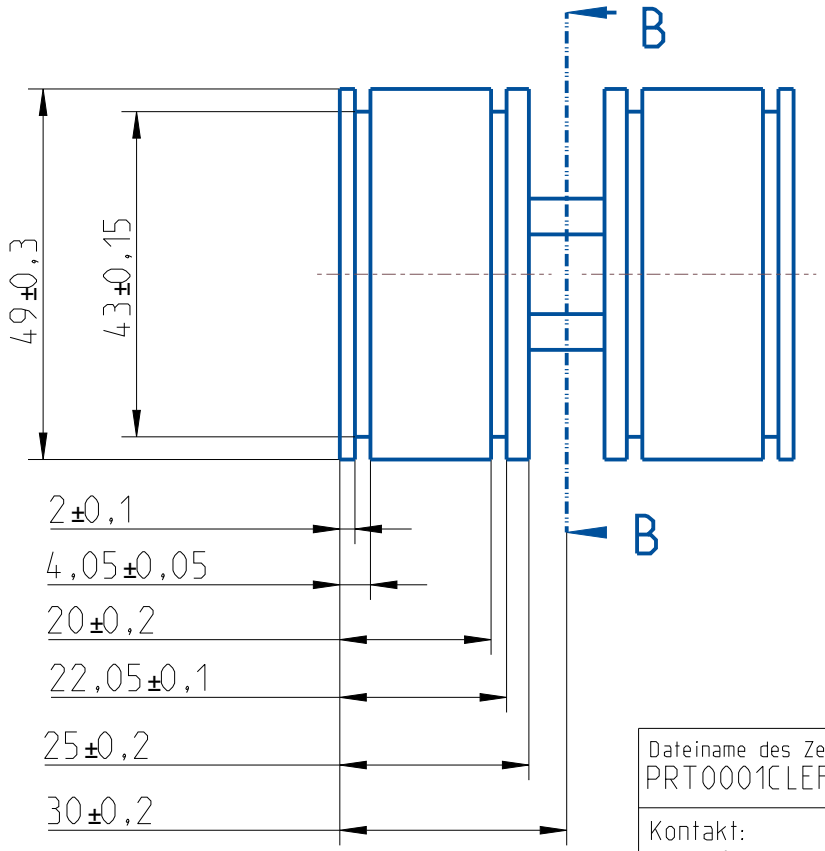
A – A

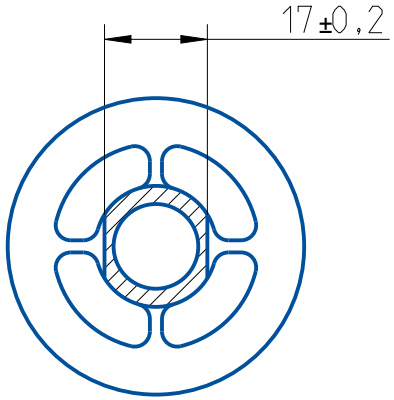




7:10

Dateiname des Zeichnungsobjektes: PRT0001CLEFI			Dateityp: PART	Dateiname der Zeichnung: DRW0001CLEFI	Format: A4
Kontakt: Malki Tel: 00		Tolerierung ISO 8015 Allg. Toleranz DIN ISO 2768 m-K	Oberflaeche DIN ISO 1302 Werkst.-Kanten DIN ISO 13715	Maßstab 1:1	Gew.: 80kg
				Werkstoff: aluminium Halbzeug: 00	
Projektnummer	HeDaMa		Datum	Name	Benennung: Kolben
Stückzahl	2x	Bear.	May-07-26	Catarina Brites	
		Tel:		+351914323429	
		Norm			
		IFKM			Zeichnungsnummer: 20260507_CB_01
					Blatt 1 / 2 Bl.
Zust. Änderung	Datum Nam.	(Urspr.)		(Ers.f.:)	(Ers.d.:)



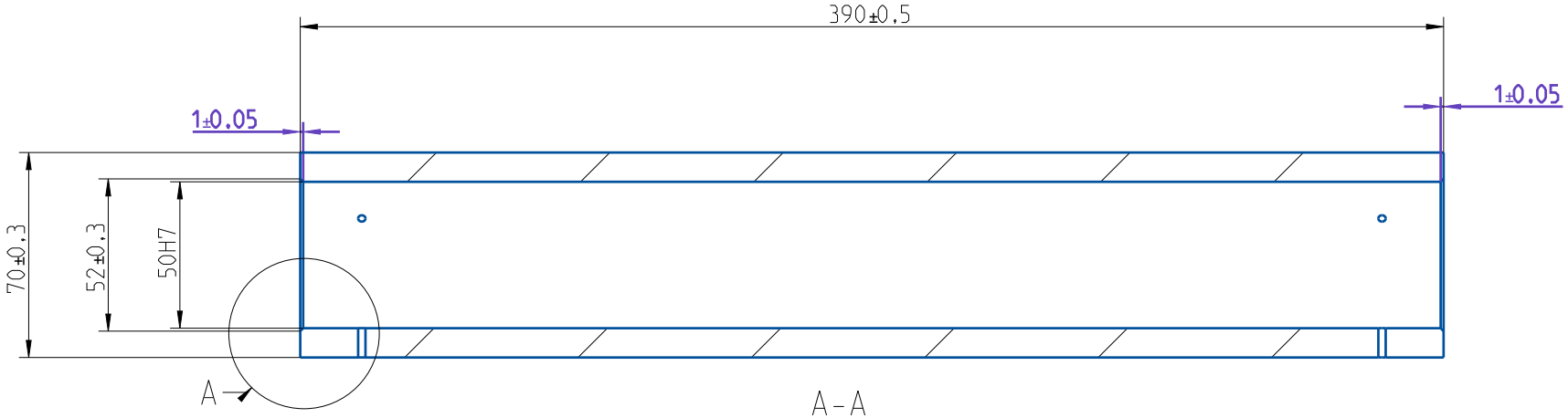


B–B
4:5

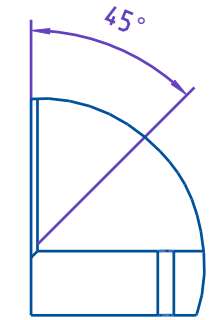


7:10

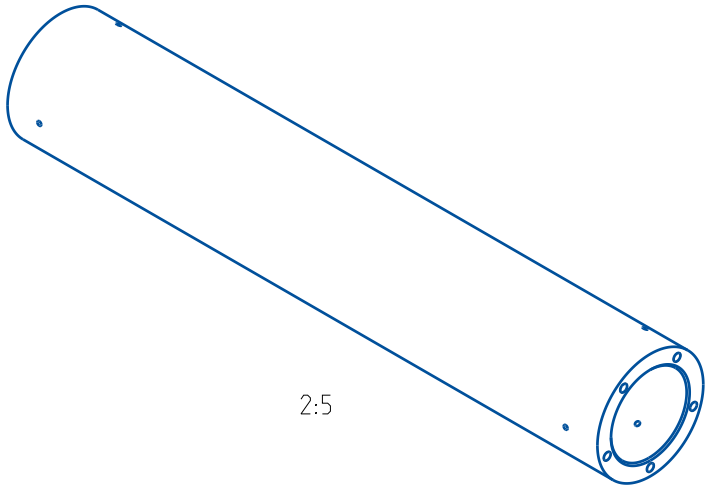
Dateiname des Zeichnungsobjektes: PRT0001CLEFI			Dateityp: PART	Dateiname der Zeichnung: DRW0001CLEFI	Format: A4
Kontakt: Malki Tel: 00		Tolerierung ISO 8015 Allg. Toleranz DIN ISO 2768 m-K	Oberflaeche DIN ISO 1302 Werkst.-Kanten DIN ISO 13715	Maßstab 1:1	Gew.: 80kg
				Werkstoff: aluminium Halbzeug: 00	
Projektnummer	HeDaMa		Datum	Name	Benennung: Kolben
Stückzahl	2x	Bear.	May-07-26	Catarina Brites	
		Gepr.			
		Norm			
		IFKM		Zeichnungsnummer: 20260507_CB_01	Blatt 2 / 2 Bl.
Zust. Änderung	Datum Nam.	(Urspr.)		(Ers.f.:)	(Ers.d.:)



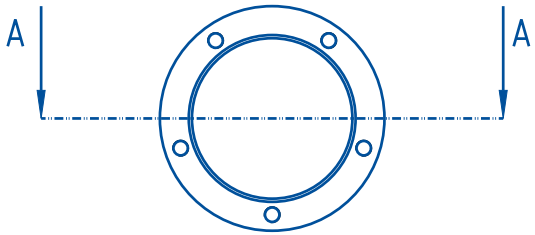
A–A
3:5



Detail A
6:5



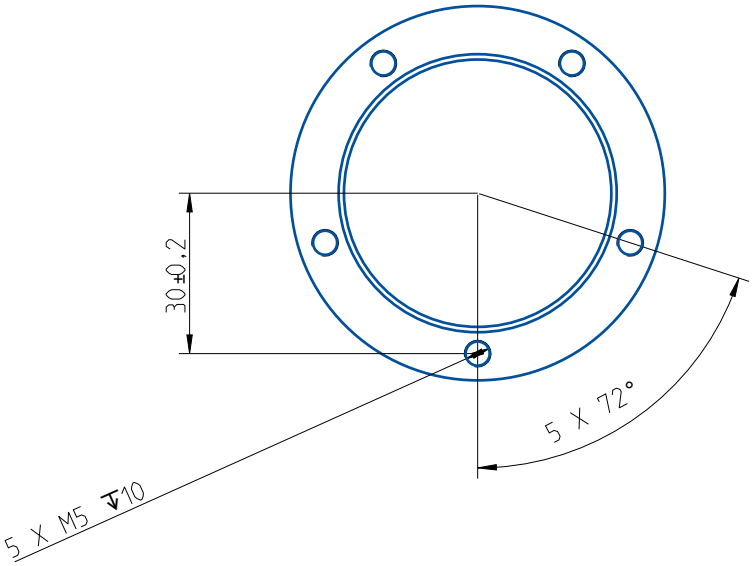
2:5

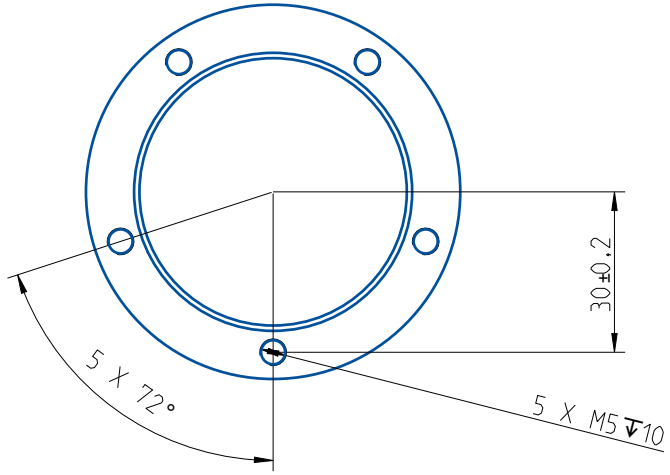


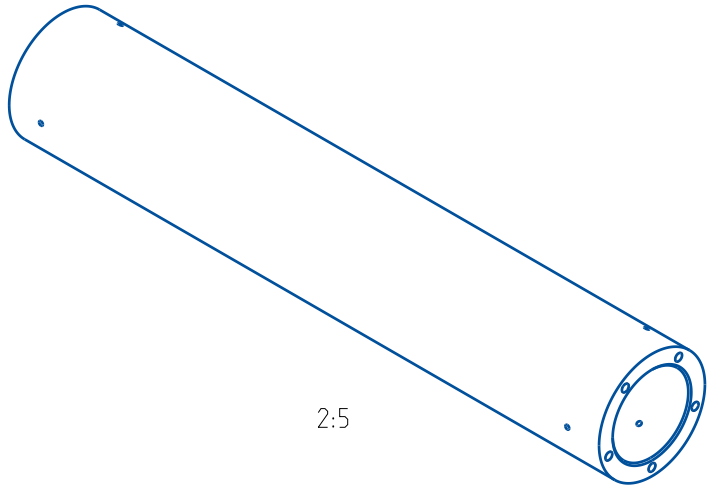
3:5

Dateiname des Zeichnungsobjektes: PRT0002			Dateityp: PART	Dateiname der Zeichnung: Gehäuse	Format: A4
Kontakt: Malki Tel: 00		Tolerierung ISO 8015 Allg. Toleranz DIN ISO 2768 m-K	Oberflaeche DIN ISO 1302 Werkst-Kanten DIN ISO 13715	Maßstab 3:5	Gew.: 200g kg
				Werkstoff: aluminium	
				Halbzeug: 00	
Projektnummer	HeDaMa		Datum	Name	Benennung: Gehäuse
Stückzahl	1	Bear.	Mar-12-26	Catarina Brites	
		Gepr.			
		Norm			
		IFKM			Zeichnungsnummer: 20260313_CB_01
Zust. Änderung	Datum	Nam. (Urspr.)		(Ers.f.:)	(Ers.d.:)

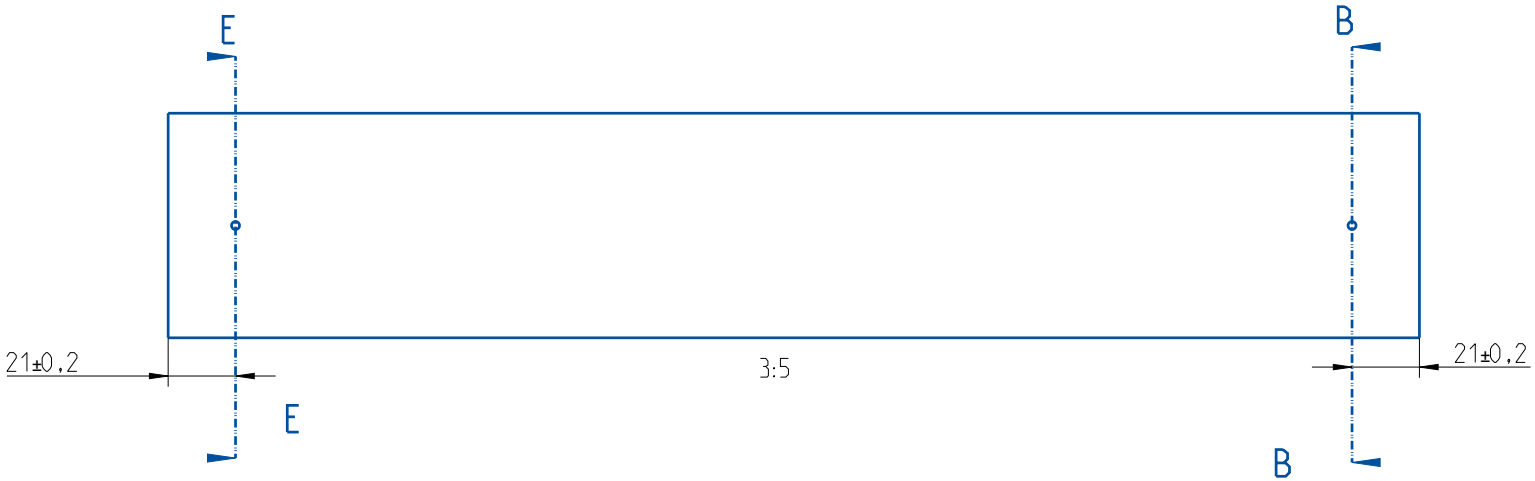
Blatt 1
3 Bl.

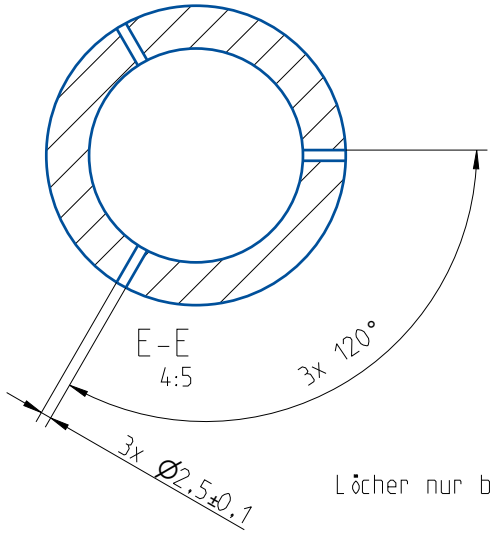




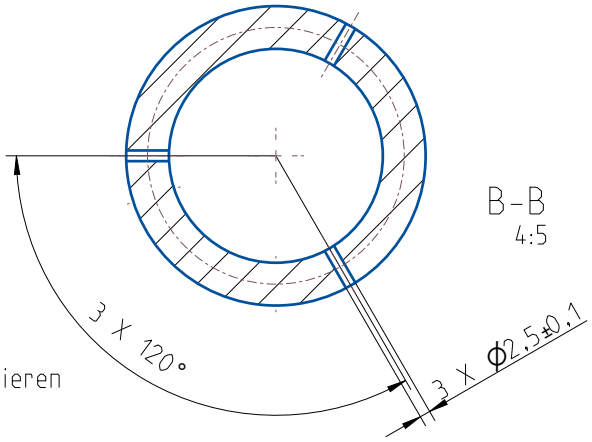


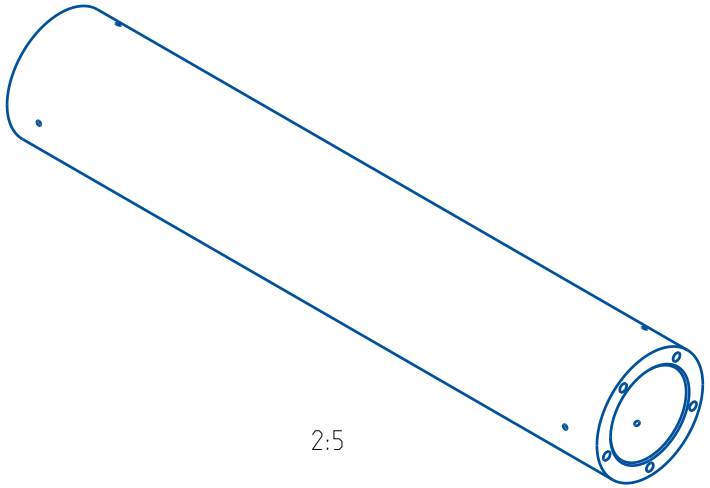
Dateiname des Zeichnungsobjektes: PRT0002			Dateityp: PART	Dateiname der Zeichnung: Gehäuse	Format: A4
Kontakt: Malki Tel: 00		Tolerierung ISO 8015 Allg. Toleranz DIN ISO 2768 m-K	Oberflaeche DIN ISO 1302 Werkst.-Kanten DIN ISO 13715	Maßstab 1:1	Gew.: 200g kg
				Werkstoff: aluminium Halbzeug: 00	
Projektnummer	HeDaMa		Datum	Name	Benennung: Gehäuse
Stückzahl	1	Bear.	Mar-13-26	Catarina Brites	
		Gepr.			
		Norm			
		IFKM		Zeichnungsnummer: 20260313_CB_01	Blatt 2 / 3 Bl.
Zust. Änderung	Datum	Nam. (Urspr.)		(Ers.f.:)	(Ers.d.:)





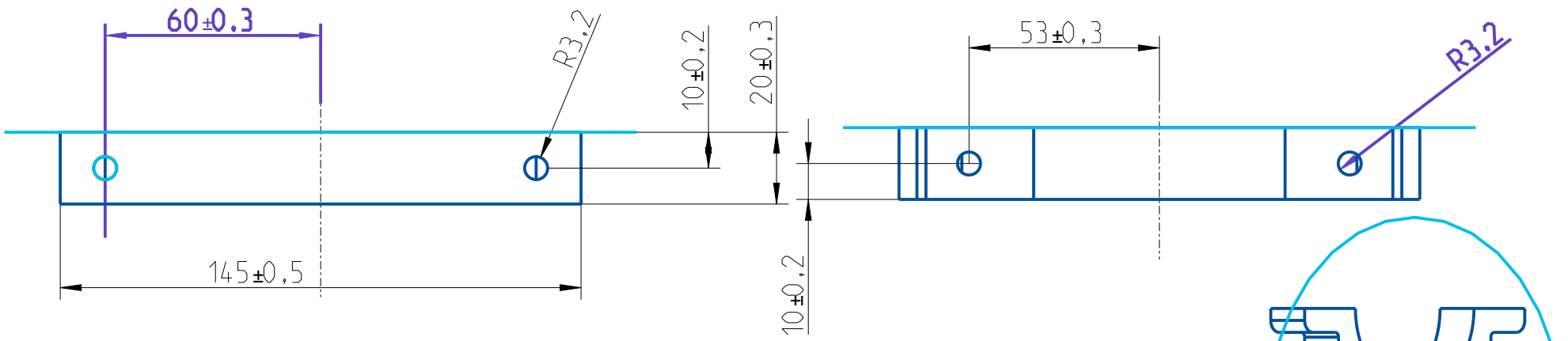
Löcher nur beim Montieren

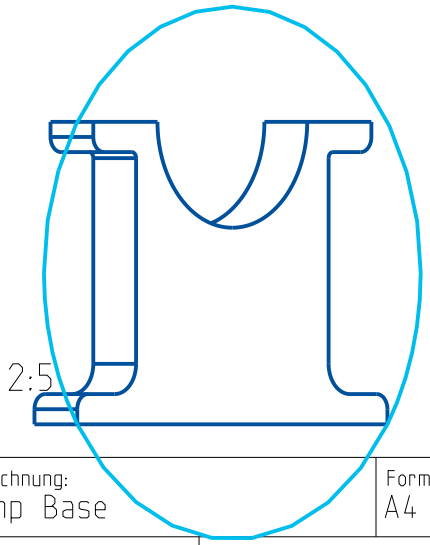




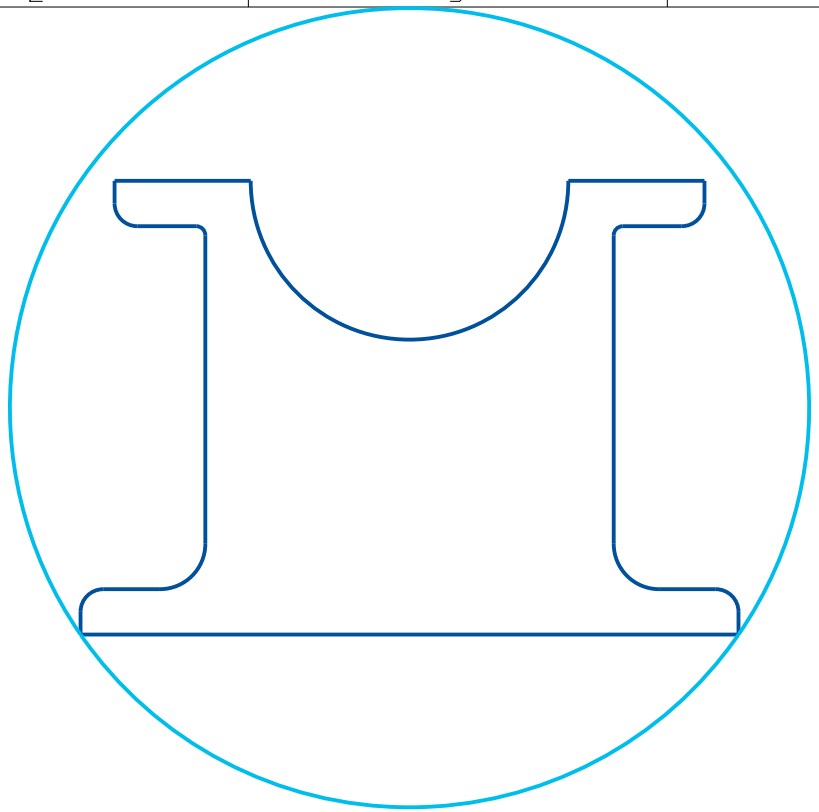
Dateiname des Zeichnungsobjektes: PRT0002			Dateityp: PART	Dateiname der Zeichnung: Gehäuse	Format: A4
Kontakt: Malki Tel: 00		Tolerierung ISO 8015 Allg. Toleranz DIN ISO 2768 m-K	Oberflaeche DIN ISO 1302 Werkst-Kanten DIN ISO 13715	Maßstab 1:1	Gew.: 200g kg
				Werkstoff: aluminium	
				Halbzeug: 00	
Projektnummer	HeDaMa		Datum	Name	Benennung: Gehäuse
Stückzahl	1	Bear.	Mar-13-26	Catarina Brites	
		Gepr.			
		Norm			
		IFKM			Zeichnungsnummer: 20260313_CB_01
Zust. Änderung	Datum	Nam. (Urspr.)		(Ers.f.:)	(Ers.d.:)

Blatt 3
3 Bl.

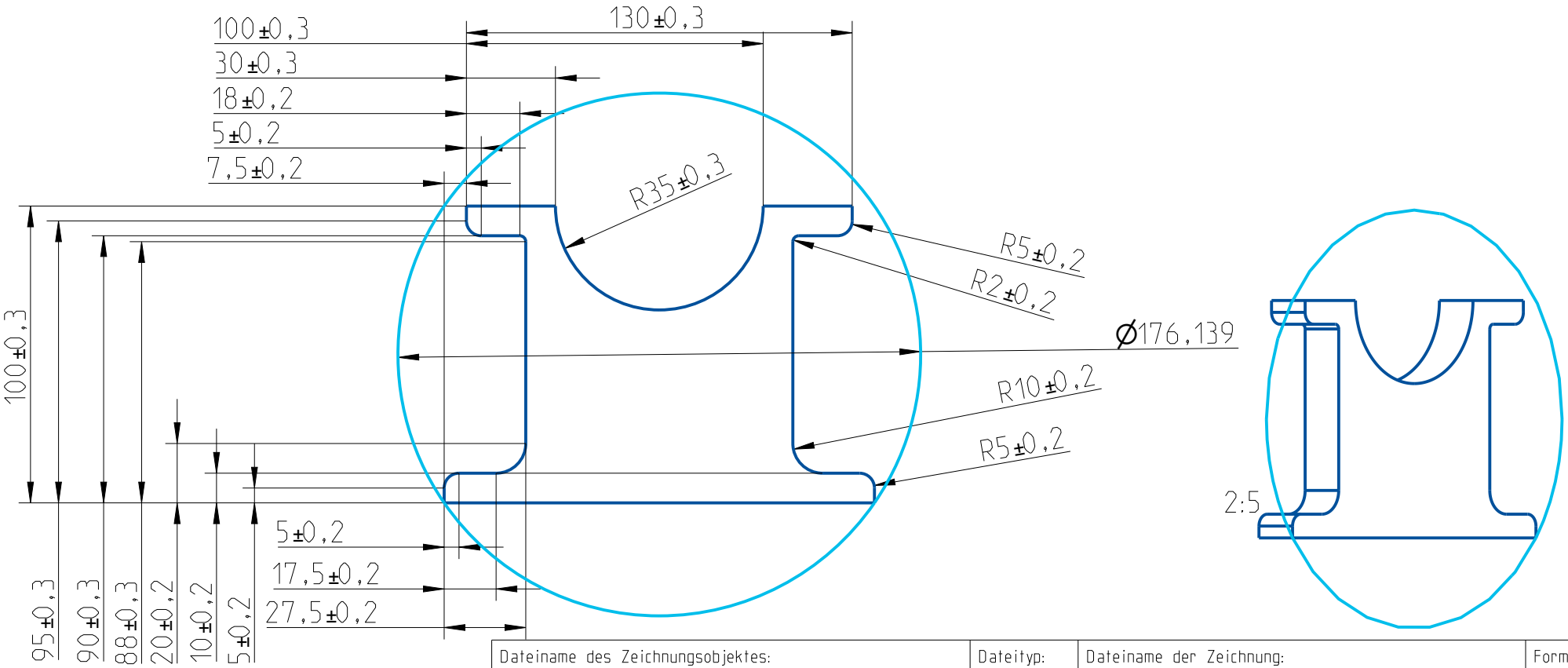




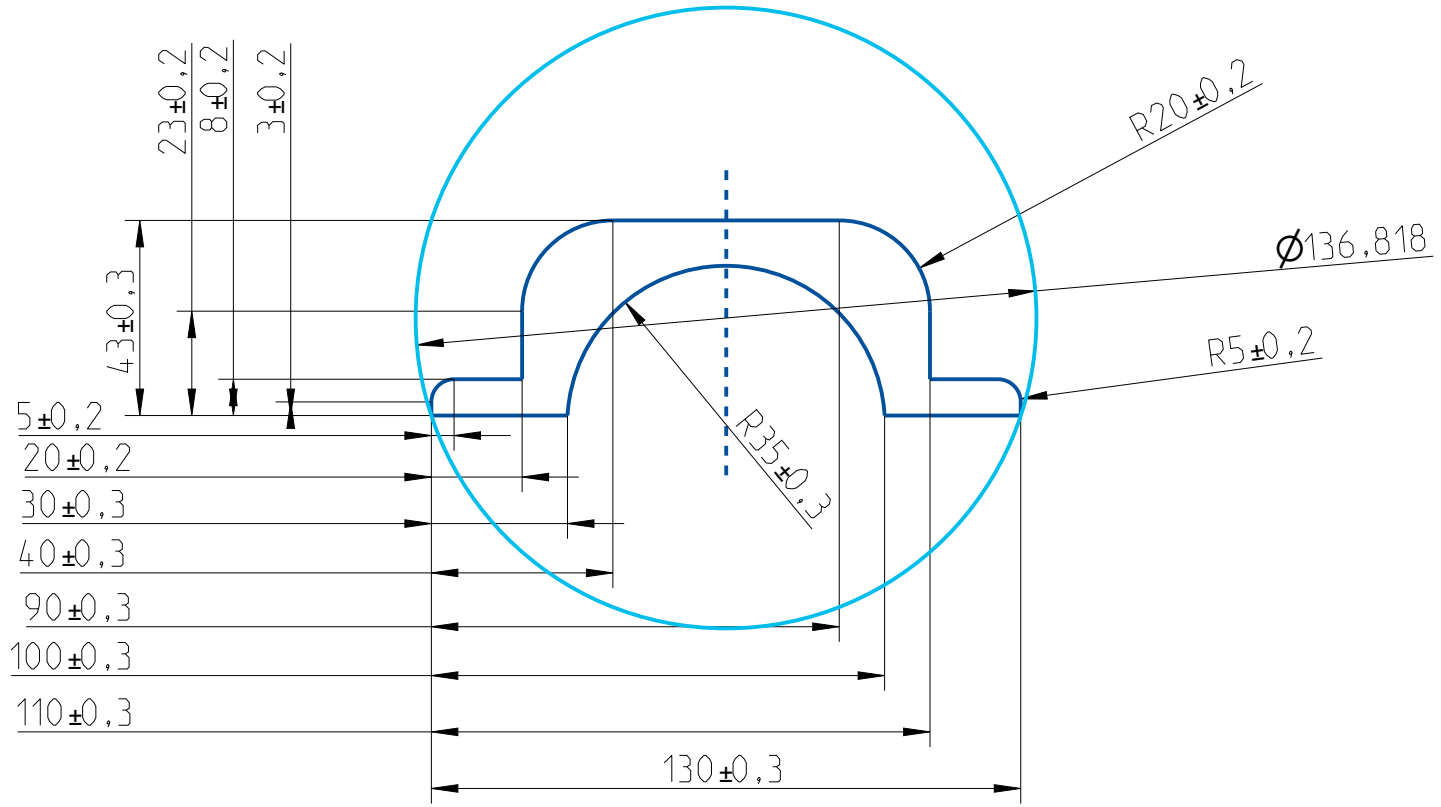
Dateiname des Zeichnungsobjektes: PRT0005			Dateityp: PART	Dateiname der Zeichnung: Housing Clamp Base / Format: A4
Kontakt: Malki Tel: 00		Tolerierung ISO 8015 Allg. Toleranz DIN ISO 2768 m-K	Oberflaeche DIN ISO 1302 Werkst.-Kanten DIN ISO 13715	Maßstab 3:5 / Gew.: 200g kg
				Werkstoff: AlCuMgPb
				Halbzeug: 00
Projektnummer	HeDaMa		Datum	Name
Stückzahl	2	Bear.	Mar-11-26	Catarina Brites
		Gepr.		
		Norm		
		IFKM		Benennung: Housing Clamp Base
				Zeichnungsnummer: 20260311_CB_04 / Blatt 1 / 3 Bl.
Zust. Änderung	Datum Nam.	(Urspr.)	(Ers.f.:)	(Ers.d.:)

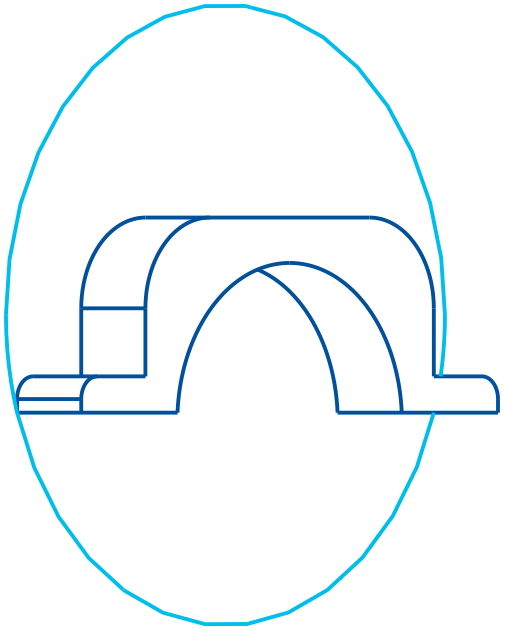


Dateiname des Zeichnungsobjektes: PRT0005			Dateityp: PART	Dateiname der Zeichnung: Housing Clamp Base	Format: A4
Kontakt: Malki Tel: 00		Tolerierung ISO 8015 Allg. Toleranz DIN ISO 2768 m-K	Oberflaeche DIN ISO 1302 Werkst.-Kanten DIN ISO 13715	Maßstab 3:5	Gew.: 200g kg
				Werkstoff: aluminium Halbzeug: 00	
Projektnummer	HeDaMa		Datum	Name	Benennung: Housing Clamp Base
Stückzahl	2	Bear.	Mar-11-26	Catarina Brites	
		Gepr.			
		Norm			
		IFKM		Zeichnungsnummer: 20260311_CB_04	Blatt 2 / 3 Bl.
Zust. Änderung	Datum Nam.	(Urspr.)		(Ers.f.:)	(Ers.d.:)



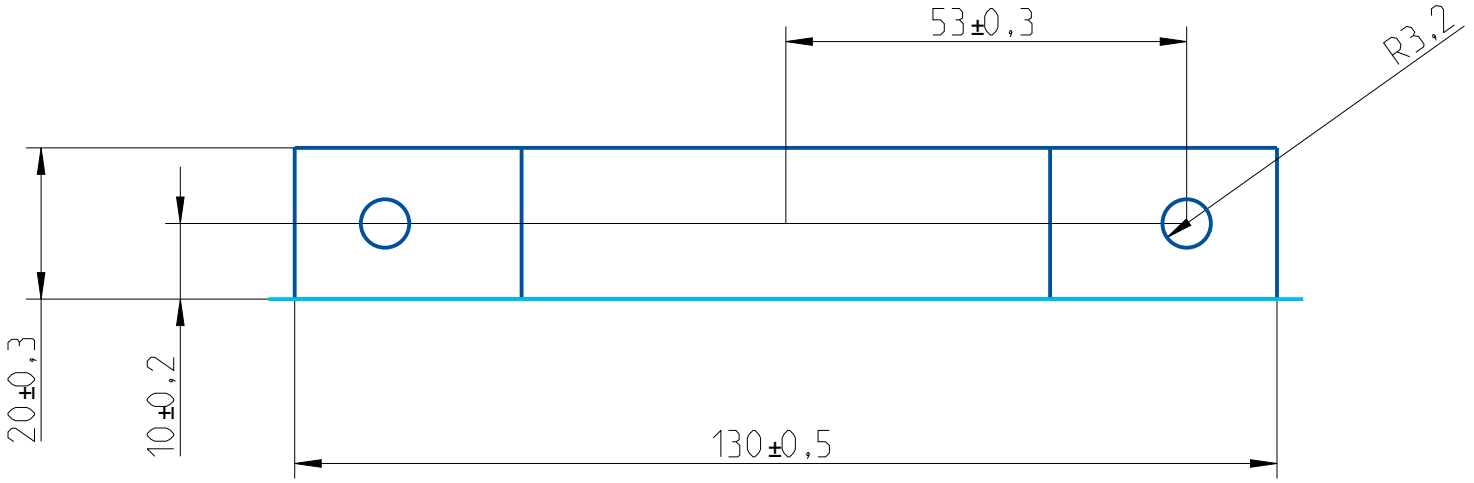
Dateiname des Zeichnungsobjektes: PRT0005		Dateityp: PART	Dateiname der Zeichnung: Housing Clamp Base	Format: A4
Kontakt: Malki Tel: 00	Tolerierung ISO 8015 Allg. Toleranz DIN ISO 2768 m-K	Oberflaeche DIN ISO 1302 Werkst.-Kanten DIN ISO 13715	Maßstab 1:2	Gew.: 200g kg
			Werkstoff: AlCuMgPb Halbzeug: 00	
Projektnummer: HeDaMa		Datum: Mar-11-26	Name: Catarina Brites	Benennung: Housing Clamp Base
Stückzahl: 2		Bear.		
		Gepr.		
		Norm		
IFKM				Zeichnungsnummer: 20260311_CB_04
				Blatt 3 3 Bl.
Zust. Änderung	Datum Nam.	(Urspr.)	(Ers.f.:)	(Ers.d.:)

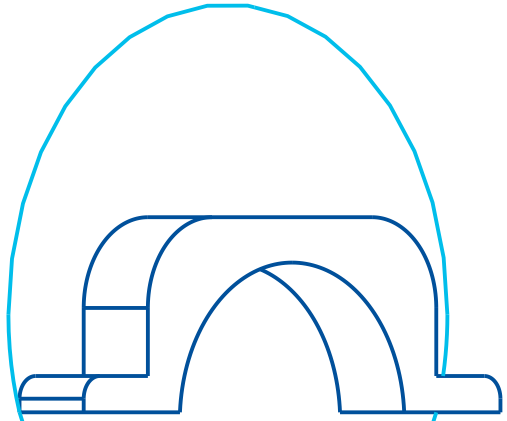




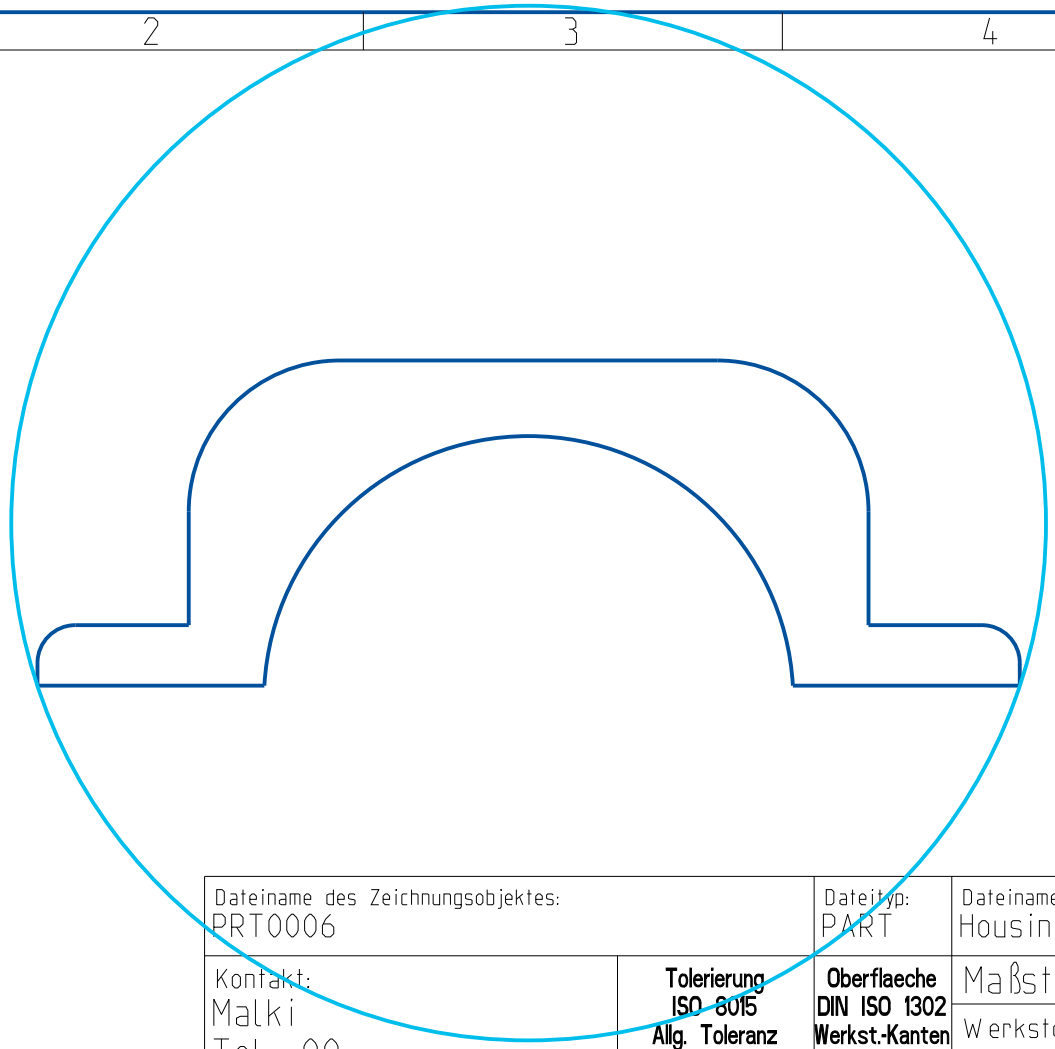
3:5

Dateiname des Zeichnungsobjektes: PRT0006			Dateityp: PART	Dateiname der Zeichnung: Housing Clamp Top	Format: A4
Kontakt: Malki Tel: 00		Tolerierung ISO 8015 Allg. Toleranz DIN ISO 2768 m-K	Oberflaeche DIN ISO 1302 Werkst.-Kanten DIN ISO 13715	Maßstab 3:5	Gew. 150gkg
				Werkstoff: AlCuMgPb Halbzeug: 00	
Projektnummer	HeDaMa		Datum	Name	Benennung: Housing Clamp Top
Stückzahl	2	Bear.	Mar-09-26	Catarina Brites	
		Gepr.			
		Norm			
		IFKM			Zeichnungsnummer: 20260309_CB_02
					Blatt 1 3 Bl.
Zust. Änderung	Datum Nam.	(Urspr.)		(Ers.f.:)	(Ers.d.:)

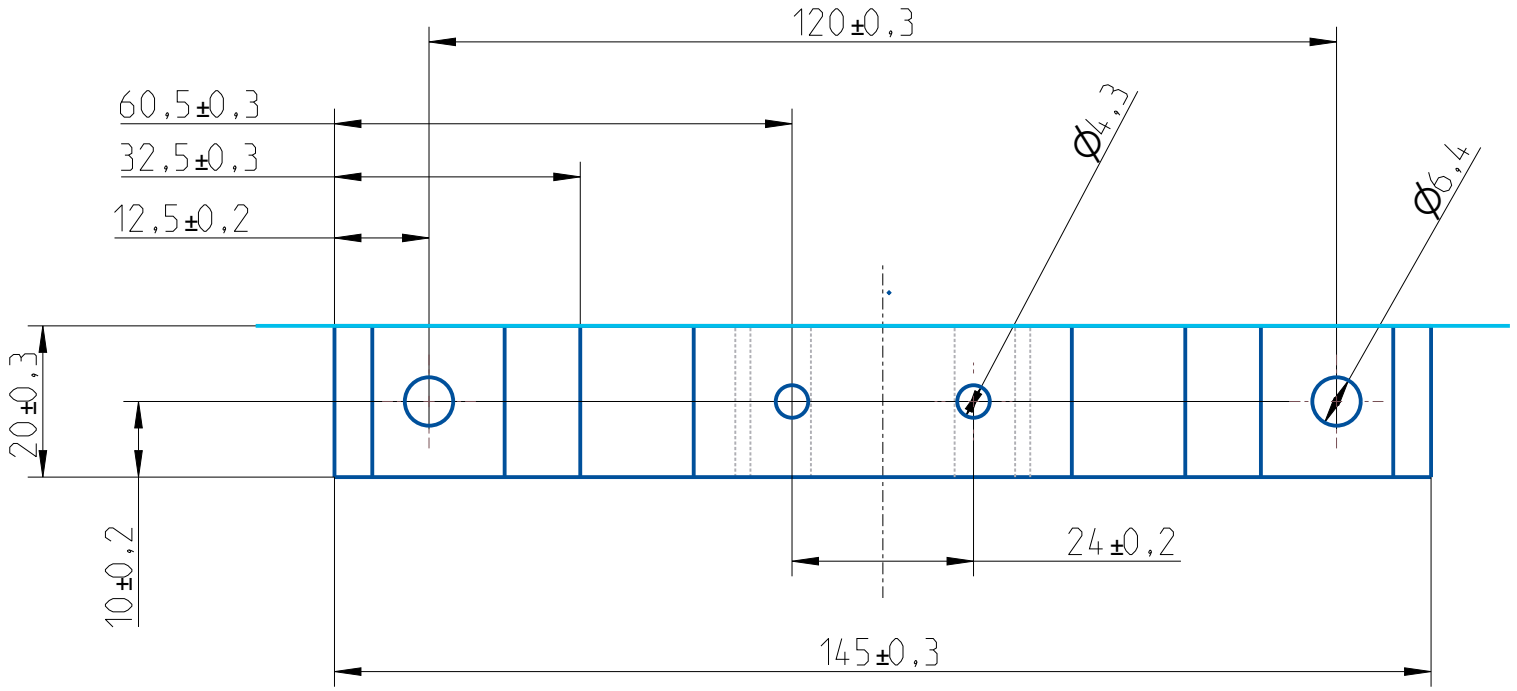


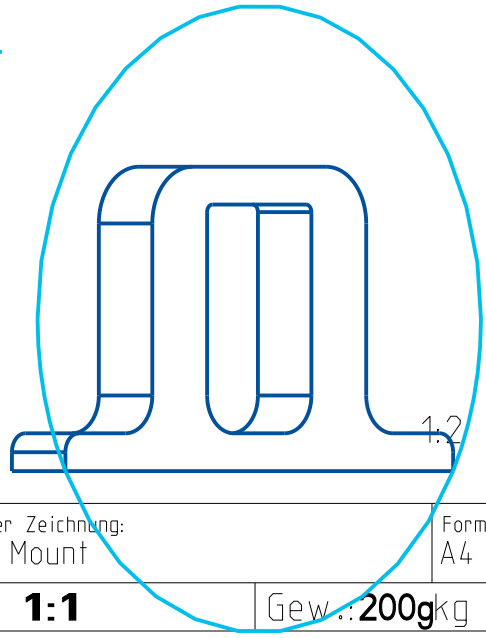


Dateiname des Zeichnungsobjektes: PRT0006			Dateityp: PART	Dateiname der Zeichnung: Housing Clamp Top	Format: A4
Kontakt: Mallki Tel: 00		Tolerierung ISO 8015 Allg. Toleranz DIN ISO 2768 m-K	Oberflaeche DIN ISO 1302 Werkst.-Kanten DIN ISO 13715	Maßstab 1:1	Gew.: 150g kg
				Werkstoff: AlCuMgPb	
				Halbzeug: 00	3:5
Projektnummer	HeDaMa		Datum	Name	Benennung: Housing Clamp Top
Stückzahl	2	Bear.	Mar-11-26	Catarina Brites	
		Gepr.			
		Norm			
		IFKM			Zeichnungsnummer: 20260309_CB_02
					Blatt 2 / 3 Bl.
Zust. Änderung	Datum Nam.	(Urspr.)		(Ers.f.:)	(Ers.d.:)

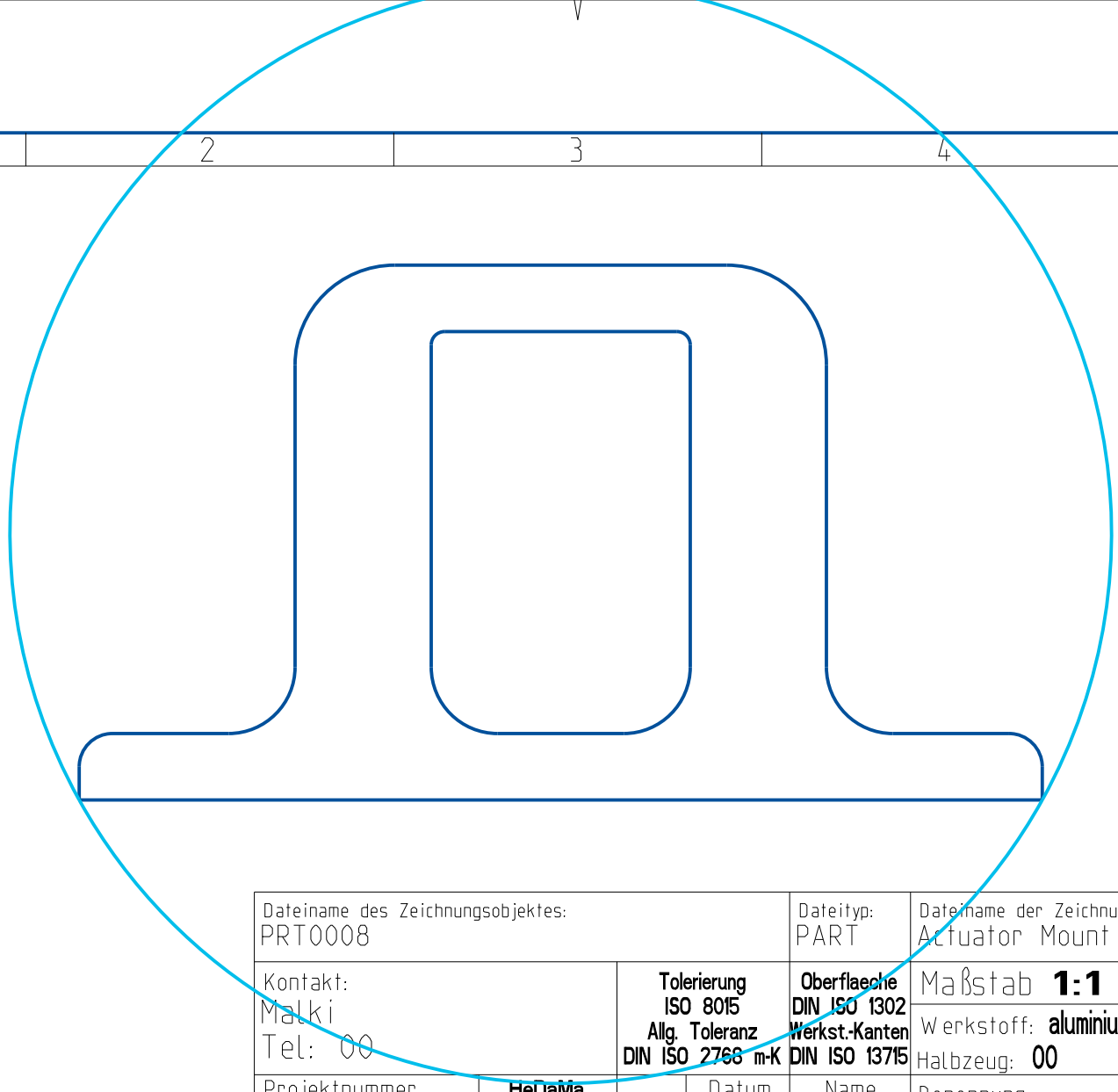


Dateiname des Zeichnungsobjektes: PRT0006			Dateityp: PART	Dateiname der Zeichnung: Housing Clamp Top	Format: A4
Kontakt: Malki Tel: 00		Tolerierung ISO 8015 Allg. Toleranz DIN ISO 2768 m-K	Oberflaeche DIN ISO 1302 Werkst.-Kanten DIN ISO 13715	Maßstab 1:1	Gew.: 150g kg
				Werkstoff: aluminium Halbzeug: 00	
Projektnummer	HeDaMa		Datum	Name	Benennung: Housing Clamp Top
Stückzahl	2	Bear.	Mar-11-26	Catarina Brites	
		Gepr.			
		Norm			
		IFKM		Zeichnungsnummer: 20260309_CB_02	Blatt 3 / 3 Bl.
Zust. Änderung	Datum Nam.	(Urspr.)		(Ers.f.:)	(Ers.d.:)

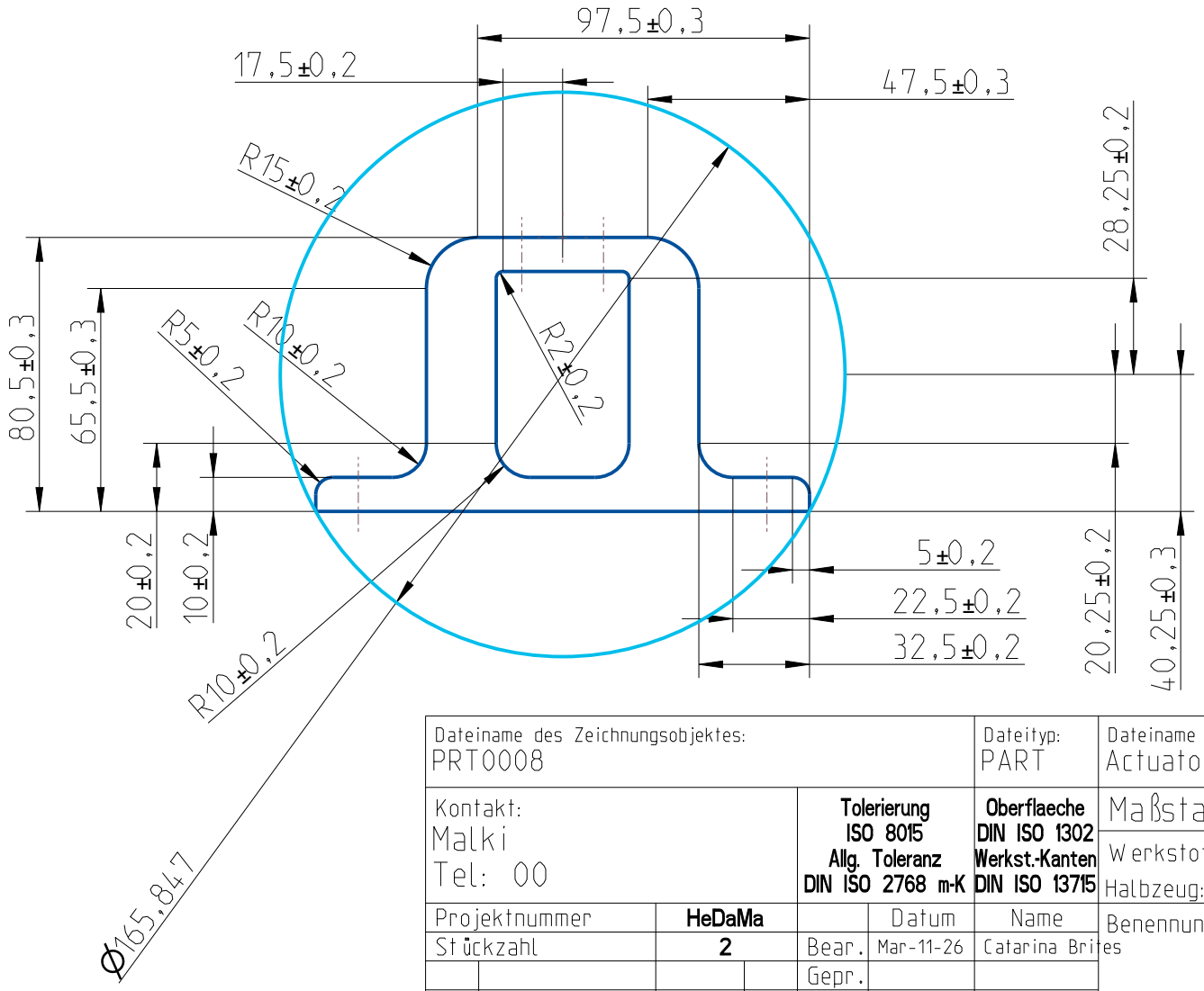


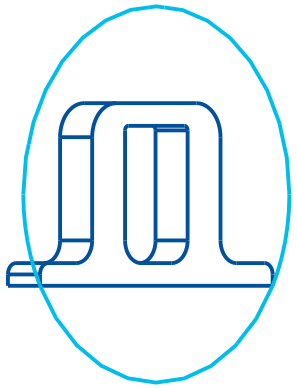


Dateiname des Zeichnungsobjektes: PRT0008			Dateityp: PART	Dateiname der Zeichnung: Actuator Mount	Format: A4
Kontakt: Malki Tel: 00		Tolerierung ISO 8015 Allg. Toleranz DIN ISO 2768 m-K	Oberflaeche DIN ISO 1302 Werkst.-Kanten DIN ISO 13715	Maßstab 1:1	Gew.: 200g kg
				Werkstoff: AlCuMgPb Halbzeug: 0	
Projektnummer	HeDaMa		Datum	Name	Benennung: Actuator Mount
Stückzahl	2	Bear.	Mar-09-26	Catarina Brites	
		Gepr.			
		Norm			
		IFKM		Zeichnungsnummer: 20260309_CB_01	Blatt 1 / 3 Bl.
Zust. Änderung	Datum Nam.	(Urspr.)		(Ers.f.:)	(Ers.d.:)



Dateiname des Zeichnungsobjektes: PRT0008			Dateityp: PART	Dateiname der Zeichnung: Actuator Mount	Format: A4
Kontakt: Malki Tel: 00		Tolerierung ISO 8015 Allg. Toleranz DIN ISO 2768 m-K	Oberflaeche DIN ISO 1302 Werkst.-Kanten DIN ISO 13715	Maßstab 1:1	Gew.: 200g kg
				Werkstoff: aluminium Halbzeug: 00	
Projektnummer	HeDaMa		Datum	Name	Benennung: Actuator Mount
Stückzahl	2	Bear.	Mar-09-26	Catarina Brites	
		Gepr.			
		Norm			
		IFKM		Zeichnungsnummer: 20260309_CB_01	Blatt 2 / 3 Bl.
Zust. Änderung	Datum Nam.	(Urspr.)		(Ers.f.:)	(Ers.d.:)

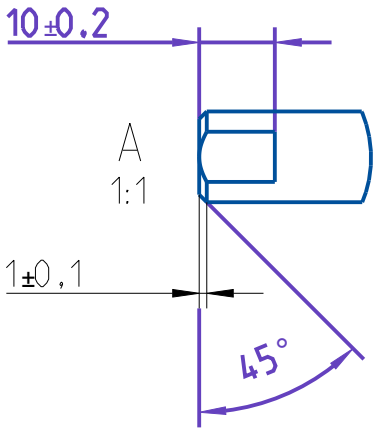


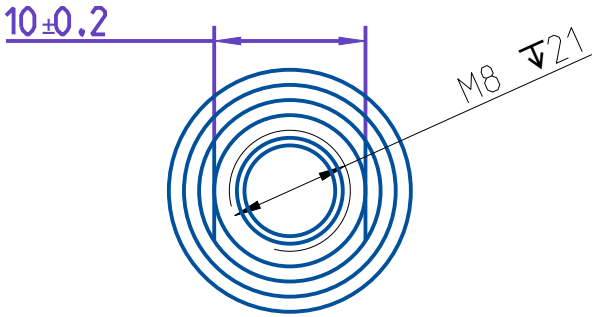


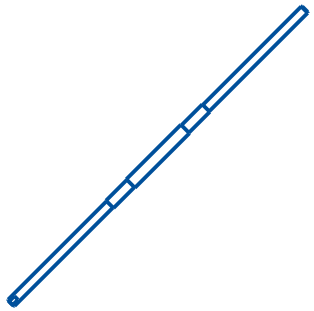
3:10

Dateiname des Zeichnungsobjektes: PRT0008			Dateityp: PART	Dateiname der Zeichnung: Actuator Mount	Format: A4
Kontakt: Malki Tel: 00		Tolerierung ISO 8015 Allg. Toleranz DIN ISO 2768 m-K	Oberflaeche DIN ISO 1302 Werkst.-Kanten DIN ISO 13715	Maßstab 4:5	Gew.: 200g kg
				Werkstoff: AlCuMgPb Halbzeug: 00	
Projektnummer	HeDaMa		Datum	Name	Benennung: Actuator Mount
Stückzahl	2	Bear.	Mar-11-26	Catarina Brites	
		Gepr.			
		Norm			
		IFKM		Zeichnungsnummer: 20260309_CB_01	Blatt 3 3 Bl.
Zust. Änderung	Datum Nam.	(Urspr.)		(Ers.f.:)	(Ers.d.:)

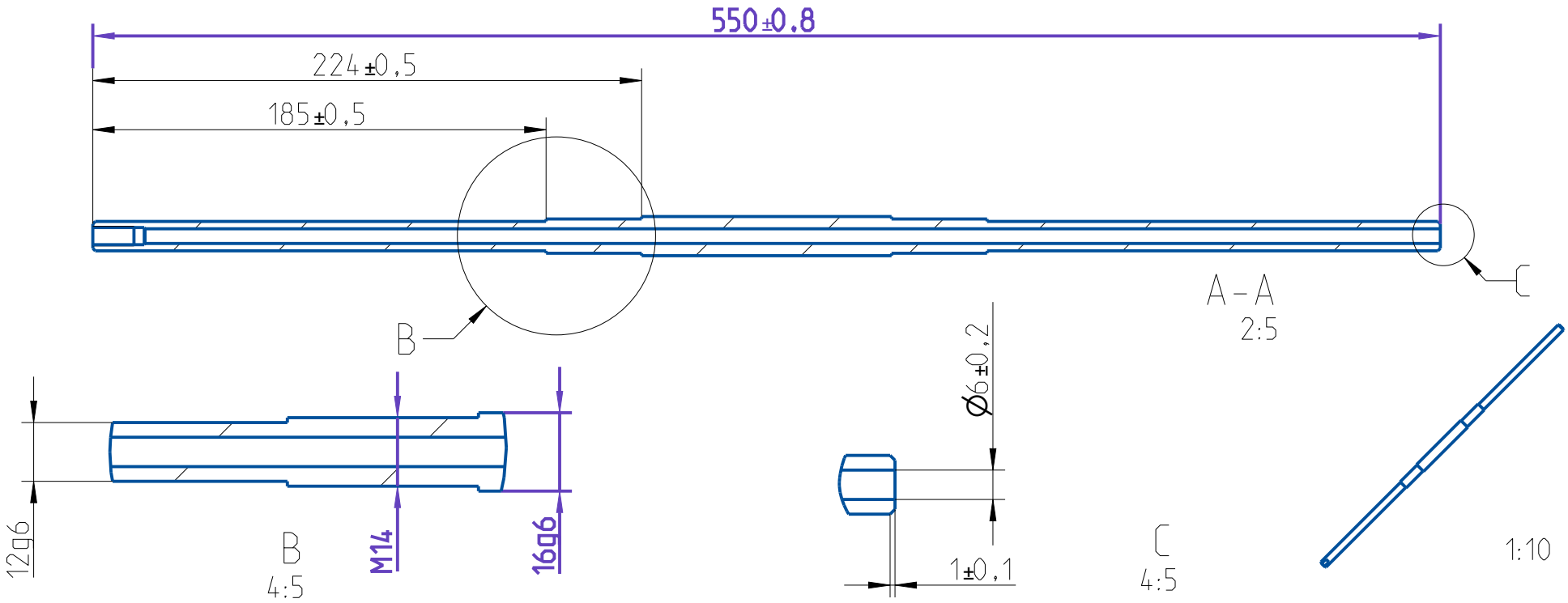


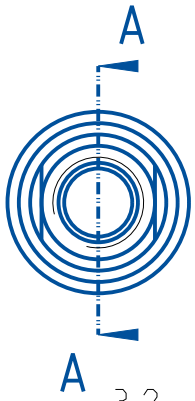




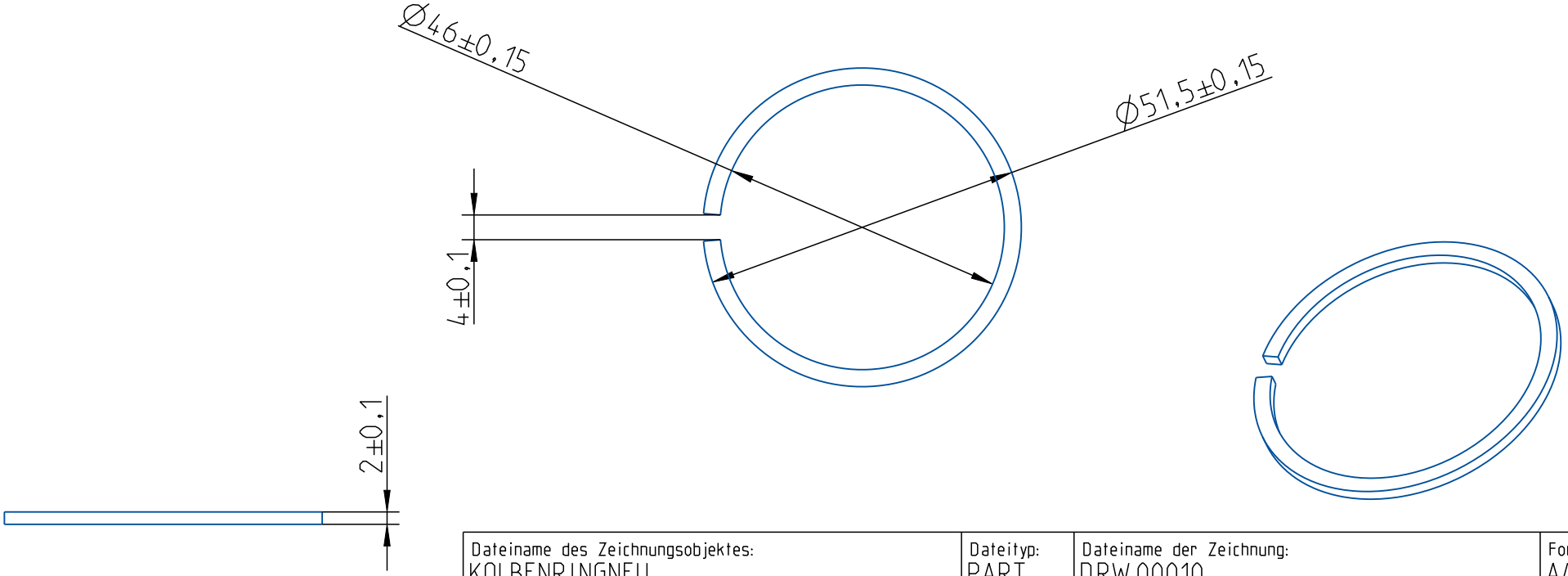


Dateiname des Zeichnungsobjektes: WELLE			Dateityp: PART	Dateiname der Zeichnung: DRW WEELE2	Format: A4
Kontakt: Malki Tel: 00		Tolerierung ISO 8015 Allg. Toleranz DIN ISO 2768 m-K	Oberflaeche DIN ISO 1302 Werkst.-Kanten DIN ISO 13715	Maßstab 1:1	Gew.: 100g kg
				Werkstoff: aluminium Halbzeug: 00	
Projektnummer	HeDaMa		Datum	Name	Benennung: Welle
Stückzahl	1	Bear.	Apr-23-26	Catarina Brites	
		Gepr.			
		Norm			
		IFKM		Zeichnungsnummer: 20260423_CB_01	Blatt 1 / 2 Bl.
Zust. Änderung	Datum Nam.	(Urspr.)		(Ers.f.:)	(Ers.d.:)

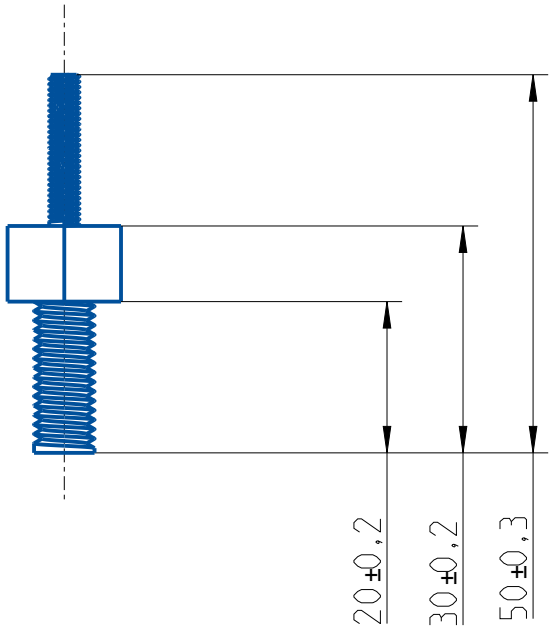


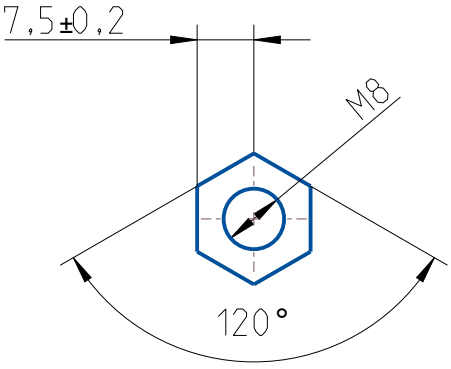


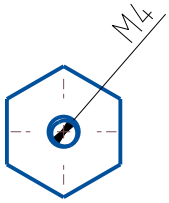
Dateiname des Zeichnungsobjektes: WELLE			Dateityp: PART	Dateiname der Zeichnung: DRW WEELE2	Format: A4
Kontakt: Malki Tel: 00		Tolerierung ISO 8015 Allg. Toleranz DIN ISO 2768 m-K	Oberflaeche DIN ISO 1302 Werkst.-Kanten DIN ISO 13715	Maßstab 1:1	Gew.: 100g kg
				Werkstoff: aluminium Halbzeug: 00	
Projektnummer	HeDaMa		Datum	Name	Benennung: Welle
Stückzahl	1	Bear.	Apr-23-26	Catarina Brites	
		Gepr.			
		Norm			
		IFKM		Zeichnungsnummer: 20260423_Cb_01	Blatt 2 / 2 Bl.
Zust. Änderung	Datum Nam.	(Urspr.)		(Ers.f.:)	(Ers.d.:)

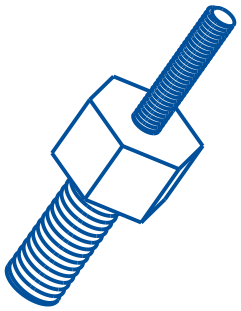


Dateiname des Zeichnungsobjektes: KOLBENRINGNEU			Dateityp: PART	Dateiname der Zeichnung: DRW 00010	Format: A4
Kontakt: Malki Tel: 00		Tolerierung ISO 8015 Allg. Toleranz DIN ISO 2768 m-K	Oberflaeche DIN ISO 1302 Werkst.-Kanten DIN ISO 13715	Maßstab **1:1**	Gew.: **10g** kg
				Werkstoff: **Teflon** Halbzeug: **00**	
Projektnummer	**HeDaMa**		Datum	Name	Benennung: **KolbenRing**
Stückzahl	**4**	Bear.	Jun-29-26	Catarina Brites	
		Gepr.			
		Norm			
		IFKM		Zeichnungsnummer: **20260519_CB_01**	Blatt 1 / 1 Bl.
Zust. Änderung	Datum Nam.	(Urspr.)		(Ers.f.:)	(Ers.d.:)

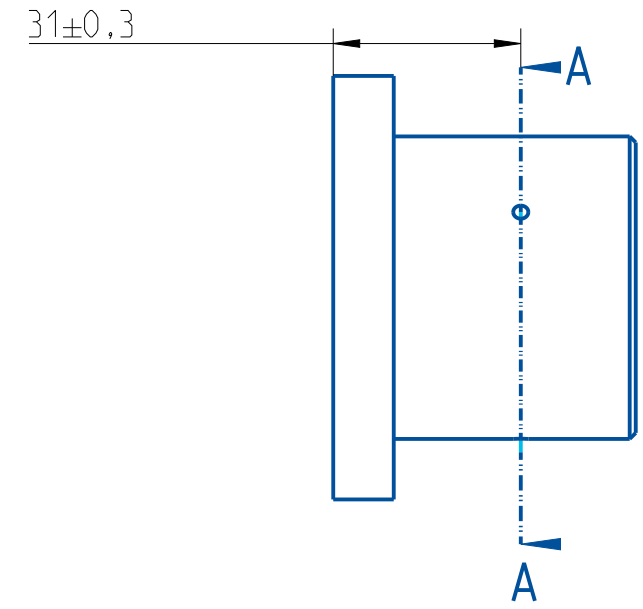


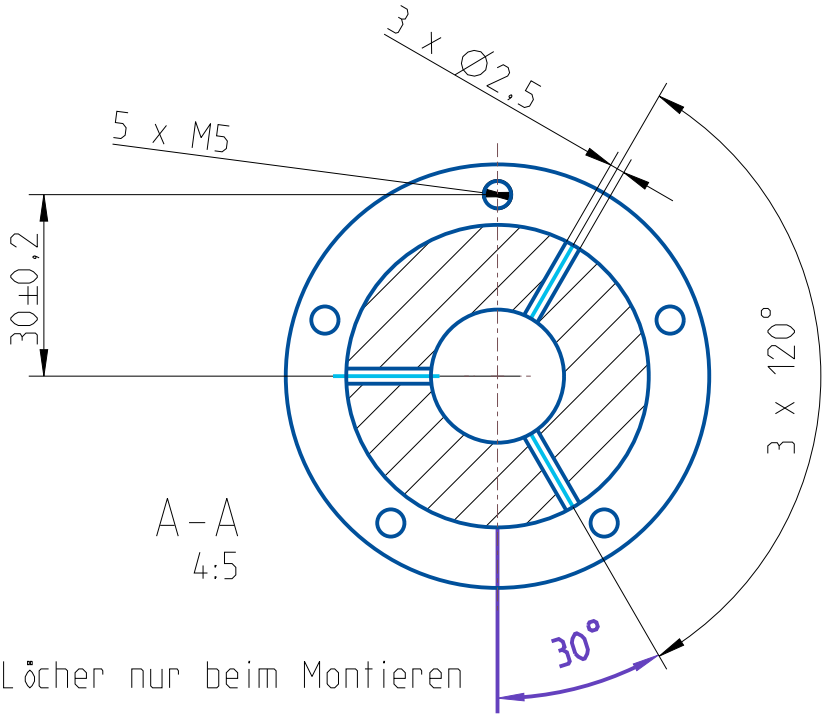






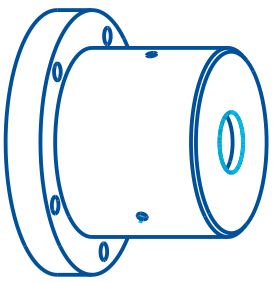
Dateiname des Zeichnungsobjektes: PRT0009			Dateityp: PART	Dateiname der Zeichnung: Shaft Coupling	Format: A4
Kontakt: Malki Tel: 00		Tolerierung ISO 8015 Allg. Toleranz DIN ISO 2768 m-K	Oberflaeche DIN ISO 1302 Werkst.-Kanten DIN ISO 13715	Maßstab 1:1	Gew.: 50g kg
				Werkstoff: stainless steel Halbzeug: 00	
Projektnummer	HeDaMa		Datum	Name	Benennung: Shaft Coupling
Stückzahl	1	Bear.	Mar-13-26	Catarina Brites	
		Gepr.			
		Norm			
IFKM				Zeichnungsnummer: 20260313_CB_06	Blatt 1 / 1 Bl.
Zust. Änderung	Datum	Nam. (Urspr.)		(Ers.f.:)	(Ers.d.:)





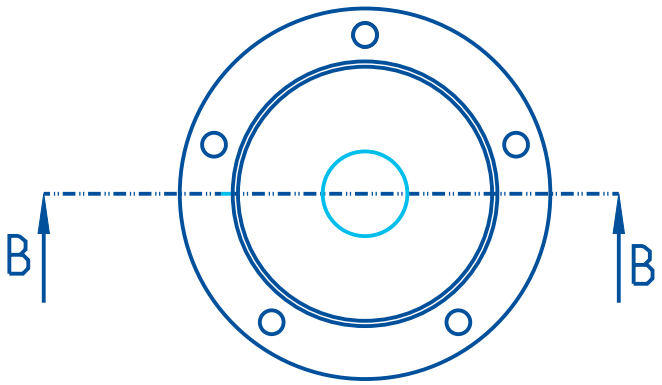
A-A
4:5

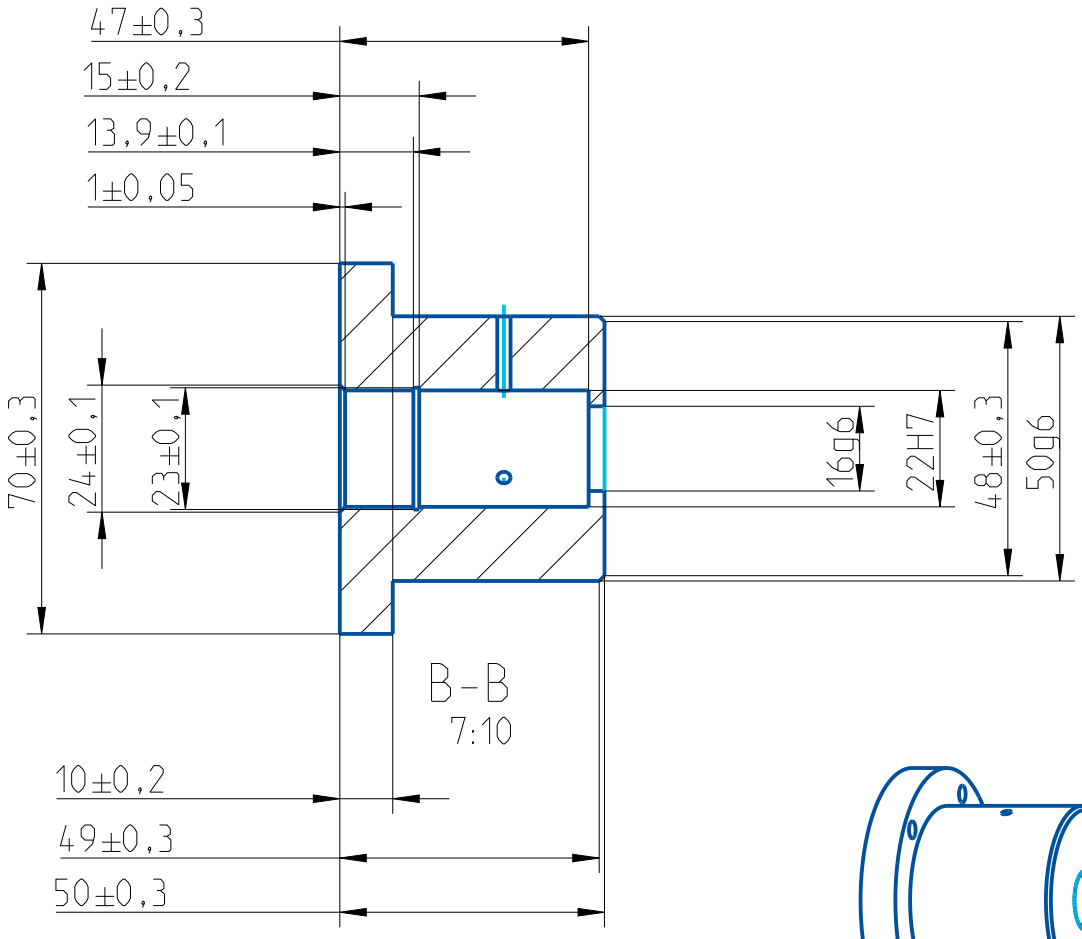
Löcher nur beim Montieren



1:2

Dateiname des Zeichnungsobjektes: PRT_07		Dateityp: PART	Dateiname der Zeichnung: DRW 0007	Format: A4
Kontakt: malki Tel: 00	Tolerierung ISO 8015 Allg. Toleranz DIN ISO 2768 m-K	Oberflaeche DIN ISO 1302 Werkst.-Kanten DIN ISO 13715	Maßstab 4:5	Gew.: 100g kg
			Werkstoff: aluminium	
			Halbzeug: 00	
Projektnummer: HeDaMa		Datum	Name	Benennung: Intern Stamge
Stückzahl: 2		Bear. Apr-27-26	Catarina Brites	
		Gepr.		
		Norm		
IFKM			Zeichnungsnummer: 20260427_CB_01	Blatt 1 / 2 Bl.
Zust. Änderung	Datum Nam.	(Urspr.)	(Ers.f.:)	(Ers.d.:)





1:2

Dateiname des Zeichnungsobjektes: PRT_07		Dateityp: PART	Dateiname der Zeichnung: DRW 0007	Format: A4
Kontakt: Malki Tel: 00	Tolerierung ISO 8015 Allg. Toleranz DIN ISO 2768 m-K	Oberflaeche DIN ISO 1302 Werkst.-Kanten DIN ISO 13715	Maßstab 7:10	Gew.: 100g kg
			Werkstoff: aluminium	
			Halbzeug: 00	
Projektnummer: HeDaMa		Datum	Name	Benennung: Intern Stange
Stückzahl: 2	Bear.	Apr-27-26	Catarina Brites	
	Gepr.			
	Norm			
IFKM			Zeichnungsnummer: 20260427_CB_01	Blatt 2 / 2 Bl.
Zust. Änderung Datum Nam.	(Urspr.)		(Ers.f.:)	(Ers.d.:)

B.2 Experimental Setup

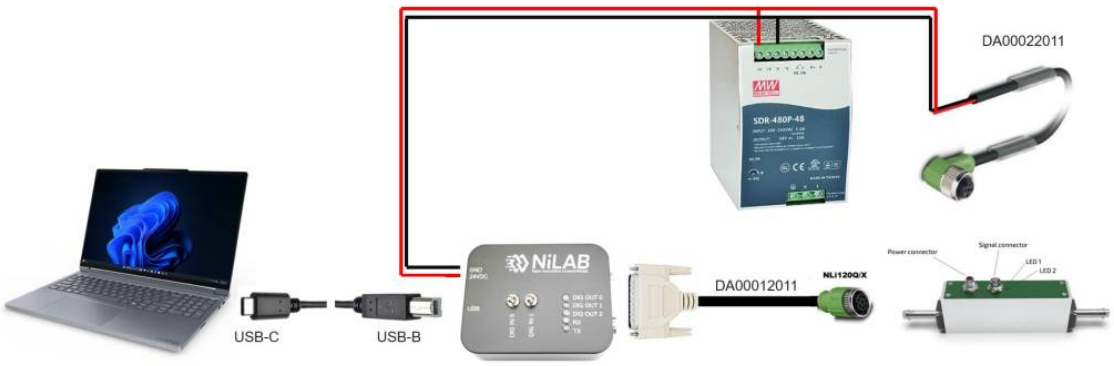


Figure B.1: Programming box combined with NLi120X motor (cable connections) .

B.3 Control Parameters

Table B.1: Feedback control parameters.

Position Feedback			**Speed Feedback**			**Current Feedback**			
K_p	K_i	**Max Speed**	K_p	K_i	**LP Filter**	K_p	K_i	$I_{\max}$ **[A]**	**LP Filter**
100	5	3 [m/s]	1200	14	1000 [Hz]	3000	80	15	200 [Hz]

Table B.2: Feed forward control parameters.

Feed Forward Gain	
Speed	**Acceleration**
11	100

B.4 NiLab Meeting

Table B.3: Description of Meeting with NiLAB.

Topic	Analysis of Performance Results
Date/Location	4 August 2026, via Microsoft Teams
Participants	**NiLAB:** Marco Gavesi **IFKM:** Malki Maliha, Catarina Brites
Content	This meeting was arranged after a series of experimental tests had been conducted using different combinations of frequencies, stroke amplitudes, and moving mass configurations. The meeting began with a software update performed by Marco Gavesi. which corrected a bug present in the previously used software, where the target current was being incorrectly saturated. The discussion then focused on the main factor limiting the actuator performance, which Marco Gavesi explained that it was centered in thermal overload (*I2T Overcurrent*), which is monitored through the RMS current. Due to these thermal constraints, the motor was unable to sustain the current levels required to reach the desired operating speeds. It was further explained that higher operating speeds are only achievable when very small stroke amplitudes are required, since the thermal load increases significantly with larger amplitudes. Several possible solutions to improve the thermal performance were discussed. These included the use of additional cooling methods, such as mounting the actuator on a heat sink plate or implementing forced-air cooling with a fan. However, it was clarified that replacing the power supply with a higher-current source (e.g., 48 A) would not solve the problem, as the limitation originates from the motor's thermal characteristics rather than the available electrical power. Finally, the limitations associated with the generation of the velocity profile were discussed. The precision of the velocity profile is constrained by the encoder resolution, which has a maximum update rate of 1 ms. In addition, the control system introduces an unavoidable waiting time of approximately 6 ms, making it impossible to generate a perfectly sinusoidal motion profile.

Appendix C

Attachments - Results and Discussion

C.1 Operation Limits

Table C.1 presents the maximum speeds supported by the actuator under the different operating conditions and configurations. This complements the information presented in Figure 4.1. Configurations without piston rings (B and D) are not specified, as they have the same speed limit as their counterparts with piston rings (C and E).

Table C.1: Operating limits identified for each configuration and stroke amplitude based on the last recorded point before I^2T thermal overload.

Configuration	Stroke	Operating limit speed (rpm)	Motor load (%)
A	20 mm	475	70
	25 mm	450	80
	30 mm	400	70
C	20 mm	450	75
	25 mm	400	85
	30 mm	400	90
E	20 mm	400	55
	25 mm	400	90
	30 mm	375	90